Scuola Internazionale Superiore di Studi Avanzati - Trieste

Condensed Matter

Unconventional Phases in Doped or Frustrated Quantum Antiferromagnets: a Systematic QMC Study

Thesis submitted for the degree of
Doctor Philosophiae

CANDIDATE

Wenjun Hu

SUPERVISORS

Prof. Sandro Sorella

Dr. Federico Becca

September 2013

SISSA - Via Bonomea 265 - 34136 TRIESTE - ITALY

Abstract

We investigate the ground-state properties of two strongly-correlated systems: the two-dimensional $t-J$ model that can be used to study the high-temperature superconducting phase in the doped antiferromagnet, and the frustrated Néel antiferromagnet described by the $J_1 - J_2$ Heisenberg model on the square lattice, which is widely considered as the prototype model for spin frustration.

In this thesis, we apply to these two systems state-of-the-art quantum Monte Carlo techniques, including the variational and the Green's function Monte Carlo with the fixed-node approximation. Few Lanczos steps are used to systematically improve the accuracy of the trial wave functions. By introducing a suitable regularization scheme for the variational calculations with few Lanczos steps, stable and controllable simulations can be performed up to very large cluster sizes with very good accuracy.

In the two-dimensional $t-J$ model at $J/t = 0.4$, we show that the accuracy of the Gutzwiller-projected variational state (containing $d_{x^2-y^2}$ pairing) can be improved much by few Lanczos steps; in addition, the fixed-node Monte Carlo with these systematically improvable trial wave functions gives results that are comparable with the best accurate DMRG ones. Our main outcome is that the ground state is homogeneous and no evidence of stripes is detected around the doping $\delta = 1/8$. Indeed, our best approximation to the ground state does not show any tendency towards charge inhomogeneity. Furthermore, our results show that a uniform state containing superconductivity and antiferromagnetism is stabilized at low hole doping, i.e., $\delta \lesssim 0.1$.

In the $J_1 - J_2$ Heisenberg model on the square lattice, we use the projected mean-field state that is built from Abrikosov fermions having a Z_2 gauge structure

and four Dirac points in the spinon spectrum. No spin or dimer order is found in the strongly frustrated regime and our calculations imply that a spin liquid phase may faithfully represent the exact ground state around $J_2/J_1 = 0.5$. The few Lanczos step technique is used to systematically improve the accuracy of the variational states both for the ground state and for few relevant low-energy excitations. This procedure allows us to estimate, in a valuable and systemic way, the spin gaps within thermodynamical limit and to show a solid evidence of an unconventional gapless excitation spectrum in the strongly frustrated regime, i.e., $J_2/J_1 \simeq 0.5$. In particular, we found gapless triplet excitations at momenta $(\pi, 0)$ and $(0, \pi)$, which are compatible with the presence of four Dirac points at momenta $(\pm\frac{\pi}{2}, \pm\frac{\pi}{2})$ in the spinon spectrum.

Contents

Abstract **i**

Contents **1**

Introduction **11**

1 Strongly correlated electron systems **17**

1.1 Microscopic models for correlated electrons 20

1.2 The quantum antiferromagnet 22

1.3 Doping the Mott insulator 25

1.4 Adding frustrating super-exchange couplings to the Néel antiferromagnet 28

1.4.1 Fermionic mean-field approach to spin models and the projective symmetry group 30

2 Numerical Methods **39**

2.1 Lanczos 40

2.2 Variational Monte Carlo 41

2.3 The Minimization Algorithm 44

2.4 Few Lanczos Steps 46

2.4.1 Variance Extrapolation 48

2.4.2 Regularization 49

2.5 Green's Function Monte Carlo 53

3 Stripe in the 2D $t-J$ model **59**
3.1 Introduction 59
3.2 Model and methods 61
3.3 Results 64
3.4 Conclusions 73

4 Quantum Spin Liquid **77**
4.1 Introduction 77
4.2 Model and Methods 80
4.3 Calculations with fixed parameters 83
4.4 Main Results 85
4.5 Conclusions 98

Conclusions **99**

Bibliography **103**

Acknowledgment **109**

List of Publications **111**

List of Figures

1 An example of stripe phase in a two-dimensional lattice. The size of the circles and arrows is proportional to the electron density and spin along z direction, respectively. Anti-parallel spins across the hole-rich sites (empty circles), i.e., the π shift. 12

1.1 Three spins on a triangle with antiferromagnetic interactions. 19

1.2 Néel order on the square lattice. The dashed lines indicate the second-order virtual hopping. 22

1.3 (a) and (b) represent two particular valence bond states. The red lines represent the singlet bonds between two spins. 23

1.4 Two holes in an antiferromagnet. In the $J \gg t$ limit, the energy loss with respect to the ordered state is given by number of broken bonds (red lines). (a) two holes are widely separated and break 8 bonds, (b) two holes form a pair and break 7 bonds. 24

1.5 Energy per hole $e(\delta)$ as function of doping δ for a stable (a) and unstable (b) system. The dashed line is the Maxwell construction. . . 26

1.6 Nearest- (J_1) and next-nearest-neighbor (J_2) spin-spin super-exchanges in the two-dimensional square lattice. The second-neighbor interaction frustrates the Néel order. 28

1.7 The schematic phase diagram of the $J_1 - J_2$ Heisenberg model on the square lattice at zero temperature. Magnetic phases settle down for small J_2/J_1 and large J_2/J_1 values. In between a quantum spin liquid is expected to be stabilized. 29

2.1 The local energy as function of the Monte Carlo steps without regularization. The $S = 1$ excitation at $J_2/J_1 = 0.5$ in the $J_1 - J_2$ Heisenberg model on the 6×6 lattice with $p = 1$. 49

2.2 Test curves showing the importance of the regularization used for the $S = 1$ excitation with $p = 1$ at $J_2/J_1 = 0.5$ in the $J_1 - J_2$ Heisenberg model on the 6×6 lattice. ε is the value of the regularization used (see text). The insets are the amplification of the region $10^{-8} \leq \varepsilon \leq 10^{0}$. . 50

2.3 Test curves obtained by adding noise to the determinant for the $S = 2$ excitation with $p = 0, 1, 2$ at $J_2/J_1 = 0.2, 0.3$ in the $J_1 - J_2$ Heisenberg model on the 6×6 lattice. The extrapolated energy values are compared with the exact results. 52

3.1 Variational results for the variance extrapolation on a 162-site cluster, for different numbers of holes: $p = 0$ and 1 ($p = 0, 1$ and 2) Lanczos steps have been performed on the wave function with (without) antiferromagnetism. The best fixed-node results are also marked by arrows. 63

3.2 Energy per hole as a function of the doping for $J/t = 0.4$. Variational results are reported for $p = 0$ and 1 ($p = 0, 1$ and 2) Lanczos steps for the wave function with (without) antiferromagnetism. The extrapolated gap for $0.03 \lesssim \delta \lesssim 0.15$ are reported. 65

3.3 Energy per hole as a function of the doping for $J/t = 0.4$. Fixed-node results are reported for $p = 0$ and 1 ($p = 0, 1$ and 2) Lanczos steps for the wave function with (without) antiferromagnetism. The best variational DMRG and iPEPS energies [16] and the fixed-node with $p = 2$ are connected by dashed lines for a better comparison. 66

3.4 The CDW parameters as function of SR steps at 1/8 doping on 24×24 size cluster. (a) $l_s = 8$; (b) $l_s = 12$. i labels different sites. 68

3.5 Upper panels: local density n_i when a site-dependent chemical potential with $\delta\mu = 1.6$ [see Eq. (3.8)] is added to the variational wave function; the cases with $l_s = 12$ (a) and 8 (b) are reported. Lower panels: local density n_i when a site-dependent potential [see Eq. (3.9)] is added to the $t-J$ Hamiltonian, with $l_s = 12$ and $V = 0.2$ (c) and $l_s = 8$ and $V = 0.4$ (d). Variational and fixed-node results are reported for a 12×12 cluster and $\delta = 1/8$. Insets: the difference between the largest and the smallest local density (at the fixed-node level) as a function of V. 70

3.6 The density-density correlation function calculated by using the same parameters as Fig. 3.5. Upper panels: a site-dependent chemical potential with $\delta\mu = 1.6$ [see Eq. (3.8)] is added to the variational wave function; the cases with $l_s = 12$ (a) and 8 (b) are reported. Lower panels: a site-dependent potential [see Eq. (3.9)] is added to the $t-J$ Hamiltonian, with $l_s = 12$ and $V = 0.2$ (c) and $l_s = 8$ and $V = 0.4$ (d). Variational and fixed-node results are reported for a 12×12 cluster and $\delta = 1/8$. 71

3.7 The SDW parameters as function of SR steps in the $2 \times l_s$ unit cell at 1/8 doping on 24×24 size cluster. (a) $l_s = 8$; (b) $l_s = 12$. i labels different sites. 73

3.8 Variational (a) and fixed-node (b) charge and spin distributions in the 2×8 unit cell of a 16×16 lattice. The size of the circles and arrows is proportional to the electron density and spin along z, respectively (largest symbols: $n_{R_i} = 0.9195(4)$, $S^z_{R_i} = \pm 0.087(2)$). 74

4.1 The ground state energy per site of eight Z_2 spin liquids in Ref. [50] (Z2A0013, Z2A001n,Z2Azz13, Z2Azz1n, Z2B0013, Z2B001n, Z2Bzz13, Z2Bzz1n) at $J_2/J_1 = 0.5$ on different sizes ($L = 6, 10, 18$). Black crossings mark unstable spin liquids, for which the variational parameters related to Z_2 symmetry vanish after the optimization of the wave function. The best energy is given by the ansatz Z2Azz13. . . . 78

4.2 The mean field spectrum of the Hamiltonian Eq.(4.1). Four red points are the Dirac points. 79

4.3 Calculations with fixed parameters of $S = 2$ spin gap Δ_2 by using different wave functions (Z_2 and $U(1)$ spin liquids) for $J_2/J_1 = 0$ and $J_2/J_1 = 0.55$ on square lattice until 50×50 cluster. The solid line is the linear fitting. 82

4.4 Calculations with fixed parameters of spin-spin correlation function $S(q)$ by using Z_2 spin liquid wave function at $J_2/J_1 = 0.55$ on 30×30 and 50×50 clusters. 82

4.5 The d_{xy} pairing as function of J_2/J_1 on 6×6 lattice for the ground state. The value of d_{xy} is nonzero for $J_2/J_1 > 0.4$. 84

4.6 The spin-spin correlation function at momentum (π, π) divided by N_{site} at $J_2/J_1 = 0.5$ on different sizes ($L = 14, 22, 30$) are reported. The quadratic fit is performed to show the non-magnetic order in the thermodynamical limit. 84

4.7 The dimer order parameter D_d as function of $1/L$ at $J_2/J_1 = 0.45$, 0.5 and 0.55 are reported. No dimer order is shown by the quadratic fit. 85

4.8 Energies per site for the $S = 0$ ground state (a), the $S = 1$ state with $k = (\pi, 0)$ (b), and the $S = 2$ with $k = (0, 0)$ (c) versus the variance for $J_2/J_1 = 0.5$. The results with $p = 0$, 1, and 2 are reported for $L = 4$, 6, 8, and 10, and with only $p = 0$ and $p = 1$ for $L = 14$ and $L = 18$. The variance extrapolated results are also shown. 87

4.9 Spin gap for the $S = 1$ excitation at $k = (\pi, 0)$ for the 6×6 cluster. Results for $p = 0$, 1, and 2 Lanczos steps are reported, together with the extrapolated and the exact energies. 88

4.10 Spin gap for the $S = 2$ excitation with $k = (0, 0)$ for the 6×6 cluster. Results for $p = 0$, 1, and 2 Lanczos steps are reported, together with the extrapolated and the exact ones. 88

4.11 The $S = 2$ spin gap as a function of the system size for the variational wave function and the Lanczos extrapolation for $J_2/J_1 = 0.5$. The thermodynamic extrapolation is consistent with a vanishing gap within the errorbar, i.e., $\Delta_2 = -0.04(5)$. The DMRG results on $2L \times L$ cylinders (with open boundary conditions along x and periodic along y) for the $S = 1$ excitation are also shown [17]. Exact results (stars) of the $S = 2$ gap and the lowest $S = 1$ gap on the 6×6 cluster (with periodic boundary conditions) are reported. 89

4.12 The $S = 2$ spin gap as a function of the system size for the variational wave function and the Lanczos extrapolation for $J_2/J_1 = 0.55$. The thermodynamic extrapolation is consistent with a vanishing gap within the errorbar, i.e., $\Delta_2 = -0.07(7)$. The DMRG results on $2L \times L$ cylinders (with open boundary conditions along x and periodic along y) for the $S = 1$ excitation are also shown [17]. Exact results (stars) of the $S = 2$ gap and the lowest $S = 1$ gap on the 6×6 cluster (with periodic boundary conditions) are reported. 90

4.13 The $S = 1$ spin gap with $k = (\pi, 0)$ as a function of the system size for the variational wave function and the Lanczos extrapolation at $J_2/J_1 = 0.45$. The Lanczos step procedure reduces the gap on each size. The thermodynamic extrapolation shows a finite gap within the errorbar, i.e., $\Delta_1 = 0.10(4)$. 91

4.14 The $S = 1$ spin gap with $k = (\pi, 0)$ as a function of the system size for the variational wave function and the Lanczos extrapolation at $J_2/J_1 = 0.5$. The Lanczos step procedure reduces the gap on each size. The thermodynamic extrapolation is consistent with a vanishing gap within the errorbar, i.e., $\Delta_1 = -0.00(3)$. 92

4.15 The behavior of the extrapolated gap as a function of J_2/J_1 is reported. The line is a guide to the eye. The Lanczos extrapolated gap as a function of L for different values of J_2/J_1 are also reported in the inset. 94

5.1 A continuous phase transition between antiferromagnetic order (AF) and the gapless Z_2 spin liquid. At the critical point, the vison gap (green line) and the $S = 1$ spin gap with $k = (\pi, 0)$ (red line) vanish. A state with four gapless modes with momenta $(0, 0)$, (π, π), $(\pi, 0)$, and $(0, \pi)$ is obtained not only in the spin-liquid regime but also at the critical point. 100

List of Tables

3.1 VMC and FN energies per site for 26 sites with 2 and 4 holes. The estimated values of the variance extrapolation and exact results are also reported. 67

4.1 p=0 96
4.2 p=1 96
4.3 p=2 97
4.4 extrapolation 97

Introduction

The study of strongly-correlated electron systems is one of the most exciting and challenging areas in condensed-matter physics. Recently, several very interesting new phases of matter have been theoretically proposed and experimentally observed in several materials. Among them, the discovery of the cuprate high-temperature superconductors by Bednorz and Müller in 1986 [1] has opened a new era of unconventional superconductors. These materials are made by Copper-Oxygen planes intercalated by (insulating) block layers generically containing rare earths and Oxygens. The 'parent' compounds of the cuprate superconductors are Mott insulators with antiferromagnetic Néel ordering [2]. The phase diagram becomes very rich when the electron density is changed in the Copper-Oxygen planes by substituting the rare earths with lower valence elements or by adding Oxygen in the insulating block layers. Besides the superconducting phase, an interesting charge-density (often called stripe) order has been observed in Copper-oxide materials by neutron scattering studies [3, 4, 5]. Here, the doped charges are concentrated along domain walls between antiferromagnetic insulating regions [6]: see Fig.1 for an example of a stripe. The origin of these microscopic inhomogeneities may be due to the competition between the strong antiferromagnetic interaction and the long-range Coulomb interaction between charges. The understanding of the origin and the mechanism, which should be different from the standard electron-phonon interaction, of high-temperature superconductors is one of the biggest challenges in the present theory of condensed matter.

Another class of interesting compounds is given by pure Mott insulators, where no magnetic order is detected down to very low temperatures (i.e., several order of magnitude smaller than the super-exchange coupling). These materials are often

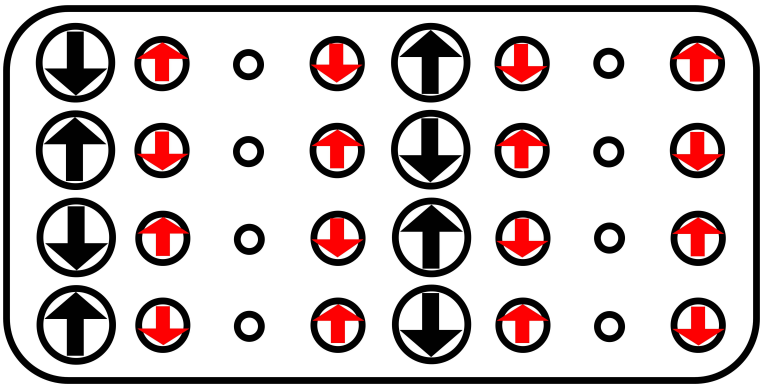

Figure 1: An example of stripe phase in a two-dimensional lattice. The size of the circles and arrows is proportional to the electron density and spin along z direction, respectively. Anti-parallel spins across the hole-rich sites (empty circles), i.e., the π shift.

characterized by the presence of competing magnetic interactions, which gives rise to frustration. Systems that do not show any kind of long-range order are called *spin liquids*. In recent years, there has been a huge experimental and theoretical effort to understand their physical properties. The possibilities to sustain elementary excitations with fractional quantum numbers (like in the fractional quantum Hall effect) and the existence of the so-called topological order are two prominent examples of the exotic properties characterizing spin liquids.

Among possible spin-liquid materials, it is worth to mention the organic charge-transfer salt $\kappa-(BEDT-TTF)_2Cu_2(CN)_3$, which has a triangular lattice structure [7, 8], and the so-called Herbertsmithite, $ZnCu_3(OH)_6Cl_2$, with a Kagomé lattice structure [9]. The exotic excitations of these materials can be studied by measuring physical quantities like for example magnetic susceptibility, specific heat, Neutron scattering, nuclear-magnetic resonance, and muon-spin resonance. In the organic salt $\kappa-(BEDT-TTF)_2Cu_2(CN)_3$, the magnetic susceptibility goes to a constant at low temperatures and the specific heat is linear in temperature, indicating gapless spin excitations; moreover, the ratio of magnetic susceptibility to the linear-temperature coefficient of the specific heat is close to the free-fermion one, suggesting that the excitations are fermionic spinons [8, 10]. Also in the Kagomé

material $ZnCu_3(OH)_6Cl_2$, the magnetic excitations are found to be (almost) gapless by magnetic susceptibility measurements [9, 10].

The electronic and chemical structure of these strongly-correlated materials is very intricate. In order to capture the relevant physics, it is necessary to simplify the problem as much as possible. In this regard, many effective low-energy models have been introduced to describe these strongly-correlated systems and they have attracted much attention also very recently. For instance, the Hubbard and $t-J$ models have been used to study the high-temperature superconducting phase in doped antiferromagnets, while one of the simplest frustrated Hamiltonian, namely the J_1-J_2 Heisenberg model on the square lattice, is still widely considered as the prototype model for spin frustration.

However, only one-dimensional models can be solved by analytic methods. For example, Bethe solved the Heisenberg model [11] and, later, Lieb and Wu solved the Hubbard model [12]. Instead, in two dimensions, there are no exact solutions. Traditional mean-field techniques and dynamical mean-field theory [13] also fail to give a satisfactory description of the phase diagram of the two-dimensional strongly-correlated electron systems. Therefore, many kinds of advanced numerical approaches have been used to study correlated electrons in two dimensions. As an example, the Lanczos method allows us to compute the exact properties of any Hamiltonian. Unfortunately, due to the exponential increase of the Hilbert space with the lattice size, this method is restricted to extremely small sizes.

An important step forward has been done by the density matrix renormalization group (DMRG) [14], which has been very successful for solving several one-dimensional models and recently has been aslo applied to two-dimensional systems. For the two-dimensional $t-J$ model, a stripe phase for $J/t=0.4$ at doping $\delta=\frac{1}{8}$ was found [15, 16]; more recently, a gapped spin liquid has been suggested in the strongly-frustrated regime of the J_1-J_2 Heisenberg model [17]. The main drawback of DMRG is that cylindrical boundary conditions are usually considered on highly anisotropic "ladder" geometries, composed by a relatively small number of "legs". As a result, an unbiased thermodynamic limit is difficult to reach, in comparison to systems retaining a full rotational/translational symmetry. Therefore, we believe that it is extremely important to compare DMRG results with other methods, in which a square lattice with periodic boundary conditions can be used.

The variational Monte Carlo method is one of the choices. Although several trial wave functions may be considered and compared, the main limitation of this technique is that the results crucially depend on the chosen wave function. In order to improve the variational Monte Carlo, it is possible to apply the Green's function Monte Carlo method [18]. By means of this method, starting from the variational wave function, the exact ground state can be filtered out. As other quantum Monte Carlo methods for fermionic systems, the well-known sign problem affects this technique. Due to the antisymmetry of the many-body wave function of ferminons, the cancellation between positive and negative weights during the simulation implies an exceedingly large statistical error for the Green's function Monte Carlo. In order to overcome this difficulty, some approximate method has been introduced, for example the fixed-node approximation [19].

In Ref. [20], Spanu and coworkers used the fixed-node Monte Carlo to study the $t-J$ model for $J/t \simeq 0.4$ and obtained a coexistence of superconductivity and antiferromagnetism in the small doping region. These results are in sharp contrast with the DMRG conclusions and, therefore, more accurate methods are required to clarify this issue. Based on a given trial wave function, a number p of Lanczos steps can be applied to approach the ground state by systematically improving the standard quantum Monte Carlo techniques. Within this approach, both the energy and variance can be computed. Since the ground state has the minimum energy and a zero variance, it is possible to estimate the exact ground-state energy by extrapolation to the zero variance limit. In this thesis we show that, if the variational wave function is a good approximation of the exact ground state, few Lanczos steps are enough to obtain a good estimate of the ground-state energy and its low-energy excitation spectrum.

We present the results for the two-dimensional $t-J$ model, showing that the accuracy of the Gutzwiller-projected variational state (containing $d_{x^2-y^2}$ pairing) can be improved much by few Lanczos steps; in addition, the fixed-node Monte Carlo with these systematically improvable trial wave functions gives results that are comparable with the best accurate DMRG ones. Our results do not show any evidence of static stripes at $J/t = 0.4$ in the $t-J$ model.

By using the same techniques, we also studied the $J_1 - J_2$ Heisenberg model on the square lattice: here, the projected wave function is written in terms of Abrikosov

fermions and has non-trivial pairing terms. A spin-liquid phase around $J_2/J_1 = 0.5$ is found, which is in agreement with the conclusion by DMRG. However, through accurate calculations up to large clusters for both the ground state and the low-energy excitations, we show a solid evidence of an unconventional gapless excitation spectrum in the strongly frustrated regime, i.e., $J_2/J_1 \simeq 0.5$. This outcome disagrees with the claim of a spin liquid with a finite spin gap $\sim 0.2J_1$, proposed by Jiang *et al.* with state-of-the-art DMRG calculations [17].

Chapter 1

Strongly correlated electron systems

The properties of non-interacting electrons in a periodic potential generated by the ions are well understood by the pioneering work of Bloch, just few years after the birth of quantum mechanics [21]. Bloch's theorem states that the eigenfunctions for such a system can be written as the product of a plane wave envelope function and a periodic function $u_{n,\mathbf{k}}(\mathbf{r})$ that has the same periodicity as the potential; the corresponding energy eigenvalues are $\epsilon_n(\mathbf{k}) = \epsilon_n(\mathbf{k} + \mathbf{K})$, which are periodic with periodicity $\mathbf{K}$ of a reciprocal lattice vector. The energies associated with the index n vary continuously with wave vector $\mathbf{k}$ and form an energy band identified by the index n. When a weak electron-electron interaction is added as a perturbation, the only effect is to slightly change the band structure and, therefore, the independent-electron picture is still valid and able to describe all physical properties. Later, Landau developed a framework to describe the interacting gas of electrons, in which the excitations close to the Fermi surface can be described as weakly-interacting *quasiparticles* [22]. The Fermi liquid is qualitatively analogous to the non-interacting Fermi gas, in the following sense: the system's dynamics and thermodynamics at low temperatures may be described by substituting the interacting fermions with non-interacting quasiparticles, which carry the same spin, charge and momentum as the original particles. The Bloch's theorem and the Landau theory of Fermi liquids are two pillars of the solid state physics and give the framework to understand most

of the known materials.

Within the independent-electron picture, it is possible to distinguish a metal from an insulator in a straightforward way, i.e., by looking at the filling of the electronic bands. An electronic system can be insulating only because there is a finite gap between the highest occupied level and the lowest unoccupied one: this is the so-called *band insulator*. In this sense, due to the spin degeneracy (in absence of the spin-orbit coupling) an odd number of electrons per unit cell naturally implies a partially filled conduction band and, therefore, a metallic behavior. However, when the repulsive interaction between electrons is sufficiently strong in comparison with their kinetic energy, the independent-electron picture may fail and the system can turn insulating, even with an odd number of electrons per unit cell. In 1937 Mott and Peierls introduced the so-called *Mott insulator*, whose origin comes from a strong electron-electron repulsion and, therefore, is completely different from a band insulator [23]. The cartoon picture of a Mott insulator is given by a regular lattice of Hydrogen atoms, whose distances may be varied: when the ions are close to each other, the electrons delocalize around the lattice, thus forming a half-filled band with a metallic character; on the contrary, when the ions are sufficiently far apart, it is more favorable to localize each electron around an ion, in order not to pay a considerable Coulomb repulsion. A metal to (Mott) insulator transition is expected to appear for a given distance between ions.

Strictly speaking, a Mott insulator is a state that does not break any of the symmetries of the original problem (e.g., translations, rotations, spin SU(2), time reversal, etc.) and cannot be adiabatically turned into a band insulator. In a looser definition, systems with magnetic order can be also included, whenever the magnetic order can be considered as a by-product, rather than the driving force to have an insulating behavior. After many years of intense investigations, the physics of quantum magnets still attracts a lot of interest. In particular, new problems arose from the discovery of high-temperature superconductors, whose parent compounds are Mott insulators with antiferromagnetic order (like for example La_2CuO_4) [2]. Besides the understanding of the origin of superconductivity from doping Mott insulators, one important issue is related to the possibility of destroying magnetic order by engineering competing super-exchange couplings. Whenever no magnetic order (and possibly other kinds of symmetry breaking) is developed down to zero

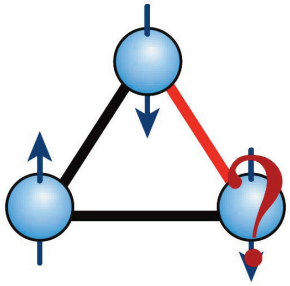

Figure 1.1: Three spins on a triangle with antiferromagnetic interactions.

temperature, we talk about spin *liquids* [10, 24].

One of the main path to obtain magnetically disordered ground states is to consider frustration in low-dimensional lattices. Frustration stands for the existence of competing interactions: individually, each term would give rise to a well defined minimal-energy configuration that however is not compatible with the other ones. The paradigmatic example is given by three spins on a triangle with antiferromagnetic interactions (see Fig. 1.1). The low spatial dimensionality is important to enhance quantum fluctuations. In this regard, the most interesting (and physically relevant) systems are two dimensional, since in one dimension, the Mermin-Wagner theorem forbids any kind of magnetic order (except for ferromagnetism) at zero temperature [25]. In the last few years, a huge effort has been spent to understand the low-temperature properties of various frustrated materials, like for example the Heisenberg model on triangular and Kagomé lattices in two dimensions, or even more complicated geometries in three dimensions.

Unfortunately, all traditional methods, such as mean-field theory or perturbation theory, fail to give a satisfactory description of the physical properties of strongly-correlated systems. Therefore, many kinds of numerical techniques have been introduced to study strongly correlated-electron problems. Density-matrix renormalization group (DMRG) or dynamical mean-field theory (DMFT) are two prominent examples that have been devised to study and understand particular aspects of correlated systems. However, both DMRG and DMFT fail to describe pure two-dimensional systems: while DMRG works preferably in one dimension, DMFT is

essentially an infinite-dimensional approximation. In addition, a considerable improvement has been done in quantum Monte Carlo methods, including variational and projection techniques, which have been widely used to clarify different issues. The great advantage of these stochastic methods is that two- or three-dimensional systems can be directly considered, thus having a direct comparison with real materials.

1.1 Microscopic models for correlated electrons

The prototypical Hamiltonian that contains the basic ingredients of strongly-correlated electrons on the lattice is the one-band Hubbard model [26]:

$$H_{Hub} = -t \sum_{\langle ij \rangle \sigma} c^{\dagger}_{i\sigma} c_{j\sigma} + h.c. + U \sum_{i} n_{i\uparrow} n_{i\downarrow}, \tag{1.1}$$

where $\langle \dots \rangle$ indicates nearest-neighbor sites of the lattice. In the following we will consider the two-dimensional square lattice, but other geometries can be also conceived. In addition, longer-range hopping terms may be also included.

The Hubbard model contains important simplifications of the original problem of electrons in solids. First of all, only one kind of orbital on each ion (with s-wave symmetry, for simplicity) is taken. The motivation is that, in several cases, there is only one band in the vicinity of the Fermi level, which is relevant to determine the low-temperature properties of the material. $c_{i\sigma}$ and $c^{\dagger}_{i\sigma}$ are the creation and annihilation operators for the electrons on the site i with spin σ, and $n_{i\sigma} = c^{\dagger}_{i\sigma} c_{i\sigma}$; $n_i = \sum_{\sigma} n_{i\sigma}$ being the density operator on the site i. t is the hopping amplitude between two nearest-neighbor sites. The second important simplification is to reduce the long-range Coulomb interactions into an on-site electron-electron repulsion. The justification for this approximation is that, in many materials, the Coulomb potential is heavily screened and the effective interaction is therefore short range. The parameter U parametrizes the on-site Coulomb repulsion.

The ground-state properties only depend upon the ratio U/t and the total electron density $n = \sum_{i\sigma} \langle n_{i\sigma} \rangle$. When $U = 0$, the model just describes free electrons, while for $t = 0$ the electrons are localized to minimize the total energy. The half-filled case with $n = 1$ is particularly important, since a metal to (Mott) insulator

transition occurs when increasing the ratio U/t (its actual value depending upon the lattice geometry). Indeed, in the atomic limit $t = 0$, every site is occupied by a single electron, and the system has a large energy gap $\Delta E = U$; by including a small hopping $t \ll U$, this gap is slightly renormalized, but remains finite, implying a Mott insulator. Only when t is considerably large, usually of the order of U, the gap eventually closes and a metallic behavior is reached.

At half-filling for $U \gg t$, well inside the Mott insulator, one can use the perturbation theory to obtain an effective low-energy model. When $t = 0$ the ground state has a huge degeneracy, due to the freedom in having up or down spins on each site. When an infinitesimal hopping is turned on, this degeneracy is lifted by the (second-order) virtual hopping between nearest-neighbor sites: antiparallel spins are favored with respect to parallel ones (see Fig.1.2). Therefore, an antiferromagnetic super-exchange term $J = 4t^2/U$ is generated, leading to the Heisenberg Hamiltonian:

$$H_{Heis} = J \sum_{\langle ij \rangle} \mathbf{S}_i \cdot \mathbf{S}_j, \tag{1.2}$$

where $\mathbf{S}_i = (S_i^x, S_i^y, S_i^z)$ are the quantum spin operators on the site i. Away from half-filling $n \neq 1$, the effective Hamiltonian also contains a hopping term, which is constrained in the subspace with $n_i \leq 1$, i.e., in the subspace without double occupancies:

$$H_{tJ} = -t \sum_{\langle i,j \rangle \sigma} P_G c_{i,\sigma}^\dagger c_{j\sigma} P_G + h.c. + J \sum_{\langle i,j \rangle} \left(\mathbf{S}_i \cdot \mathbf{S}_j - \frac{1}{4} n_i n_j \right), \tag{1.3}$$

here, a nearest-neighbor density-density interaction also appears (at half-filling this term just gives rise to a trivial energy shift). P_G is the projector that constrains the Hilbert space not to contain double occupied sites.

In one dimension, both analytical (e.g., Bethe ansatz [11] or bosonization [27] techniques) and DMRG [14] approaches allowed for a full understanding of several low-energy properties of correlated systems; in particular, DMRG enables highly accurate calculations for systems sufficiently large to approach the thermodynamical limit. In higher dimensions, the situation is much more complex and only very limited regions of the phase diagram are well understood.

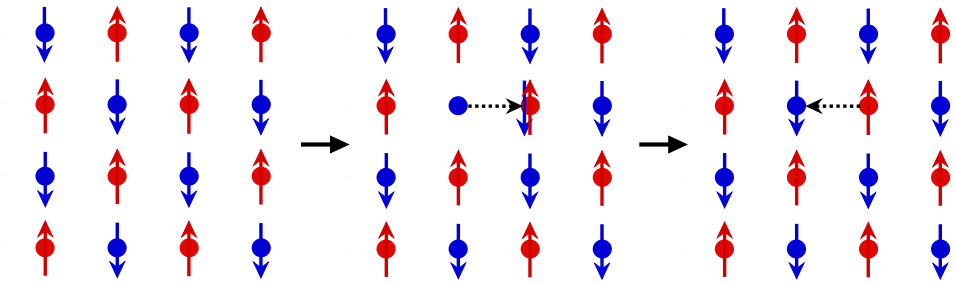

Figure 1.2: Néel order on the square lattice. The dashed lines indicate the second-order virtual hopping.

1.2 The quantum antiferromagnet

On the square lattice, the Heisenberg model with nearest-neighbor interactions displays an antiferromagnetic Néel order at zero temperature: spins have a collinear order with a staggered pattern, defined by the pitch vector $\mathbf{Q} = (\pi, \pi)$. In this regard, quantum Monte Carlo has been extremely powerful and important to finally demonstrate this fact for the spin-half model [28, 29, 30]. After performing the finite-size scaling, the most accurate calculations of the ground-state energy and staggered magnetization gave $\epsilon_0 = -0.669437(5)$ and $M = 0.3070(3)$, respectively.

The Néel antiferromagnet breaks the SU(2) spin-rotational symmetry, having gapless excitations above the ground state (i.e., Goldstone modes). The qualitative description of the Néel phase can be captured by using the Holstein-Primakoff approach to describe the spin operators in the limit of large spin, i.e., $S \gg 1$ [31]. In this spin-wave theory, one starts by assuming the Néel order and then, by introducing the Gaussian fluctuations, the value of classical magnetization is reduced. Excitations over the ground state are magnons that carry $S = 1$.

Before knowing the numerical solution of the $S = 1/2$ Heisenberg model on the square lattice, Anderson suggested that its ground state could be magnetically disordered, especially in presence of frustration (the original Anderson's suggestion referred to the triangular lattice) [32]. In particular, he prompted that a good variational ansatz for the Heisenberg model could be represented by the so-called resonating-valence bond (RVB) state. The RVB state is linear superpositions of

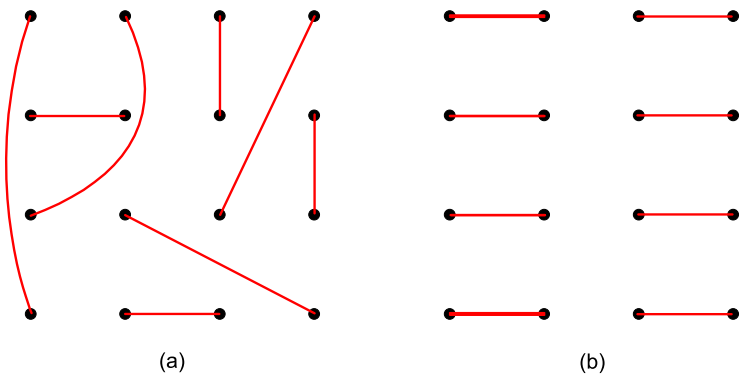

Figure 1.3: (a) and (b) represent two particular valence bond states. The red lines represent the singlet bonds between two spins.

valence-bond states in which each spin of the lattice is coupled with another one to form a singlet:

$$|\Psi_{RVB}\rangle = \sum_i a_i |VB\rangle_i, \tag{1.4}$$

where $|VB\rangle_i$ are valence-bond states. The RVB state is the generalization on a lattice of the Kekulé's suggestion of the π-orbitals of the Benzene molecule. In Fig. 1.3, we show two particular valence-bond states on the square lattice. Depending on the valence-bond states that are included in the sum and the actual weights a_i, RVB states with different properties can be obtained. For example, if only nearest-neighbor singlets are allowed in each $|VB\rangle_i$ and all a_i are equal, we have the so-called short-range RVB state. Here, the spin-spin correlations decay exponentially in space, implying a finite gap in the low-energy excitations. This is the prototype for a gapped spin liquid. If the presence of long-range singlets are allowed in each $|VB\rangle_i$, we have a long-range RVB state. Here, the spin-spin correlations may decay with a power-law behavior, implying gapless spin excitations. These states generically describe magnetically disordered states (even though Liang *et al.* [33] showed that

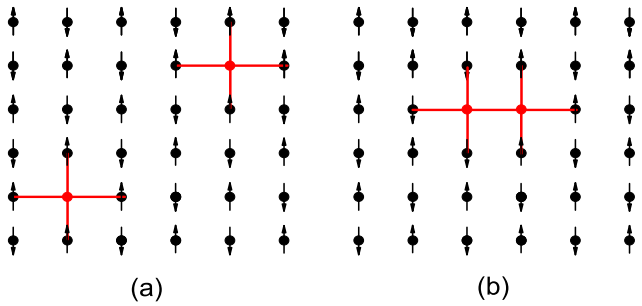

Figure 1.4: Two holes in an antiferromagnet. In the $J \gg t$ limit, the energy loss with respect to the ordered state is given by number of broken bonds (red lines). (a) two holes are widely separated and break 8 bonds, (b) two holes form a pair and break 7 bonds.

for sufficiently long-range singlets a magnetic state can be obtained). In this sense, RVB wave functions are used to describe spin-liquid phases; however, they can also capture valence-bond solids, in which singlets are distributed according to a well-defined pattern, e.g., they are stacked along the rows or columns (see Fig.1.3(b)). Here, although the spin-spin correlations are exponentially decaying, singlet-singlet correlations remain finite at large distances, implying a valence-bond order.

Although the Heisenberg model on the square and triangular lattices is now known to have an antiferromagnetic order at zero temperature, the Anderson's suggestion still remains very appealing when additional terms are added in the model, in order to frustrate the magnetic order. In practice, two ways can be considered to melt antiferromagnetism. The first one, closely related to high-temperature superconductors, is to insert mobile holes into the Heisenberg model and consider the $t-J$ model of Eq.(1.3). In this way, the "preformed" singlets should be poised to become Cooper pairs and lead to superconductivity [2]. The second way is to remain at half filling adding further super-exchange couplings at longer distances. In this way, for sufficiently strong frustration, the magnetic order is definitively suppressed and a

non-magnetic state is stabilized. Nowadays, there are several compounds that are known to possess frustrating interactions, either because of their frustrated lattices (e.g., triangular, Kagomé, etc) or because of the presence of competing antiferromagnetic couplings [34].

In the following two sections we will describe these two cases in detail.

1.3 Doping the Mott insulator

The problem of doped Mott insulators can be studied by considering the $t-J$ Hamiltonian of Eq.(1.3), where the kinetic term acts in the subspace without doubly occupied sites. Similarly, the Hubbard model of Eq.(1.1) can be also considered; however, in this case, the (large) energy scale U overwhelms the (tiny) antiferromagnetic scale $J = 4t^2/U$, implying much harder numerical simulations to reach the correct low-temperature physics.

In general, the kinetic energy tends to delocalize the holes (or the electrons), thus favoring a homogeneous state; on the contrary, the interaction energy would tend to localize particles, implying some inhomogeneous phase in which holes are segregated in a given region of the lattice. The competition between these two terms of the Hamiltonian may give rise to strong charge and spin fluctuations, and eventually to phase separation, charge-density wave (CDW), or spin-density wave (SDW).

In order to understand the charge inhomogeneities in the doped Mott insulator, we take the $t-J$ model and first consider the case of a small hopping compared to the super-exchange coupling, namely $J \gg t$. In this limit, we can neglect the kinetic energy of the holes. Let us denote the energy of the antiferromagnetic state without holes by E_0 and then insert two holes. If these holes are far apart, four antiferromagnetic bonds are broken for each one; this implies that the energy is $E = E_0 + 8BJ$, BJ being the antiferromagnetic energy per bond (see Fig.1.4(a)). By contrast, whenever the holes are close together (to form a pair), the energy is $E = E_0+7BJ$, since one bond is in common (see Fig.1.4(b)). Therefore, it is energetically favorable to cluster together two holes. The argument can be generalized for a finite number of holes. This simple variational calculation suggests that, at least for very large values of J/t, the state where the holes are segregated, leaving the rest of the

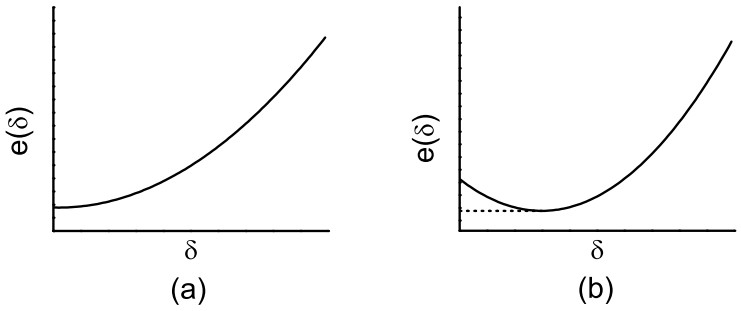

Figure 1.5: Energy per hole $e(\delta)$ as function of doping δ for a stable (a) and unstable (b) system. The dashed line is the Maxwell construction.

system undoped, is favored over the uniform one.

At finite t the loss in antiferromagnetic energy competes with the gain in kinetic energy, and it is not at all obvious if the phase-separated state is still favorite over the homogeneous one. In order to study the presence of phase separation in $t-J$ and Hubbard models, Emery *et al.* [35] suggested to compute the "energy per hole":

$$e(\delta) = \frac{E(\delta) - E(0)}{\delta}, \tag{1.5}$$

here, $E(\delta)$ is the energy per site at hole doping $\delta = N_{hole}/N_{site}$ and $E(0)$ is its value at half filling. For a stable system, $e(\delta)$ must be a monotonically increasing function of δ, since in this case the energy is a convex function of the doping and $e(\delta)$ represents the chord joining half filling and the doping δ. On the other hand, the instability towards phase separation is marked by a minimum at a given δ_c on finite clusters, and a flat behavior up to δ_c in the thermodynamic limit where the Maxwell construction is implied , see Fig.1.5. Although the energy per hole $e(\delta)$ contains the same information as the energy per site $E(\delta)$, the former one gives a much better detector for phase separation than the latter one.

In real materials, a true phase separation is very rare, since electrons are charged and a macroscopic segregation would imply an infinite Coulomb energy; in this regard, the phase separation observed in $La_2CuO_{4+\delta}$ is possible because of the presence of mobile Oxygens in the reservoir layers [36, 37, 38, 39]. Instead of a $\mathbf{q} = 0$ instability, some microscopic segregation with $\mathbf{q} \neq 0$ is possible even in presence of long-range Coulomb interactions [6]. In particular, Emery and Kivelson have suggested that CDW naturally emerges when the Coulomb repulsion is considered on top of a phase-separated system [6]; it has been also suggested that the strong scattering between particles in this regime may also lead to an attraction in the particle-particle channel, thus leading to superconductivity [40].

From the experimental point of view, the so-called striped phase, in which both charge and spin modulations are present, has been observed in a few superconducting materials. The first indication of spin-density modulations has been provided by neutron-scattering studies of $La_{2-x}Sr_xCuO_4$ [41]. Then, Tranquada, *et al.* have shown some evidence that also in the copper-oxide material $La_{1.48}Nd_{0.4}Sr_{0.12}CuO_4$ a phase with spin and possibly charge orders is present [3, 4, 5]. One fingerprint of stripes is the existence of a π-shift, namely by antiparallel spins across the hole-rich domain wall, see Fig. 1 in Introduction.

Motivated by these experimental results, there have been several attempts to detect stripes in simple microscopic Hamiltonians, such as the Hubbard or the $t-J$ models. In particular, by using DMRG [15], and more recently infinite projected entangled-pair states (iPEPS) [16], it has been shown that the ground state of the $t-J$ model may possess stripe order in a rather wide region of hole doping around $\delta = 1/8$. The great success of these methods is that they are able to obtain stripes that are closely related to the ones observed in experiments. However, we would like to emphasize that DMRG and iPEPS are approximate techniques, especially in two spatial dimensions, and their results may not represent the exact ground state. Nevertheless, it must be said that charge fluctuations are very strong in a wide range of the phase diagram. Therefore, small perturbations may drive the system into CDW or striped phases: in this regard, we mention that by considering anisotropies $t_x \neq t_y$ and $J_x \neq J_y$, some evidence of stripes has been found with π-phase shift, which gives rise to incommensurate peaks in the spin structure factor [42].

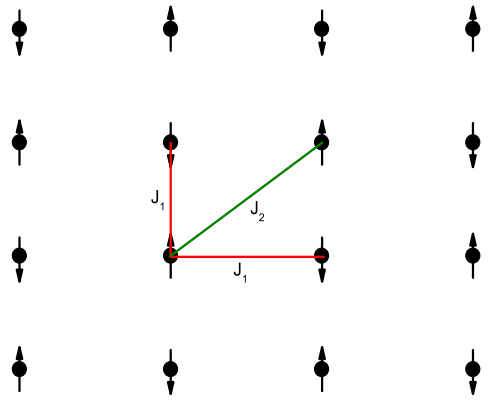

Figure 1.6: Nearest- (J_1) and next-nearest-neighbor (J_2) spin-spin super-exchanges in the two-dimensional square lattice. The second-neighbor interaction frustrates the Néel order.

Although many kinds of models and different methods have been used to study the microscopic mechanics of the phase separation and stripes in the doped quantum antiferromagnet, the actual situation is still not clear and more investigations are definitively needed.

1.4 Adding frustrating super-exchange couplings to the Néel antiferromagnet

The simplest way to add frustration to the simple Heisenberg model is to consider a next-nearest-neighbor super-exchange J_2, so to define the so-called J_1-J_2 Heisenberg model:

$$H_{J_1 J_2} = J_1 \sum_{\langle i,j \rangle} \mathbf{S}_i \cdot \mathbf{S}_j + J_2 \sum_{\langle\langle i,j \rangle\rangle} \mathbf{S}_i \cdot \mathbf{S}_j, \tag{1.6}$$

where $\langle \dots \rangle$ and $\langle\langle \dots \rangle\rangle$ indicate nearest-neighbor and next-nearest-neighbor sites on the square lattice, see Fig. 1.6. In the unfrustrated case with $J_2 = 0$, it is well established that the ground state has Néel long-range order, with a pitch vec-

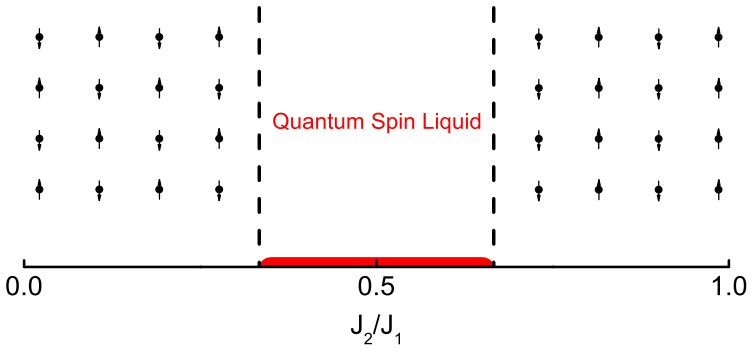

Figure 1.7: The schematic phase diagram of the $J_1 - J_2$ Heisenberg model on the square lattice at zero temperature. Magnetic phases settle down for small J_2/J_1 and large J_2/J_1 values. In between a quantum spin liquid is expected to be stabilized.

tor $\mathbf{Q} = (\pi, \pi)$. For large values of J_2, the ground state shows again a collinear magnetic order with pitch vector $\mathbf{Q} = (\pi, 0)$ or $(0, \pi)$ (this collinear order implies that rotations are broken, besides the translations along one of the two main directions of the lattice). The intermediate regime, around the strongest frustration point $J_2/J_1 = 0.5$, is the most debated one, since the combined effect of frustration and quantum fluctuations destroys antiferromagnetism and leads to a non-magnetic ground state, see Fig. 1.7. However, the nature of this quantum phase is still controversial. Since the pioneering works [43, 44, 45, 46], it was clear that the problem was terribly complicated: many states can be constructed with very similar energies but very different physical properties, e.g., having dimer or plaquette valence-bond order, or being totally disordered with short- or long-range resonating-valence bond fluctuations. Recently, DMRG calculations suggested that a gapped spin liquid without any dimer order is stabilized for $0.4 \lesssim J_2/J_1 \lesssim 0.6$ [17].

Unfortunately, at present, the only known materials whose low-temperature physics may be described by the $J_1 - J_2$ model have either small or large values

of J_2/J_1 [47, 48], falling into magnetic regions. Examples of spin liquids may be found in different two-dimensional materials, having triangular [7, 8] and Kagomé [9] structures.

In order to characterize and describe spin-liquid phases, it is necessary to develop a suitable approach that goes beyond simple mean-field approximations of the original spin Hamiltonian. For this task, different techniques have been devised; here, we will consider a particular one, which is based upon the Abrikosov-fermion representation of the spin operators [49] and is suitable to be implemented in efficient variational Monte Carlo approaches.

1.4.1 Fermionic mean-field approach to spin models and the projective symmetry group

Let us start from a generic model of interacting spin on a lattice:

$$H = \sum_{i,j} J_{ij} \mathbf{S}_i \cdot \mathbf{S}_j, \tag{1.7}$$

where the super-exchange coupling J_{ij} depends on the distance between site i and j. A simple mean-field approximation for the Hamiltonian (1.7) would lead to

$$H = \sum_{i,j} J_{ij} \left[\langle \mathbf{S}_i \rangle \cdot \mathbf{S}_j + \langle \mathbf{S}_j \rangle \cdot \mathbf{S}_i - \langle \mathbf{S}_j \rangle \cdot \langle \mathbf{S}_i \rangle \right], \tag{1.8}$$

clearly, this approximation is not able to capture spin liquids, for which $\langle \mathbf{S}_i \rangle = 0$, since it gives the trivial mean-field model $H = 0$. Therefore, an alternative approach must be decided. The general idea is to re-write the spin operator in terms of more elementary degrees of freedom, which are often called partons. One possibility is to use the so-called Abrikosov-fermion representation of the spin operator [49]:

$$S_i^\mu = \frac{1}{2} c_{i\alpha}^\dagger \sigma_{\alpha\beta}^\mu c_{i\beta}, \tag{1.9}$$

where $\sigma_{\alpha\beta}^\mu$ are the Pauli matrices, and $c_{i\alpha}^\dagger$ ($c_{i\alpha}$) creates (destroys) an electron with spin 1/2. It can be easily verified that this is a faithful representation of the spin operator, i.e., it reproduces the correct commutation relations of the spin operators.

In terms of these fermionic operators, the Heisenberg model (1.7) can be re-written as

$$H = \sum_{i,j} J_{ij}[\frac{1}{4}(n_{i\uparrow} - n_{i\downarrow})(n_{j\uparrow} - n_{j\downarrow}) + \frac{1}{2}(c^\dagger_{i\uparrow}c_{i\downarrow}c^\dagger_{j\downarrow}c_{j\uparrow} + c^\dagger_{j\uparrow}c_{j\downarrow}c^\dagger_{i\downarrow}c_{i\uparrow})]. \tag{1.10}$$

One drawback of considering these new fermionic particles is that their Hilbert space is larger than the original one: for spins, each site has only two states (up or down spin), while for fermions, each site has four possible states, empty, singly occupied (with up or down spin), or doubly occupied. Therefore, in order to describe the spin model, a constraint on each site must be considered:

$$\sum_\sigma c^\dagger_{i\sigma}c_{i\sigma} = 1, \tag{1.11}$$

which implies also that

$$c_{i\sigma}c_{i,-\sigma} = 0. \tag{1.12}$$

Now, a mean-field decoupling can be performed within the fermionic Hamiltonian (1.10):

$$\begin{aligned} H_{MF} &= \sum_{i,j} -\frac{3}{8}J_{ij}[\chi_{ji}\sum_\sigma c^\dagger_{i\sigma}c_{j\sigma} + \eta_{ij}(c^\dagger_{i\uparrow}c^\dagger_{j\downarrow} + c^\dagger_{j\uparrow}c^\dagger_{i\downarrow}) + H.c. - |\chi_{ij}|^2 - |\eta_{ij}|^2] \\ &\quad + \sum_i \{a^3_0(\sum_\sigma c^\dagger_{i\sigma}c_{i\sigma} - 1) + [(a^1_0 + ia^2_0)\sum_\sigma c_{i\sigma}c_{i,-\sigma} + H.c.]\}, \end{aligned} \tag{1.13}$$

where the local constraints (1.11) and (1.12) have been replaced by global ones (i.e., enforcing the single occupancy only on average) and have been introduced by Lagrange multipliers:

$$\langle\textstyle\sum_\sigma c^\dagger_{i\sigma}c_{i\sigma}\rangle = 1, \tag{1.14}$$

$$\langle c_{i\sigma}c_{i,-\sigma}\rangle = 0. \tag{1.15}$$

The mean-field Hamiltonian contains few (complex) parameters, i.e., $\chi_{ij} = 2\langle c^\dagger_{i\uparrow}c_{j\uparrow}\rangle = 2\langle c^\dagger_{i\downarrow}c_{j\downarrow}\rangle$ and $\eta_{ij} = -2\langle c_{i\uparrow}c_{j\downarrow}\rangle = 2\langle c_{i\downarrow}c_{j\uparrow}\rangle$; in addition, a^l_0 ($l = 1, 2, 3$) are the Lagrange multipliers.

At this level, the mean-field Hamiltonian is described by free fermions, the so-called spinons, which carry half of the spin of a usual $S = 1$ magnon excitation. Understanding whether these fractionalized excitations survive beyond the mean-field approximation is crucial to determine the validity of this approach. Therefore, it is important to incorporate some of the important fluctuations that have been neglected. In the following, we will briefly sketch some arguments given by Wen [50] to argue when a stable mean-field state could be expected.

The mean-field Hamiltonian can be re-written in a more compact form by using the doublet:

$$\psi_i = \begin{pmatrix} c_{i\uparrow} \\ c^\dagger_{i\downarrow} \end{pmatrix} \tag{1.16}$$

and the 2×2 matrix:

$$U_{ij} = \begin{pmatrix} \chi^\dagger_{ij} & \eta_{ij} \\ \eta^\dagger_{ij} & -\chi_{ij} \end{pmatrix} = U^\dagger_{ij}, \tag{1.17}$$

which can be written in terms of the identity and the three Pauli matrices:

$$U_{ij} = \chi^I_{ij}\tau_0 + \chi^R_{ij}\tau_3 + \eta^I_{ij}\tau_2 + \eta^R_{ij}\tau_1, \tag{1.18}$$

where τ_0 stands for the identity and χ^R_{ij} (η^R_{ij}) and χ^I_{ij} (η^I_{ij}) indicate the real and imaginary parts of the hopping (pairing) parameters.

Then, we have:

$$H_{MF} = \sum_{i,j} \frac{3}{8} J_{ij} [\frac{1}{2} Tr(U^\dagger_{ij} U_{ij}) - (\psi^\dagger_i U_{ij} \psi_j + H.c.)] + \sum_i a^l_0 \psi^\dagger_i \tau_l \psi_i, \tag{1.19}$$

in addition, the constraints can be written as:

$$\langle \psi^\dagger_i \tau_l \psi_i \rangle = 0. \tag{1.20}$$

It can be verified easily that, given the form of the U_{ij} matrix (1.17), the mean-field Hamiltonian preserves the spin-rotational symmetry.

The mean-field Hamiltonian (1.19) is invariant under a *local* SU(2) transformation $W(i)$:

$$\psi_i \to W(i)\psi_i, \tag{1.21}$$

$$U_{ij} \to W(i) U_{ij} W^\dagger(j). \tag{1.22}$$

This symmetry is usually referred as a *gauge symmetry* of the enlarged fermionic system: the price to be paied when enlarging the Hilbert space, passing from spins to electrons, is the presence of a *redundancy*, which is equivalent to a gauge symmetry. We would like to emphasize that the structure of this emergent gauge structure depends on how the spin operator has been re-written in terms of partons: considering bosons instead of fermions would imply a U(1) structure instead of SU(2). Therefore, this is usually referred as a "high-energy" gauge symmetry [50].

The presence of this gauge symmetry has very important consequences. First of all, let $|\Psi_{MF}^{(U_{ij})}\rangle$ be the ground state of H_{MF}, for a fixed (mean-field) ansatz of U_{ij}. $|\Psi_{MF}^{(U_{ij})}\rangle$ is not a valid state for the original spin problem, since it does not have one electron per site. Now, since the transformation (1.22) does not change the spin operator, we have that $|\Psi_{MF}^{(U_{ij})}\rangle$ and $|\Psi_{MF}^{(W_i U_{ij} W_j^\dagger)}\rangle$ give rise to the same state after projection on the physical Hilbert space:

$$\Psi_{spin}(\{\sigma_i\}) = \langle 0| \prod_i c_{i\sigma_i} |\Psi_{MF}^{(U_{ij})}\rangle = \langle 0| \prod_i c_{i\sigma_i} |\Psi_{MF}^{(W_i U_{ij} W_j^\dagger)}\rangle. \tag{1.23}$$

Therefore, the two ansatze U_{ij} and $U'_{ij} = W_i U_{ij} W_j^\dagger$ label the *same* physical spin state.

However, there may exist ansatze that will give rise to *different* physical states. Indeed, the remarkable aspect is that different spin-liquid states can be obtained, even though all of them have all the symmetries of the microscopic Hamiltonian. As a result, they cannot be distinguished by local symmetries (or order parameters), like in the ordinary Landau theory for classical phase transitions.

Wen [50] was able to make a classifications of *different* spin liquids that may be obtained within this approach. This can be achieved by considering the so-called projective symmetry group (PSG). A PSG is a property of an anstaz U_{ij} and is formed by all the transformations that keep the Ansatz unchanged. A PSG transformation must be a combination of lattice $\mathcal{T}$ and gauge $G_{\mathcal{T}}$ transformations. The invariance of the ansatz under its PSG can be expressed as

$$\mathcal{T}(U_{ij}) = U_{\mathcal{T}(i)\mathcal{T}(j)}, \tag{1.24}$$

$$G_{\mathcal{T}}(U_{ij}) = G_{\mathcal{T}}(i) U_{ij} G_{\mathcal{T}}^\dagger(j), \tag{1.25}$$

$$G_{\mathcal{T}}\mathcal{T}(U_{ij}) = U_{ij}, \tag{1.26}$$

where $G_{\mathcal{T}}(i) \in SU(2)$. $G_{\mathcal{T}}\mathcal{T}$ defines the PSG for the ansatz U_{ij}. We would like to emphasize that, given the presence of the local gauge symmetry, a totally symmetric physical state may be obtained even by considering a less symmetric ansatz U_{ij}. Eq.(1.26) expresses the condition to obtain a symmetric state when considering the gauge transformations (i.e., for having a symmetric state after projection).

The PSG for two gauge-equivalent ansatze U_{ij} and $W(U_{ij}) = W(i)U_{ij}W^{\dagger}(j)$ are related: if $G_{\mathcal{T}}\mathcal{T}$ is the PSG for U_{ij}, then $WG_{\mathcal{T}}\mathcal{T}W^{-1}$ is the PSG for $W(U_{ij})$.

Every PSG contains a special subgroup, the invariant gauge group (IGG): all the gauge transformations that leave the ansatz unchanged:

$$\mathcal{G} = \{G_i | G_i U_{ij} G_j^{\dagger} = U_{ij}, G_i \in SU(2)\}. \tag{1.27}$$

Using PSG and IGG, we can classify spin liquid phases. The crucial point is that, given the lattice symmetries $\mathcal{T}$ (i.e., translations, rotations, and reflections) and possibly also time reversal, *different* sets of gauge transformations $G_{\mathcal{T}}$ can be found to fulfill Eq.(1.26). Each set of transformations defines a PSG and, therefore, a spin liquid. Thus, even though all spin liquids have the *same* symmetries, they are characterized by a *different* set of transformations that leave the ansatz unchanged.

Wen argued that the IGG defines the important gauge fluctuations around the mean-field ansatz, i.e., the "low-energy" gauge fluctuations. The IGG can have SU(2), U(1), or Z_2 symmetry, defining SU(2), U(1), or Z_2 spin liquids, respectively. Similarly, a first distinction among spin liquids may be done by considering SU(2) fluxes for loops with a given base site, in which the loop starts and ends. For example, we can consider a loop C with a base point i such that $i \to i+x \to i+x+y \to i+y \to i$; the SU(2) flux is given by $P_C = U_{i,i+x}U_{i+x,i+x+y}U_{i+x+y,i+y}U_{i+y,i}$. P_C is a 2×2 matrix that results from the multiplications of the U_{ij} for different bonds. P_C can be written in terms of the identity and the three Pauli matrices. Under a gauge transformation (1.22), the flux P_C changes as:

$$P_C \to W(i)P_C W^{\dagger}(i), \tag{1.28}$$

involving only the matrix $W(i)$ at the site i.

Wen [50, 51] argued that if the SU(2) flux P_C for *all* loops is trivial $P_C \propto \tau_0$, then the SU(2) gauge structure is unbroken. This is the case when $\eta = 0$ or when $\chi = \eta$

in the mean-field ansatz. When the flux P_C is non-trivial but all possible fluxes with different loops commute with each other, then the SU(2) gauge structure is broken down to U(1). Finally, when there are fluxes that do not commute, then the SU(2) gauge structure is broken down to Z_2.

A Z_2 gauge interaction is particularly important, since it is gapped and thus irrelevant at low energies: in this case one would expect that the mean-field picture is not destroyed when putting back fluctuations. The expectation is that spinons remain free fermions at low energies.

Let us finish this section by illustrating how it is possible to classify Z_2 spin liquids by using the PSG and the IGG in a particularly simple case, where only translational symmetries are considered. The more difficult case, with translations, reflections, and time-reversal symmetries can be found in Ref.[50].

In this case the IGG is Z_2 and contains two elements:

$$\mathcal{G} = Z_2 = \{G_1, G_2\}. \tag{1.29}$$

$$G_1(i) = \tau_0 \quad G_2(i) = -\tau_0. \tag{1.30}$$

First of all, we can use the local SU(2) gauge transformations to obtain SU(2) fluxes that do not depend upon the site i. Then, the translational invariance of the fluxes implies that:

$$G_{T_x}(i) = \pm\tau_0 \quad G_{T_y}(i) = \pm\tau_0. \tag{1.31}$$

Then, we note that the gauge transformations of the form $W(i) = \pm\tau_0$ do not change the translation-invariant property of the loop operators. Thus we can use such gauge transformations to further simplify G_{T_x} and G_{T_y}. First, we can choose a gauge to make

$$G_{T_y}(i) = \tau_0. \tag{1.32}$$

Then, we note that a gauge transformation $W(i) = W(i_x)$ does not change the condition $G_{T_y}(i) = \tau_0$ and can be used to fix:

$$G_{T_x}(i_x, i_y = 0) = \tau_0. \tag{1.33}$$

Finally, since the translations in x and y directions commute, we have

$$\begin{aligned} & G_{T_x}T_xG_{T_y}T_y(G_{T_x}T_x)^{-1}(G_{T_y}T_y)^{-1} \\ = \; & G_{T_x}(i)G_{T_y}(i-x)G_{T_x}^{-1}(i-y)G_{T_y}^{-1}(i) \in \mathcal{G}. \end{aligned} \tag{1.34}$$

By using Eq.(1.32), we have:

$$G_{T_x}(i)G_{T_x}^{-1}(i-y) = \pm\tau_0. \tag{1.35}$$

Therefore, two solutions are possible:

$$G_{T_x}(i) = \tau_0, \tag{1.36}$$

$$G_{T_x}(i) = (-1)^{i_y}\tau_0, \tag{1.37}$$

which are referred as Z2A and Z2B, respectively [50]. The two ansatze corresponding to these solutions are given by

$$U_{i,i+m} = U_m, \tag{1.38}$$

and

$$U_{i,i+m} = (-1)^{m_y i_x}U_m, \tag{1.39}$$

and correspond to a translational invariant ansatz (1.38) and an ansatz with a 2×1 unit cell (1.39).

In Ref.[50], the full classification of Z_2 spin liquids, by using translations, reflections, and time-reversal symmetries, has been worked out. It can be divided into two classes:

$$\begin{aligned} G_{T_x}(i) = \tau_0, \quad & G_{T_y}(i) = \tau_0, \\ G_{P_x}(i) = \eta_{xpx}^{i_x}\eta_{xpy}^{i_y}g_{P_x}, \quad & G_{P_y}(i) = \eta_{xpy}^{i_x}\eta_{xpx}^{i_y}g_{P_y}, \\ G_{P_{xy}}(i) = g_{P_{xy}}, \quad & G_T(i) = \eta_t^i g_T, \end{aligned} \tag{1.40}$$

and

$$\begin{aligned} G_{T_x}(i) = (-1)^{i_y}\tau_0, \quad & G_{T_y}(i) = \tau_0, \\ G_{P_x}(i) = \eta_{xpx}^{i_x}\eta_{xpy}^{i_y}g_{P_x}, \quad & G_{P_y}(i) = \eta_{xpy}^{i_x}\eta_{xpx}^{i_y}g_{P_y}, \\ G_{P_{xy}}(i) = (-1)^{i_x i_y}g_{P_{xy}}, \quad & G_T(i) = \eta_T^i g_T. \end{aligned} \tag{1.41}$$

Here η^i can be 1 or -1. g_P is the operator obtained by considering three parity symmetries (i.e., P_x: $(i_x, i_y) \to (-i_x, i_y)$, P_y: $(i_x, i_y) \to (i_x, -i_y)$, and P_{xy}: $(i_x, i_y) \to (-i_x, -i_y)$). g_T is obtained by considering time-reversal symmetry (i.e., T: $U_{ij} \to -U_{ij}$). They are listed from Eq.(1.42) to (1.58):

$$g_{P_{xy}} = \tau_0, \quad g_{P_x} = \tau_0, \quad g_{P_y} = \tau_0, \quad g_T = \tau_0, \tag{1.42}$$
$$g_{P_{xy}} = \tau_0, \quad g_{P_x} = i\tau_3, \quad g_{P_y} = i\tau_3, \quad g_T = \tau_0, \tag{1.43}$$
$$g_{P_{xy}} = i\tau_3, \quad g_{P_x} = \tau_0, \quad g_{P_y} = \tau_0, \quad g_T = \tau_0, \tag{1.44}$$
$$g_{P_{xy}} = i\tau_3, \quad g_{P_x} = i\tau_3, \quad g_{P_y} = i\tau_3, \quad g_T = \tau_0, \tag{1.45}$$
$$g_{P_{xy}} = i\tau_3, \quad g_{P_x} = i\tau_1, \quad g_{P_y} = i\tau_1, \quad g_T = \tau_0, \tag{1.46}$$
$$g_{P_{xy}} = \tau_0, \quad g_{P_x} = \tau_0, \quad g_{P_y} = \tau_0, \quad g_T = i\tau_3, \tag{1.47}$$
$$g_{P_{xy}} = \tau_0, \quad g_{P_x} = i\tau_3, \quad g_{P_y} = i\tau_3, \quad g_T = i\tau_3, \tag{1.48}$$
$$g_{P_{xy}} = \tau_0, \quad g_{P_x} = i\tau_1, \quad g_{P_y} = i\tau_1, \quad g_T = i\tau_3, \tag{1.49}$$
$$g_{P_{xy}} = i\tau_3, \quad g_{P_x} = \tau_0, \quad g_{P_y} = \tau_0, \quad g_T = i\tau_3, \tag{1.50}$$
$$g_{P_{xy}} = i\tau_3, \quad g_{P_x} = i\tau_3, \quad g_{P_y} = i\tau_3, \quad g_T = i\tau_3, \tag{1.51}$$
$$g_{P_{xy}} = i\tau_3, \quad g_{P_x} = i\tau_1, \quad g_{P_y} = i\tau_1, \quad g_T = i\tau_3, \tag{1.52}$$
$$g_{P_{xy}} = i\tau_1, \quad g_{P_x} = \tau_0, \quad g_{P_y} = \tau_0, \quad g_T = i\tau_3, \tag{1.53}$$
$$g_{P_{xy}} = i\tau_1, \quad g_{P_x} = i\tau_3, \quad g_{P_y} = i\tau_3, \quad g_T = i\tau_3, \tag{1.54}$$
$$g_{P_{xy}} = i\tau_1, \quad g_{P_x} = i\tau_1, \quad g_{P_y} = i\tau_1, \quad g_T = i\tau_3, \tag{1.55}$$
$$g_{P_{xy}} = i\tau_1, \quad g_{P_x} = i\tau_2, \quad g_{P_y} = i\tau_2, \quad g_T = i\tau_3, \tag{1.56}$$
$$g_{P_{xy}} = i\frac{\tau_1 + \tau_2}{\sqrt{2}}, \quad g_{P_x} = i\tau_1, \quad g_{P_y} = i\tau_2, \quad g_T = \tau_0, \tag{1.57}$$
$$g_{P_{xy}} = i\frac{\tau_1 + \tau_2}{\sqrt{2}}, \quad g_{P_x} = i\tau_1, \quad g_{P_y} = i\tau_2, \quad g_T = i\tau_3. \tag{1.58}$$

The following scheme can be used to label different PSG's:

$$Z2A(g_{P_x})_{\eta^{ix}_{xpx}}(g_{P_y})_{\eta^{ix}_{xpy}} g_{P_{xy}}(g_T)_{\eta_t}, \tag{1.59}$$
$$Z2B(g_{P_x})_{\eta^{ix}_{xpx}}(g_{P_y})_{\eta^{ix}_{xpy}} g_{P_{xy}}(g_T)_{\eta_t}. \tag{1.60}$$

The label $Z2A\ldots$ corresponds to the case of Eq.(1.40), and the label $Z2B\ldots$ corresponds to the case of Eq.(1.41). An abbreviated notation can be obtained by

replacing $(\tau_{0,+}, \tau_{1,+}, \tau_{2,+}, \tau_{3,+})$ by $(0, 1, 2, 3)$ and $(\tau_{0,-}, \tau_{1,-}, \tau_{2,-}, \tau_{3,-})$ by (n, x, y, z). As an example, the spin liquid $Z2Azz13$ is $Z2A\tau_{3,-}\tau_{3,-}\tau_{1,+}\tau_{3,+}$.

Remarkably 272 different solutions for the PSG have been found. Although some of them do not give rise to acceptable ansatze U_{ij}, within this approach, there should be at most 196 different spin liquids.

Chapter 2

Numerical Methods

The independent-electron approximation is known to dramatically fail in strongly-correlated systems, which cannot be easily handled with analytical tools. Therefore numerical methods are needed, and recently many kinds of techniques have been introduced to study strongly correlated systems. In this chapter, we will briefly describe the methods used in this thesis, including the exact diagonalization/Lanczos method and the quantum Monte Carlo technique.

In the first section, we will discuss how to diagonalize exactly the Hamiltonian matrix by using the Lanczos method. However, because of the memory limitation, this method can be used only on small lattice sizes. In order to overcome this problem, we have to consider statistical methods: starting from the second section, we will introduce the quantum Monte Carlo methods.

The core of Monte Carlo approach is the Metropolis algorithm [52], which generates a random walk in the configuration space, this sequence of configurations is called a Markov chain. The configurations are sampled during the random walk, according to a given stationary probability distribution that obtained after a certain number of steps to reach equilibrium. Since the general principles of the Monte Carlo methods can be found in many textbooks, we will focus on the implementation of Monte Carlo in the quantum problems. We will show that very efficient algorithms allow us to describe very large systems with good accuracy, by means of the variational Monte Carlo, the Green's function Monte Carlo, and the stochastic minimization. Also, we will describe how to apply few Lanczos steps to the given

variational wave function, which can be therefore systematically improved with this technique.

2.1 Lanczos

Generally the ground state $|\Phi_0\rangle$ of the Hamiltonian H can be obtained by the power method from a trial wave function $|\Psi_T\rangle$, which is nonorthogonal to $|\Phi_0\rangle$. In the power method, we define the operator $\Lambda - H$, where Λ is a suitable constant, allowing the convergence to the ground state of H. Indeed, after many iterations, we have that:

$$(\Lambda - H)^n |\Psi_T\rangle = (\Lambda - E_0)^n \left[\alpha_0 |\Phi_0\rangle + \sum_{i \neq 0} \left(\frac{\Lambda - E_i}{\Lambda - E_0} \right)^n \alpha_i |\Phi_i\rangle \right], \tag{2.1}$$

where E_i and $|\Phi_i\rangle$ are the eigenvalues and eigenvectors of H, and $\alpha_i = \langle \Phi_i | \Psi_T \rangle$. By taking Λ such that $\frac{|\Lambda - E_i|}{|\Lambda - E_0|} < 1$, when n goes to infinity, we obtain

$$|\Phi_0\rangle \sim \lim_{n \to \infty} (\Lambda - H)^n |\Psi_T\rangle, \tag{2.2}$$

namely, the ground state is filtered by the iterative approach of $(\Lambda - H)$.

Starting from the power method, where the ground state is approximated by a single power, $|\Phi_0\rangle \sim (\Lambda - H)^n |\Psi_T\rangle$, we can define a much more efficient iterative procedure, the Lanczos method, where the information contained in all the powers, from 1 to n, is used,

$$|\Phi_0\rangle \sim \sum_{i=1}^{n} \alpha_i H^i |\Psi_T\rangle. \tag{2.3}$$

In the Lanczos method, an orthogonal basis is constructed, in contrast to the power method, in which the vectors are not orthogonal. The orthogonal vectors can be defined by the following formula:

$$b_{n+1} |\Psi_{n+1}\rangle = H |\Psi_n\rangle - a_n |\Psi_n\rangle - b_n |\Psi_{n-1}\rangle, \tag{2.4}$$

for $n = 1, 2, 3, ...$, with $|\Psi_0\rangle = 0$, $b_1 = 0$, and

$$a_n = \langle \Psi_n | H | \Psi_n \rangle, \tag{2.5}$$

$$b_n = \langle \Psi_{n+1} | H | \Psi_n \rangle. \tag{2.6}$$

The initial vector $|\Psi_1\rangle = |\Psi_T\rangle$ can be randomly chosen, in order to have a non-zero overlap with the true ground state $\langle\Psi_1|\Phi_0\rangle \neq 0$. Based on these definitions, it is easy to prove that $|\Psi_n\rangle$ is orthogonal with $|\Psi_{n-1}\rangle$ and $|\Psi_{n+1}\rangle$. Moreover by using this basis, the Hamiltonian has a tridiagonal form

$$H = \begin{pmatrix} a_1 & b_2 & 0 & 0 & ... \\ b_2 & a_2 & b_3 & 0 & ... \\ 0 & b_3 & a_3 & b_4 & ... \\ 0 & 0 & b_4 & a_5 & ... \\ ... & ... & ... & ... & ... \end{pmatrix}. \tag{2.7}$$

Once in this form, the matrix can be easily diaganolized by using standard library routines. The main advantage of the Lanczos method is that a small number of iterations (typically about $100 \sim 200$, depending on the model) is sufficient to get a very high accuracy for the exact ground state:

$$|\Phi_0\rangle \approx \sum_{n=1}^{\sim 100} c_i |\Psi_n\rangle. \tag{2.8}$$

The main limitation of this technique is that the Hilbert space grows exponentially with the number of particles and even small lattices may require a huge computer memory. For example, for the $t - J$ model, where each site can be either empty or singly occupied, the Hilbert space can be as large as several millions of states for about 2/4 holes on 26 sites. In order to alleviate this problem, we can make use of lattice symmetries and work in distinct subspaces of the Hamiltonian.

2.2 Variational Monte Carlo

As mentioned in the previous section, due to the exponential growth of the Hilbert space, exact calculations can be performed only on small clusters. On large lattice sizes, one must devise alternative methods: the variational Monte Carlo approach is one possible choice. The key point of the variational Monte Carlo approach is the variational principle in quantum mechanics: the expectation value of a given Hamiltonian H over any trial wave function $|\Psi_v\rangle$, E_v, is always higher than the

ground-state energy E_0,

$$E_v = \frac{\langle\Psi_v|H|\Psi_v\rangle}{\langle\Psi_v|\Psi_v\rangle} \geq E_0. \tag{2.9}$$

This can be easily derived by inserting the complete set of eigenvectors $|\Phi_i\rangle$ of the Hamiltonian H with eigenvalues E_i,

$$\begin{aligned} E_v &= \frac{\langle\Psi_v|H|\Psi_v\rangle}{\langle\Psi_v|\Psi_v\rangle} = \sum_i E_i \frac{|\langle\Phi_i|\Psi_v\rangle|^2}{\langle\Psi_v|\Psi_v\rangle} \\ &= E_0 + \sum_{i\neq 0}(E_i - E_0)\frac{|\langle\Phi_i|\Psi_v\rangle|^2}{\langle\Psi_v|\Psi_v\rangle}, \end{aligned} \tag{2.10}$$

since $E_i > E_0$, we have

$$E_v \geq E_0. \tag{2.11}$$

In the variational Monte Carlo, a stochastic process is defined in a given basis $|x\rangle$, in order to evaluate expectation values of various operators. Here, we introduce the complete sets of basis $|x\rangle$, where the electrons occupy the sites on the lattice, $|x\rangle = c^\dagger_{R_1} c^\dagger_{R_2} ...|0\rangle$. Then we insert this basis into the expectation value:

$$E_v = \frac{\langle\Psi_v|H|\Psi_v\rangle}{\langle\Psi_v|\Psi_v\rangle} = \frac{\sum_{x,x'}\Psi_v(x')H_{x',x}\Psi_v(x)}{\sum_x \Psi_v^2(x)} = \sum_x \frac{E_x\Psi_v^2(x)}{\sum_{x'}\Psi_v^2(x')}, \tag{2.12}$$

with $\Psi_v(x) = \langle x|\Psi\rangle$ and $H_{x',x} = \langle x'|H|x\rangle$. The local energy is

$$E_x = \frac{\langle\Psi_v|H|x\rangle}{\langle\Psi_v|x\rangle} = \sum_{x'} \frac{\Psi_v(x')}{\Psi_v(x)} H_{x',x}. \tag{2.13}$$

A stochastic algorithm can be defined to generate a sequence of configurations $\{|x_n\rangle\}$ in the Hilbert space (the so-called Markov chain) by using $P(x)$ as the probability distribution

$$P(x) = \frac{\Psi_v^2(x)}{\sum_{x'}\Psi_v^2(x')}. \tag{2.14}$$

In practice, the Metropolis algorithm [52] is the easiest way to generate configurations according to the probability distribution $P(x)$. Given one configuration x,

the new configuration x' is proposed and then accepted if the following condition is satisfied:

$$\xi < \frac{P(x')}{P(x)} = \left[\frac{\Psi_v(x')}{\Psi_v(x)}\right]^2, \tag{2.15}$$

where ξ is a random number uniformly distributed in the interval between 0 and 1. Otherwise the old configuration will be kept, $x' = x$. Then we can calculate the expectation value as the average of E_x over the sampled configurations:

$$E_v \approx \frac{1}{N}\sum_{n=1}^{N} E_{x_n}, \tag{2.16}$$

where N is the number of configurations generated in the Markov chain.

In the variational Monte Carlo, it is possible to calculate any kind of expectation value over a given wave function in a similar way

$$\langle O\rangle_v = \sum_x \frac{O_x \Psi_v^2(x)}{\sum_{x'} \Psi_v^2(x')}, \tag{2.17}$$

where

$$O_x = \sum_{x'} \frac{\Psi_v(x')}{\Psi_v(x)} O_{x',x}. \tag{2.18}$$

Within the variational Monte Carlo approach, different trial wave functions can be considered, in order to improve the energy expectation value. In the present thesis, we have chosen projected mean-field states, defined as:

$$|\Psi_v\rangle = \mathcal{P}_J |MF\rangle. \tag{2.19}$$

$|MF\rangle$ is defined by a mean field Hamiltonian. The projector $\mathcal{P}_J$ introduces correlations into the wave function, and is diagonal in the basis $\{|x\rangle\}$

$$\Psi_v(x) = \langle x|\Psi_v\rangle = \mathcal{P}_J(x)\langle x|MF\rangle, \tag{2.20}$$

where $\langle x|MF\rangle$ is a determinant. During the Markov chain, the calculation of ratios like $\frac{\langle x'|\Psi_v\rangle}{\langle x|\Psi_v\rangle}$ is needed, both for the Metropolis algorithm and for the local energy (2.13). A straightforward calculation of the determinant would require $O(N_{site}^3)$ operations; however, whenever $|x'\rangle$ and $|x\rangle$ differ for only few electron positions, it is possible to compute the ratio $\frac{\langle x'|MF\rangle}{\langle x|MF\rangle}$ by using a fast algorithm with $O(1)$ operations. In this way, the core of the variational calculations is $O(N_{site}^2)$, corresponding to the update of Green's function $\frac{\langle x|c_{R_1}^\dagger c_{R_2}|MF\rangle}{\langle x|MF\rangle}$ [53].

2.3 The Minimization Algorithm

Let us consider the variational wave function $|\Psi_v(\alpha)\rangle$, which depends on a set of variational parameters $\alpha = \{\alpha_k\}$ $(k = 1, 2, ..., p)$; then, the energy $E_v(\alpha)$ calculated over $|\Psi_v(\alpha)\rangle$ also depends on α. We want to define an iterative scheme to optimize the variational energy, within the ansatz described by $|\Psi_v(\alpha)\rangle$. Here, we use the stochastic reconfiguration (SR) method: starting from $|\Psi_v(\alpha)\rangle$, we define

$$|\Psi_{\Lambda-H}\rangle = (\Lambda - H)|\Psi_v(\alpha)\rangle, \tag{2.21}$$

where Λ is a suitable large constant such that $|\Psi_{\Lambda-H}\rangle$ has a lower energy than $|\Psi_v(\alpha)\rangle$. Since the state $|\Psi_{\Lambda-H}\rangle$ will not have the defined functional parameters by α, we have to find the best possible approximation $|\Psi_v(\alpha')\rangle$ for it. Therefore we also considered the state obtained by slightly changing the parameters $\alpha' = \alpha + \delta\alpha$. Within the linear approximation:

$$|\Psi_v(\alpha')\rangle \approx |\Psi_v(\alpha)\rangle + \sum_{k=1}^{p} \delta\alpha_k \frac{\partial|\Psi_v(\alpha)\rangle}{\partial\alpha_k} = \left[1 + \sum_{k=1}^{p} \delta\alpha_k O_k\right] |\Psi_v(\alpha)\rangle, \tag{2.22}$$

where the operator O_k is defined through the matrix elements

$$\begin{aligned} \langle x|O_k|x'\rangle &= O_k(x)\delta_{x,x'}, \\ O_k(x) &= \tfrac{\partial \ln\langle x|\Psi_v(\alpha)\rangle}{\partial\alpha_k}. \end{aligned} \tag{2.23}$$

Defining $O_0 = 1$, we have

$$|\Psi_v(\alpha')\rangle = \sum_{k=0}^{p} \delta\alpha_k O_k|\Psi_v(\alpha)\rangle, \tag{2.24}$$

where $\delta\alpha_0$ is related to an irrelevant normalization of the wave function.

Then we equal $|\Psi_{\Lambda-H}\rangle$ and $|\Psi_v(\alpha')\rangle$ in a restricted subspace defined by $O_k|\Psi_v(\alpha)\rangle$, for $k = 0, ..., p$:

$$\langle\Psi_v(\alpha)|O_k(\Lambda - H)|\Psi_v(\alpha)\rangle = \sum_{k'=0}^{p} \delta\alpha_{k'}\langle\Psi_v(\alpha)|O_k O_{k'}|\Psi_v(\alpha)\rangle, \tag{2.25}$$

which can be written as

$$f_k = \sum_{k'=0}^{p} \delta\alpha_{k'} S_{kk'}, \tag{2.26}$$

where

$$f_k = \frac{\langle \Psi_v(\alpha)|O_k(\Lambda - H)|\Psi_v(\alpha)\rangle}{\langle \Psi_v(\alpha)|\Psi_v(\alpha)\rangle}, \tag{2.27}$$

$$S_{kk'} = \frac{\langle \Psi_v(\alpha)|O_k O_{k'}|\Psi_v(\alpha)\rangle}{\langle \Psi_v(\alpha)|\Psi_v(\alpha)\rangle}. \tag{2.28}$$

This is a set of $(p+1)$ linear equations, where the unknown $\delta\alpha_k$ can be easily obtained by inverting the matrix $S_{kk'}$. Indeed, we can easily decouple the equation for $k = 0$ from the other p equations. When $k = 0$, we have $f_0 = \Lambda - E_v(\alpha)$, then

$$\delta\alpha_0 = \Lambda - E_v(\alpha) - \sum_{k=1}^{p} \delta\alpha_k S_{0k}. \tag{2.29}$$

Combining Eq.(2.26) and Eq.(2.29), we obtain

$$f_k^{Red} = \sum_{k'=1}^{p} \delta\alpha_{k'} S_{kk'}^{Red}, \tag{2.30}$$

where

$$f_k^{Red} = \frac{\langle \Psi_v(\alpha)|O_k|\Psi_v(\alpha)\rangle}{\langle \Psi_v(\alpha)|\Psi_v(\alpha)\rangle} \frac{\langle \Psi_v(\alpha)|H|\Psi_v(\alpha)\rangle}{\langle \Psi_v(\alpha)|\Psi_v(\alpha)\rangle} - \frac{\langle \Psi_v(\alpha)|O_k H|\Psi_v(\alpha)\rangle}{\langle \Psi_v(\alpha)|\Psi_v(\alpha)\rangle}, \tag{2.31}$$

$$S_{kk'}^{Red} = S_{kk'} - S_{k0}S_{k'0}. \tag{2.32}$$

Notice that

$$f_k^{Red} = -\frac{1}{2}\frac{\partial E_v(\alpha)}{\partial \alpha_k}. \tag{2.33}$$

In practice, we perform N Metropolis steps to calculate the observables of Eq.(2.31) and (2.32), then solve the linear equations of Eq.(2.30) in order to get the variations $\{\delta\alpha_k\}$, so to update the variational parameters $\{\alpha_k\}$ into $\{\alpha'_k\}$. The new wave function $|\Psi_v(\alpha')\rangle$ is considered as the starting state, and we perform a new set of iterations, until the convergence is reached.

At equilibrium, $\frac{\partial E_v(\alpha)}{\partial \alpha_k} = 0$, implying that $\delta\alpha_k = 0$, corresponding to the variational minimum. Moreover, the definition in Eq.(2.31) with $f_k^{Red} = 0$ implies that the variational wave function has the same property of the exact eigenstate,

$$\langle O_k\rangle\langle H\rangle = \langle O_k H\rangle. \tag{2.34}$$

In principle the SR approach is similar to the standard steepest descent (SD) method; indeed, the SR iteration corresponds to the following parameter changes:

$$\delta\alpha_k \to \delta\alpha_k + \Delta t \sum_{k'} (S^{Red}_{k,k'})^{-1} f^{Red}_{k'}, \tag{2.35}$$

while the SD method has $(S^{Red})^{-1} = \delta_{k,k'}$. The advantage of SR with respect to SD comes from the fact that the energy landscape may strongly depend upon various parameters (i.e., some parameters may affect the energy values more than others), the presence of the covariance matrix $S^{Red}_{kk'}$ takes into account this fact, giving different convergence rates to the variational parameters.

2.4 Few Lanczos Steps

For a given trial wave function $|\Psi_v\rangle$, we can systematically improve its accuracy by applying p Lanczos steps:

$$|\Psi_{\beta_1 \ldots \beta_p}\rangle = \sum_{i=0}^{p} \beta_i H^i |\Psi_v\rangle. \tag{2.36}$$

where $\beta_0 = 1$, and β_i $(i \neq 0)$ are the Lanczos variational parameters. $p = 0$ means the pure variational calculation without any Lanczos step. Using this improved wave function, we can calculate the expectation value of the Hamiltonian H,

$$\begin{aligned} E_{\{\beta_i\}} &= \frac{\langle \Psi_{\{\beta_i\}} | H | \Psi_{\{\beta_i\}} \rangle}{\langle \Psi_{\{\beta_i\}} | \Psi_{\{\beta_i\}} \rangle} \\ &= \frac{\sum_{i,j} \beta_i \beta_j \langle \Psi_v | H^{i+j+1} | \Psi_v \rangle}{\sum_{i,j} \beta_i \beta_j \langle \Psi_v | H^{i+j} | \Psi_v \rangle}. \end{aligned} \tag{2.37}$$

From this equation, in order to compute $E_{\{\beta_i\}}$, we need all moments $\langle \Psi_v | H^n | \Psi_v \rangle$ up to the order $n = 2p + 1$. In principle, a straightforward calculation of all moments can be exactly obtained. However, in practice, the time required for the evaluating them grows exponentially with the dimension of the Hilbert space, which gives serious computational limitations. On the other hand, all moments can be evaluated stochastically, but this approach will induce large statistical errors, which strongly affect the final expectation value of Hamiltonian. In this thesis we implement few Lanczos steps exactly, i.e., $p = 1$ and 2.

In the case of $p = 1$, it is possible to evaluate the expectation value of the Hamiltonian over

$$|\Psi_\beta\rangle = (1 + \beta H)|\Psi_v\rangle, \tag{2.38}$$

with a reasonable computer time. We have

$$E^{(1)} = \sum_x \frac{E_x^\beta \Psi_\beta^2(x)}{\sum_x \Psi_\beta^2(x)}, \tag{2.39}$$

where $\Psi_\beta(x) = \langle x|\Psi_\beta\rangle$, and the local energy E_x^β is

$$E_x^\beta = \sum_{x'} H_{x',x} \frac{\Psi_\beta(x')}{\Psi_\beta(x)}. \tag{2.40}$$

We can use the Monte Carlo method to sample the expectation value $E^{(1)}$ by generating the configurations according to the probability distribution $\frac{\Psi_\beta^2(x)}{\sum_x \Psi_\beta^2(x)}$. For the Metropolis algorithm, we need the ratio

$$\frac{\Psi_\beta(x')}{\Psi_\beta(x)} = \frac{\langle x'|(1 + \beta H)|\Psi_v\rangle}{\langle x|(1 + \beta H)|\Psi_v\rangle} = \frac{\Psi_v(x')}{\Psi_v(x)} \left(\frac{1 + \beta E_{x'}}{1 + \beta E_x}\right). \tag{2.41}$$

This shows that we need to calculate the local energy of the trial wave function both on the configuration $|x\rangle$ and $|x'\rangle$ at each Monte Carlo step, even if x' is proposed as the new configuration and not accepted.

For the second Lanczos step $p = 2$, we have the similar equations. Now we have two Lanczos parameters,

$$|\Psi_{\beta_1\beta_2}\rangle = (1 + \beta_1 H + \beta_2 H^2)|\Psi_v\rangle. \tag{2.42}$$

The expectation value of Hamiltonian is more complicated

$$E^{(2)} = \sum_x \frac{E_x^{\beta_1\beta_2} \Psi_{\beta_1\beta_2}^2(x)}{\sum_x \Psi_{\beta_1\beta_2}^2(x)}, \tag{2.43}$$

with

$$E_x^{\beta_1\beta_2} = \sum_{x'} H_{x',x} \frac{\Psi_{\beta_1\beta_2}(x')}{\Psi_{\beta_1\beta_2}(x)}. \tag{2.44}$$

The ratio for the Metropolis algorithm is given by

$$\frac{\Psi_{\beta_1\beta_2}(x')}{\Psi_{\beta_1\beta_2}(x)} = \frac{\langle x'|(1+\beta_1 H+\beta_2 H^2)|\Psi_v\rangle}{\langle x|(1+\beta_1 H+\beta_2 H^2)|\Psi_v\rangle} = \frac{\Psi_v(x')}{\Psi_v(x)}\left(\frac{1+\beta_1 E_{x'}+\beta_2\langle H^2\rangle_{x'}}{1+\beta_1 E_x+\beta_2\langle H^2\rangle_x}\right), \quad (2.45)$$

where $\langle H^2\rangle_x = \frac{\langle x|H^2|\Psi_v\rangle}{\langle x|\Psi_v\rangle}$. In order to perform p Lanczos steps exactly, we have to calculate $\langle x|H^n|\Psi_v\rangle$ for $n = 1, 2, ..., p$, which is more and more computationally expensive when p is increased. In this thesis, we performed one Lanczos step up to 324 sites, and two Lanczos steps up to 162 sites.

2.4.1 Variance Extrapolation

In the variational Monte Carlo, we can calculate the variance to get more information about the trial wave function:

$$\sigma^2 = \left[\frac{\langle\Psi_v|H^2|\Psi_v\rangle}{\langle\Psi_v|\Psi_v\rangle} - \left(\frac{\langle\Psi_v|H|\Psi_v\rangle}{\langle\Psi_v|\Psi_v\rangle}\right)^2\right], \quad (2.46)$$

which provides a criterion for how much $|\Psi_v\rangle$ deviates from an eigenstate. The variance σ^2 vanishes for all eigenstates of H, and a good variational wave function should give an energy close to E_0 and a small variance. In practice, we calculate the variance by

$$\frac{\langle\Psi_v|H^2|\Psi_v\rangle}{\langle\Psi_v|\Psi_v\rangle} = \frac{\sum_x\langle\Psi_v|H|x\rangle\langle x|H|\Psi_v\rangle}{\sum_x\langle\Psi_v|x\rangle\langle x|\Psi_v\rangle} = \frac{\sum_x E_x^2\Psi_v^2(x)}{\sum_x\Psi_v^2(x)}, \quad (2.47)$$

according to which we need to compute both the local energy and its square.

Whenever the variational wave function is sufficiently close to the exact ground state, it is possible to get information about the exact energy by performing a variance extrapolation. Indeed, we can write

$$|\Psi_v\rangle = |\Phi_0\rangle + \epsilon|\xi\rangle, \quad (2.48)$$

where $|\Phi_0\rangle$ is the exact ground state and $\langle\xi|\Phi_0\rangle = 0$. A straightforward calculation of E_v and σ^2 gives

$$E_v = E_0 + \epsilon^2\langle\xi|H|\xi\rangle/(1+\xi^2), \quad (2.49)$$

$$\sigma^2 \sim \epsilon^2\langle\xi|(H-E_0)^2|\xi\rangle/(1+\xi^2), \quad (2.50)$$

where ξ is small, we get

$$E_v \sim E_0 + const \times \sigma^2. \tag{2.51}$$

Based on the above relation, it is possible to use different wave functions, for example $p = 0, 1, 2$ Lanczos steps, to get different values of energy E_v and variance σ^2. Then we can perform the variance extrapolation to obtain the estimate of E_0, for $\sigma^2 = 0$.

2.4.2 Regularization

During the Markov chain process, the ratio $\frac{\langle x'|MF\rangle}{\langle x|MF\rangle}$ is required. By using a fast update for the ratio of two determinants [53], $\frac{\langle x'|MF\rangle}{\langle x|MF\rangle}$ can be evaluated in $O(1)$ op-

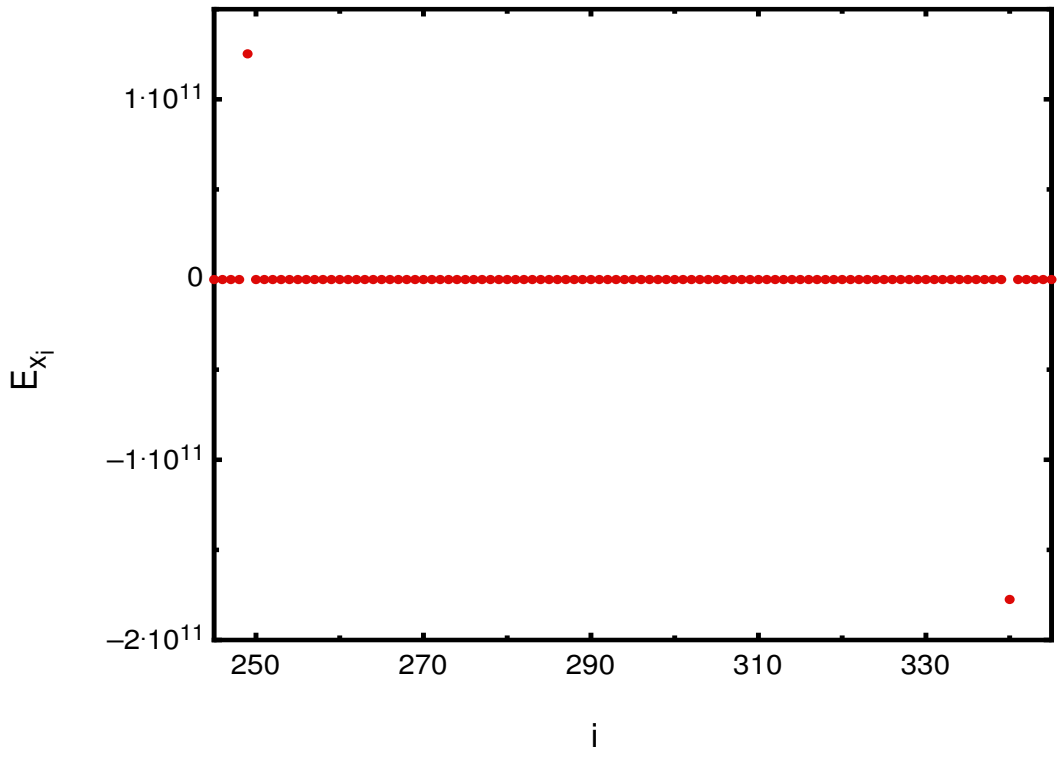

Figure 2.1: The local energy as function of the Monte Carlo steps without regularization. The $S = 1$ excitation at $J_2/J_1 = 0.5$ in the $J_1 - J_2$ Heisenberg model on the 6×6 lattice with $p = 1$.

erations within the $p = 0$ variational calculation, provided the denominator is finite. In this way, the core of the variational Monte Carlo algorithm is $O(N_{site}^2)$. There are some configurations $|x_0\rangle$ for which the wave function vanishes, i.e., $\langle x_0|\Psi_v\rangle = 0$. In the pure variational calculation, these configurations are not visited during the Markov chain, since they are always rejected by the Metropolis algorithm. However, whenever $p > 0$, most of these configurations will acquire a finite amplitude, namely

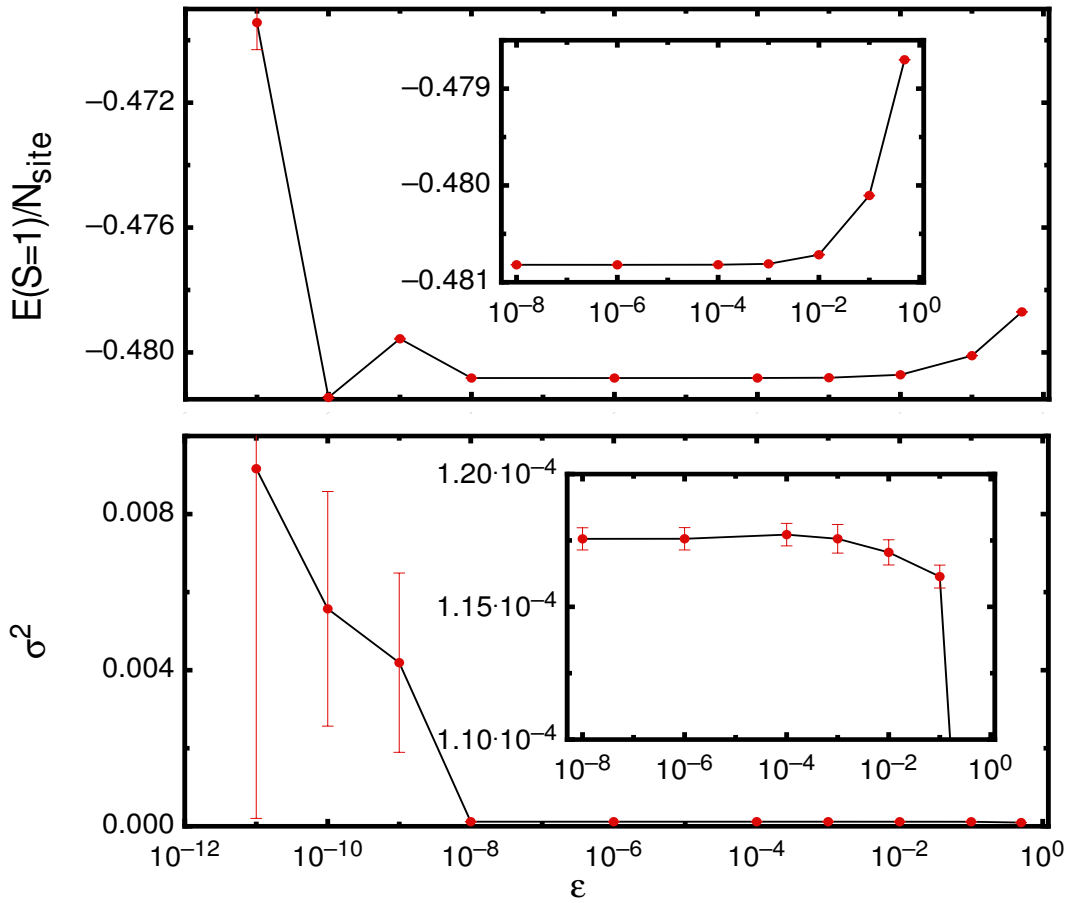

Figure 2.2: Test curves showing the importance of the regularization used for the $S = 1$ excitation with $p = 1$ at $J_2/J_1 = 0.5$ in the $J_1 - J_2$ Heisenberg model on the 6×6 lattice. ε is the value of the regularization used (see text). The insets are the amplification of the region $10^{-8} \leq \varepsilon \leq 10^0$.

$\langle x_0|\Psi_p\rangle \neq 0$. For example, for $p = 1$ we have

$$\langle x_0|\Psi_\beta\rangle = \langle x_0|\Psi_v\rangle + \beta\langle x_0|H|\Psi_v\rangle, \tag{2.52}$$

which can be non-zero when $\langle x_0|\Psi_v\rangle = 0$, because of $\langle x_0|H|\Psi_v\rangle$. The ratio between two wave functions calculated for different configurations $|x'\rangle$ and $|x\rangle$ is:

$$\frac{\langle x'|\Psi_\beta\rangle}{\langle x|\Psi_\beta\rangle} = \frac{\langle x'|\Psi_v\rangle + \beta\langle x'|H|\Psi_v\rangle}{\langle x|\Psi_v\rangle + \beta\langle x|H|\Psi_v\rangle}, \tag{2.53}$$

which, in principle would require $O(N_{site}^4)$ operations, because of $\langle x'|H|\Psi_v\rangle$ and $\langle x|H|\Psi_v\rangle$. Nevertheless, one could continue to use a fast update, by re-writing Eq.(2.53) like:

$$\frac{\langle x'|\Psi_\beta\rangle}{\langle x|\Psi_\beta\rangle} = \frac{\langle x'|\Psi_v\rangle}{\langle x|\Psi_v\rangle}\left(\frac{1+\beta E_{x'}}{1+\beta E_x}\right), \tag{2.54}$$

provided we do not visit configurations with a vanishing $p = 0$ wave function $\langle x_0|\Psi_v\rangle = 0$: the ratio $\frac{\langle x'|\Psi_v\rangle}{\langle x|\Psi_v\rangle}$ requires $O(1)$ operations, while the local energies are $O(N_{site})$. Since the fast update is $O(N_{site}^2)$, within this approach the $p = 1$ calculation does not increase the complexity of the algorithm. Moreover, it can be easily shown that a similar calculation leads to $O(N_{site}^2)$ operations for the ratio with $p = 2$.

Therefore, in order to have a fast code for $p = 1$ and 2, it is necessary to work in the subspace where $\langle x|MF\rangle \neq 0$. In practice, during the simulation we have to define a discernment to decide whether $\langle x|MF\rangle$ is vanishing or not (given the presence of roundoff in computers); here, we take the following criterion:

$$\sum_{x'\neq x}\left|\frac{\Psi_v(x')}{\Psi_v(x)}\right||H_{xx'}| < \frac{N_{site}}{\varepsilon}, \tag{2.55}$$

where ε is a small constant that can be optimized in order to have a stable simulation. The Markov chain is performed in the subspace where Eq.(2.55) is satisfied, and represents always a well-defined variational calculation, even though for $\varepsilon > 0$ some bias is introduced to the exact $\varepsilon \to 0$ limit.

In order to exemplify the advantage of this regularization, we report in Fig. 2.1 one calculation with $\varepsilon = 0$. Here, two large fluctuations are present, giving rise

to diverging errorbars. For these two points, the determinants acquire very small values, i.e., $|\Psi_v(x)| < 10^{-20}$. Remarkably, by using the regularization, those singular configurations are not present and a completely stable simulation is possible, see Fig. 2.2. Indeed, both the energy and the variance have a finite errorbar and do not depend upon the value of ε, ranging from 10^{-8} to 10^{-4}.

Up to here, we have described a simple way to perform a stable variational Monte Carlo simulation with $p > 0$, without visiting vanishing configurations. Whenever the number of these configurations is very large, the results obtained by this approach will be biased; in this case, even the variance extrapolation will fail to give

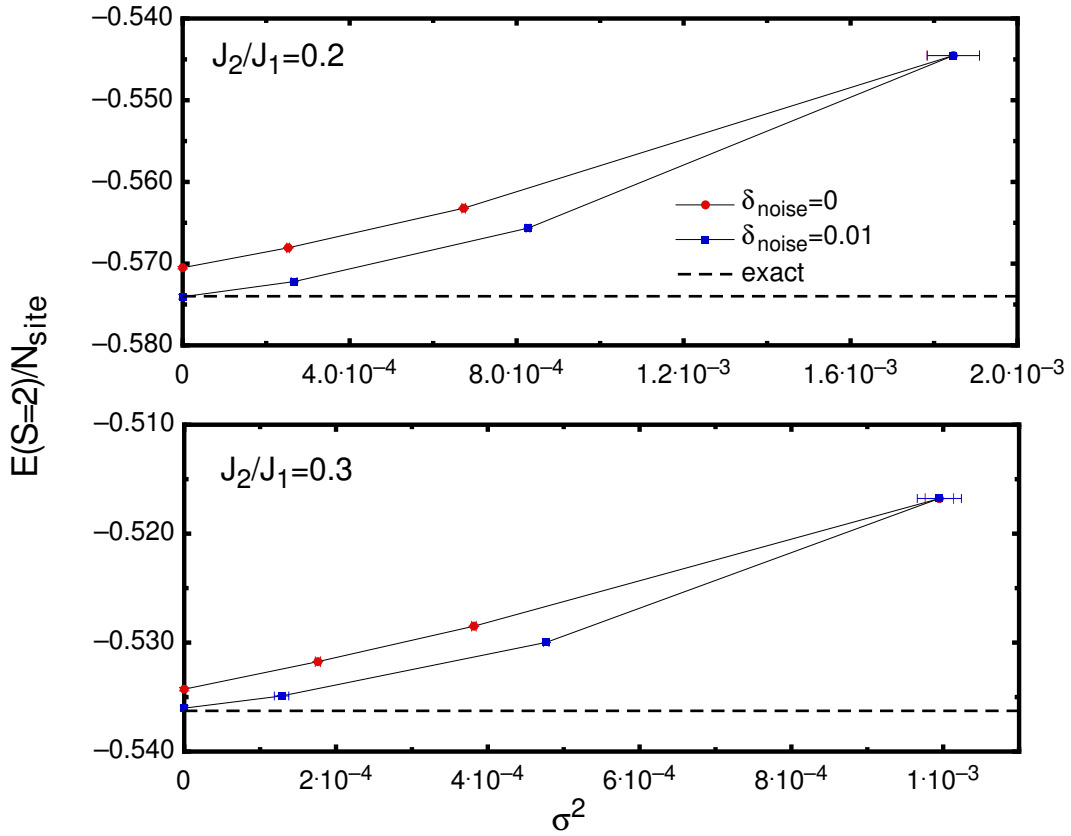

Figure 2.3: Test curves obtained by adding noise to the determinant for the $S = 2$ excitation with $p = 0, 1, 2$ at $J_2/J_1 = 0.2, 0.3$ in the $J_1 - J_2$ Heisenberg model on the 6×6 lattice. The extrapolated energy values are compared with the exact results.

the exact energy, since only a part of the total Hilbert space is spanned. In order to improve the calculations, we can slightly modify the original wave function in order to have $\langle x|MF\rangle \neq 0$ for all configurations $|x\rangle$. One possibility is to add a random on-site potential δ_{noise} in the mean-field Hamiltonian that defines $|MF\rangle$. By putting δ_{noise}, we can sample larger subspace to get better energy. In Fig. 2.3, we show the calculations of $S = 2$ excitation with and without noise in the small J_2/J_1 region of the $J_1 - J_2$ Heisenberg model on the 6×6 lattice. With $\delta_{noise} = 0$, the percentage of vanishing configurations is about 20%. For the pure variational calculation ($p = 0$), δ_{noise} does not change the value of the energy and the variance. By contrast, for $p = 1$ and 2, the gain in the accuracy is considerable, e.g., ($\sim 10^{-3}$) for energy. Also the variance extrapolations are sizable improved by the introduction of the random potential: with $\delta_{noise} = 0.01$ the quadratic fit gives the exact energy after extrapolation, while the estimated value is much higher when $\delta_{noise} = 0$.

2.5 Green's Function Monte Carlo

The Green's function Monte Carlo is a stochastic algorithm that allows us to perform the power method of Eq.(2.1):

$$\Psi_{n+1}(x') = \sum_x G_{x',x}\Psi_n(x), \tag{2.56}$$

where the subscript indicates the iteration "time" and the matrix $G_{x',x}$ is given by:

$$G_{x',x} = \langle x'|\Lambda - H|x\rangle = \Lambda\delta_{x',x} - H_{x',x}, \tag{2.57}$$

where Λ is a suitably large constant to project the initial trial state into the ground state of H.

First, we split $G_{x',x}$ into three parts:

$$G_{x',x} = s_{x',x}p_{x',x}b_x, \tag{2.58}$$

where $p_{x',x}$ is a stochastic matrix (i.e., $\sum_{x'} p_{x',x} = 1$ and $p_{x',x} \geq 0$), b_x is a weight (i.e., $b_x = \sum_{x'} |G_{x',x}|$), and $s_{x',x}$ is the sign of $G_{x',x}$. The idea of the Green's function Monte Carlo is to interpret Eq.(2.59) as a Master equation for a walker that walks

in the Hilbert space. Instead of performing the exact evolution $\sum_{x'} G_{x',x}\Psi_n(x)$, a walker described by the configuration $|x\rangle$ and its weight is considered (the latter one is due to b_x). Therefore, the Master equation is implemented by changing $|x\rangle$ into $|x'\rangle$ according to the transition probability $p_{x',x}$ and updating the weight ω into $\omega' = \omega b_x s_{x',x}$. Formally, we have that:

$$\langle x|\Psi_n\rangle = \int d\omega \omega P_n(x,\omega), \tag{2.59}$$

and

$$P_{n+1}(x',\omega') = \sum_x \int d\omega K(x',\omega'|x,\omega) P_n(x,\omega), \tag{2.60}$$

with the kernel $K(x',\omega'|x,\omega) = p_{x',x}\delta(\omega' - \omega b_x)$. By definition in Eq.(2.56), the state $\Psi_n(x)$ is

$$\Psi_n(x) = \langle \omega_n \delta_{x,x_n}\rangle = \int d\omega_n \omega_n P_n(x,\omega_n), \tag{2.61}$$

then the ground-state energy is given by

$$E_0 = \lim_{n\to\infty} \frac{\sum_{x_n} \int d\omega_n \omega_n E_{x_n} P_n(x_n,\omega_n)}{\sum_{x_n} \int d\omega_n \omega_n(x_n) P_n(x_n,\omega_n)} = \lim_{n\to\infty} \frac{\sum_{x_n} E_{x_n}\Psi_n(x_n)}{\sum_{x_n}\Psi_n(x_n)}, \tag{2.62}$$

where the local energy $E_{x_n} = \sum_{x'} H_{x',x} = \Lambda - b_x$.

The bare algorithm of Eq.(2.59) can be easily improved by considering the so-called importance sampling, namely by modifying the Green's function $G_{x',x}$ into:

$$\bar{G}_{x',x} = \Psi_G(x') G_{x',x}/\Psi_G(x), \tag{2.63}$$

where the wave function $\Psi_G(x)$ is a suitably chosen guiding function, which should be taken as close as possible to the exact ground state in order to minimize the statistical fluctuations. Notice that, in presence of the importance sampling, $\bar{G}_{x',x}$ is no longer symmetric. Therefore, a similar iterative technique can be implemented with:

$$\Psi_n(x)\Psi_G(x) = \langle \omega_n \delta_{x,x_n}\rangle. \tag{2.64}$$

Also the local energy should be modified by the guiding function,

$$E_{x_n} = \sum_{x'} \frac{\Psi_G(x')}{\Psi_G(x)} H_{x',x}. \tag{2.65}$$

The remarkable fact of this approach is to have the so-called zero-variance property, namely whenever the guiding function is the exact ground state $E_x = E_{gs}$, and the statistical fluctuations vanish. Since the convergence of the iterative procedure is exponentially fast, it is enough to stop the iteration to a reasonably finite $n = l$, then the corresponding estimate in Eq.(2.62) is

$$E_0 = \lim_{l\to\infty} \frac{\sum_n E_{x_n} G_n^l}{\sum_n G_n^l}, \tag{2.66}$$

where the weight factor G_n^l is given by

$$G_n^l = \prod_{j=1}^{l} b_{x_{n-j}} s_{x_{n-j+1},x_{n-j}}. \tag{2.67}$$

According to above definition, G_n^l is a product of l different factors, which can have very large fluctuations. To solve this problem, we introduce the many walkers algorithm [30], which allows us to drop out the irrelevant walkers with small weights and to control the bias due to the finite walkers.

Given M walkers, the corresponding configurations and weights are $([x], [\omega])$, with each component x_i and ω_i $(i = 1, ..., M)$. If the walkers are independent, we have that the probability distribution factorises

$$P_n([x], [\omega]) = \prod_i P_n(x_i, \omega_i). \tag{2.68}$$

Similarly to the one walker algorithm, the state evolved at the iteration n is

$$\Psi_n(x)\Psi_G(x) = \langle \frac{1}{M} \sum_{i=1}^{M} \omega_i \delta_{x,x_i} \rangle = \int [d\omega] \sum_{[x]} \frac{\sum_j \omega_j \delta_{x,x_j}}{M} P_n([x], [\omega]). \tag{2.69}$$

In order to avoid the divergence of the weights, we define a reconfiguration process that changes the probability distribution without changing the wave function

$$P'_n([x'], [\omega']) = \sum_{[x]} \int [d\omega] K([x'], [\omega']|[x], [\omega]) P_n([x], [\omega]), \tag{2.70}$$

with the kernel

$$K([x'],[\omega']|[x],[\omega]) = \prod_{j=1}^{M} \left(\frac{\sum_i \omega_i \delta_{x'_j,x_i}}{\sum_i \omega_i} \right) \delta \left(\omega'_j - \frac{\sum_i \omega_i}{M} \right). \tag{2.71}$$

This reconfiguration process generates a new set of M walkers $([x'],[\omega'])$ from the old ones, each new walker has the new configuration x'_i chosen with the probability $p_i = \frac{\omega_{j(i)}}{\sum_i \omega_i}$, and the weight $\omega' = \frac{1}{M}\sum_i \omega_i$. After this process, all walkers have the same weight, and the irrelevant walkers with small weights are dropped out. Moreover this kind of reconfiguration does not change the probability distribution [30].

Besides the energy, the Green's function Monte Carlo can be used to calculate also the correlation functions of the ground state. It is simple to compute the expectation values of operators which are diagonal in the working basis, $O_{x,x'} = \langle x|O|x'\rangle \delta_{x,x'}$. In order to get the expectation value $\langle O\rangle$, it is necessary to use the forward walking technique. The expectation value is written as

$$\langle O\rangle = \lim_{N,N'\to\infty} \frac{\langle \Psi_G|H^N O H^{N'}|\Psi\rangle}{\langle \Psi_G|H^{N+N'}|\Psi\rangle}. \tag{2.72}$$

In this equation, first one samples a configuration after N' GFMC steps, then computes $O_{x,x}$, and finally the walker is propagated forward for further N steps. In order to get this average, a similar approach for the energy can be used

$$\langle O\rangle = \lim_{l\to\infty} \frac{\sum_n O_{x_n} G^l_n}{\sum_n G^l_n}, \tag{2.73}$$

where O_{x_n} is the average over the walkers at the generation n, $O_{x_n} = \frac{1}{M}\sum_j O^n_j$, and O^n_j is the value on the configuration x_j of the j^{th} walker at the generation n. The factor G^l_n is

$$G^l_n = \prod_{j=-N}^{l-1} \omega'_{n-j}, \tag{2.74}$$

which is different from the case of the energy, and contains a further propagation of N steps.

In the forward walking technique, in order to control the bias, the set of values O^n_j with weights factors G^l_n has to be modified after each reconfiguration. In practice

after each reconfiguration, we have to bookkeep only the values O_j^n of the observable that survive after the reconfiguration. Therefore, after each reconfiguration, $O_i^{n'} = O_{j(i)}$, for $i = 1, ..., M$ and the function $j(i)$ describing the reconfiguration scheme has to be computed: the walker with index i assumes the configuration with index $j(i)$ before the reconfiguration. In order to implement recursively the forward walking, it is useful to store at each reconfiguration the integer function $j_n(i)$ for each reconfiguration n and the value O_i^n of of the operator for each walker. Then it is possible to compute the relevant configurations contributing to the operator O after N reconfiguration steps by recursive application of the integer function $j_n(i)$.

The Green's function Monte Carlo can be used to study the ground-state properties of a given Hamiltonian exactly in a numerical simulation, only if we do not have the so-called sign problem, i.e., the off-diagonal elements of matrix $G_{x',x} > 0$ ($x \neq x'$) (we can choose suitable value of Λ to have $G_{x,x} > 0$). When the sign of $G_{x',x}$, $s_{x',x}$, is not always larger than zero, the weights of walkers can be positive or negative, a wild cancelations will be between them, and then give a small quantity to sample with huge fluctuations. It is necessary to consider some kind of approximation, such as the fixed node approximation (FN) [19]:

$$H_{x',x}^{FN} = \begin{cases} H_{x',x}, & if\ H_{x',x} \leq 0, \\ 0, & if\ H_{x',x} > 0. \end{cases} \tag{2.75}$$

The FN defines H^{FN} starting from H, and sets to zero the positive off-diagonal elements. The fixed-node wave function Ψ^{FN} of H^{FN} can be computed without any sign problem, and it can be used to improve the variational wave function. Furthermore, the FN energy is an upper bound to the true ground state energy [19].

Chapter 3

Stripe in the 2D $t - J$ model

3.1 Introduction

The comprehension of the low-energy properties of strongly-correlated systems remains one of the biggest challenges in modern condensed matter physics. Indeed, although a fair good understanding has been achieved in some limiting cases (especially for large spatial dimensions, thanks to dynamical mean-field theory [13, 54]), many important questions remain widely open in the two-dimensional case, where the competition between charge/spin ordering and superconductivity is very strong. Unfortunately, in this case, there are not unbiased techniques that may be used to obtain accurate results for low temperatures and large system sizes. Therefore, several approximate methods have been developed and applied in the last years, for example variational (VMC) [55] and fixed-node (FN) Monte Carlo [19], density-matrix renormalization group (DMRG) [14] or its developments based upon the so-called tensor network states, including multi-scale entanglement renormalization ansatz (MERA) [56] and projected entangled-pair states (PEPS) [57], which has been recently generalized to fermionic systems [58] and infinite lattices (iPEPS) [59].

In the $t - J$ model, for the low electron density region, the results obtained by different analytical or numerical methods are consistent. For example, Hellberg *et al.* determined accurately the critical J/t for phase separation, i.e., $J_c/t \approx 3.43$ [60]. On the other hand, in the high electron density and small value of J/t (which is the related regime for cuprate high-temperature superconductors), different calculations

have shown contradicting outcomes. The variational analysis by Emery *et al.* leads to the conclusion that phase separation occurs for all values of J/t [35]. Hellberg *et al.* investigated this problem by the Green's function Monte Carlo method and Maxwell construction for larger clusters and reached similar conclusion [61]. The DMRG calculations show domain walls for doping $0 < \delta \leq 0.3$ [62], and a striped phase at $\delta = \frac{1}{8}$ [15]. By contrast, a critical value of J_c/t below which no phase separation exists, has been found both by high-temperature expansions [63] and power Lanczos techniques [64]: the former one obtained $J_c/t \sim 1$, the latter one $J_c/t \sim 0.6$. Moreover, by using variational and Green's function Monte Carlo, a critical value of $J_c/t \approx 0.7$ has been found [65]. More important issues on magnetic and superconducting properties are still under debate. One important issue, related to the mechanism of pairing in the cuprate materials, is whether some charge instability may take place (at $q = 0$, leading to phase separation, or at finite q, leading to the so-called stripes) or instead the homogeneous ground state is stable [66]. In the latter case, the residual attraction among quasi-particles may lead to a superconducting state. Previous FN calculations emphasized the existence of a stable superconducting ground state [67], while DMRG and iPEPS results suggested a stripe order [16].

The competition between superconductivity and stripes have been studied in several papers, and different aspects have been addressed in the recent past [68, 69, 70]. For example, it has been shown that a relatively small anisotropy in the super-exchange (and hopping) parameters may lead to a striped order [42]. In this regard, it is crucial to have a controlled method that may give variational results, in order to make a direct comparison of energies (and other correlation functions) among different methods and reach a final consensus.

In this chapter, we present state-of-the-art Monte Carlo calculations for the 2D $t-J$ model; first, we introduce the model and discuss the form of the wave functions that are used in the Monte Carlo methods, and then we show the variational results. The small size calculations show the accuracy of the methods. Then the phase diagram is obtained by the large-cluster calculations, and no phase separation is found for small J/t. We also consider stripe structures both in the variational wave function and Hamiltonian. These results suggest the absence of static stripes.

3.2 Model and methods

The $t-J$ model on the two-dimensional square lattice, which can be derived from the three-band Hubbard model[71], is defined by Eq.(1.3). This Hamiltonian is defined in the subspace without doubly occupied sites. In this chapter, we will take the amplitude for nearest-neighbor hopping $t = 1$, and consider, in most of the calculations, the antiferromagnetic super-exchange $J/t = 0.4$. The hole doping will be denoted by $\delta = 1 - N/N_{site}$, where N and N_{site} are the number of electrons and sites, respectively. In general the square lattice can be constructed by $N_{site} = l^2+m^2$, with l and m being positive integers. When l(or m)$= 0$ or $l = m$, the clusters have all symmetries of the infinite lattice; however, $l \neq m$ clusters have rotations, but no reflection symmetries. In this chapter, $L \times L$ or 45-degree tilted lattices (with $l = m$ and $N_{site} = 2l^2$, l being an odd integer, so that the non-interacting ground state is non-degenerate at half filling) are considered and periodic boundary conditions are taken in both directions.

Our starting variational wave function is constructed by applying different projector operators to a mean-field state

$$|\Psi_v\rangle = \mathcal{P}_N \mathcal{P}_G \mathcal{J}_d \mathcal{J}_s |\Phi_{MF}\rangle, \tag{3.1}$$

where $\mathcal{P}_N$ is the projector onto the subspace with N electrons, $\mathcal{P}_G$ is the Gutzwiller projector, which enforces no double occupation on each site. $\mathcal{J}_d$ is the density-density Jastrow

$$\mathcal{J}_d = \exp(\frac{1}{2}\sum_{i,j} u_{ij} n_i n_j), \tag{3.2}$$

with u_{ij} being the corresponding variational parameters, and $\mathcal{J}_s$ is the spin-spin Jastrow

$$\mathcal{J}_s = \exp(\frac{1}{2}\sum_{i,j} v_{ij} S_i^z S_j^z), \tag{3.3}$$

v_{ij} being the corresponding variational parameters. Finally, $|\Phi_{MF}\rangle$ is a mean-field state that may contain BCS pairing, antiferromagnetic order, or both. It can be taken as the ground state of the mean field Hamiltonian

$$H_{MF} = \sum_{i,j,\sigma} t_{ij} c_{i\sigma}^\dagger c_{j\sigma} + H.c. - \mu \sum_{i,\sigma} n_{i\sigma} + \sum_{\langle i,j\rangle} \Delta_{ij} (c_{i\uparrow}^\dagger c_{j\downarrow}^\dagger + c_{j\uparrow}^\dagger c_{i\downarrow}^\dagger + H.c.) + H_{AF}, \tag{3.4}$$

where Δ_{ij} is the BCS paring with $d-wave$ symmetry, and the staggered magnetic field term H_{AF} is

$$H_{AF} = \Delta_{AF} \sum_i (-1)^{R_i} (c^\dagger_{i\uparrow} c_{i\downarrow} + H.c.), \tag{3.5}$$

with the antiferromagnetic parameter Δ_{AF} in the $x-y$ plane. Relevant quantum fluctuations can be included by considering the Jastrow factor $\mathcal{J}_s$, which acts perpendicularly to the plane of the magnetization [20, 65].

The mean-field Hamiltonian (3.4) is quadratic in the fermionic operators and can be easily diagonalized in real space. Its ground state has the general form

$$|\Phi_{MF}\rangle = \exp\left(\frac{1}{2} \sum_{i,j,\sigma_i,\sigma_j} f_{ij}^{\sigma_i\sigma_j} c^\dagger_{i\sigma_i} c^\dagger_{j\sigma_j}\right) |0\rangle. \tag{3.6}$$

In general we can choose the configurations with definite z component of the spin. In the case of the standard BCS Hamiltonian with $\Delta_{AF} = 0$ or Δ_{AF} along z direction, the pairing function $f_{ij}^{\sigma_i\sigma_j}$ is an antisymmetric $2N_{site} \times 2N_{site}$ matrix, and the mean field wave function is equivalent to a slater determinant [55]. However, if the magnetic field is in the $x-y$ plane, the mean field wave function takes the form of a Pfaffian [20, 65],

$$\langle x|\Phi_{MF}\rangle = Pf[f]. \tag{3.7}$$

By using the minimization technique [72] described in Section 2.3, we are able to deal with a large number of variational parameters. In the wave function (3.1) the variational parameters are the u_{ij}'s and v_{ij}'s (for all independent distances in the lattice), and few parameters that describe the mean-field state $|\Phi_{MF}\rangle$ (i.e., the pairing amplitude Δ_{BCS}, the antiferromagnetic parameter Δ_{AF}, as well as the chemical potential μ and the next-nearest-neighbor hopping describing the variational electron dispersion). Due to the presence of strong correlations (i.e., the Gutzwiller projector and the Jastrow factors), a variational Monte Carlo approach is required to compute the energy and all physical observables.

The accuracy of the wave function (3.1) may be improved in different ways. The first one is by applying Lanczos steps as discussed in Section 2.4. Here, we consider the case in which few (i.e., $p = 1, 2$) Lanczos steps are applied to the original variational state (corresponding to $p = 0$). An estimation of the true ground-state

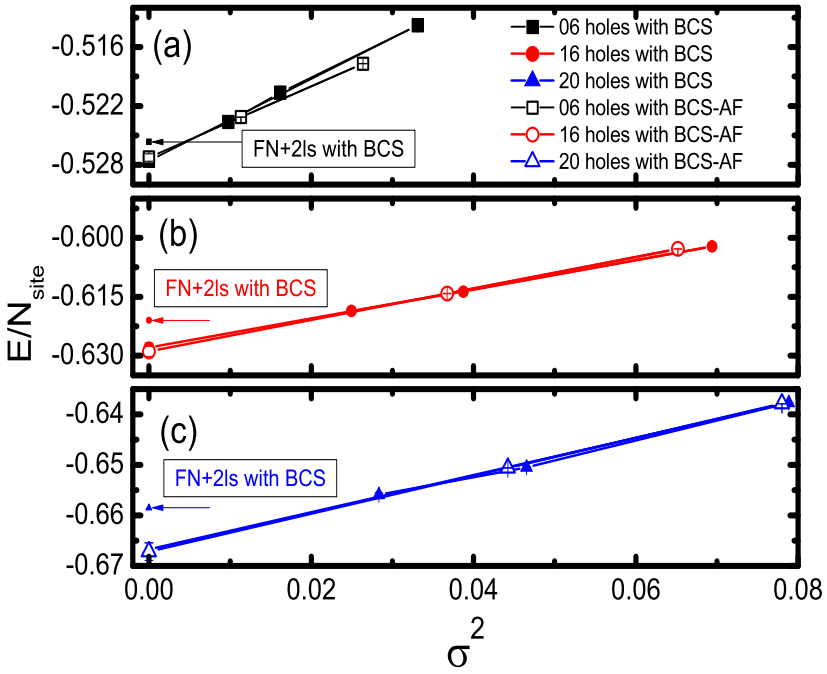

Figure 3.1: Variational results for the variance extrapolation on a 162-site cluster, for different numbers of holes: $p = 0$ and 1 ($p = 0, 1$ and 2) Lanczos steps have been performed on the wave function with (without) antiferromagnetism. The best fixed-node results are also marked by arrows.

energy may be achieved by the variance extrapolation (see Section 2.4). Therefore, the exact ground state energy $E_{\rm ex}$ may be assessed by fitting the variational ground-state energy E vs σ^2 for $p = 0, 1,$ and 2. Another way to improve the VMC calculations is through the FN approach [19], described in Section 2.5, where the ground state of an auxiliary FN Hamiltonian is obtained. In this case, we use the optimized variational wave function as the guiding function. Most importantly, the resulting energies are still variational, so to have a totally controlled approximation of the original problem [19].

3.3 Results

Before showing the results on large systems, we would like to mention that a very good accuracy on small lattices, where the Lanczos diagonalizations can be performed, is obtained. In Table 3.1 we compare our results with the exact ones on the 26-site lattice with 2 and 4 holes, and at different values of J/t. Pure VMC and FN results are shown, with 0, 1 and 2 Lanczos steps, as well as the estimated values from the variance extrapolation. We only consider BCS pairing and no antiferromagnetic order: in these cases, which correspond to relatively high dopings, the gain due to antiferromagnetism is negligible. Both the Lanczos steps and the FN techniques largely improve the variational wave function and the best FN calculations (with 2 Lanczos steps) reach an accuracy of $(E_{\rm ex} - E)/E_{\rm ex} \approx 0.002$ and ≈ 0.003 for 2 and 4 holes, respectively (for $J/t = 0.4$). The estimated energies, obtained by the variance extrapolation from the variational results with $p = 0, 1, 2$ Lanczos steps, agree with the exact data within one or two errorbars.

Let us now move to larger sizes, where we have used two kinds of wave functions, with and without antiferromagnetic parameters. We will define them by BCS+AF and BCS, respectively. In the following, for the Pfaffian wave function we will only consider $p = 1$, since $p = 2$ is very time consuming. Remarkably, the same extrapolated energies are obtained by using these two states, see Fig. 3.1, for 6, 16, and 20 holes. For the small values of dopings (i.e., 6 holes), the BCS+AF state gives better energies and smaller variances than the BCS results for $p = 0$ and 1. On the contrary, for large dopings (i.e., 16 and 20 holes), the presence of antiferromagnets is

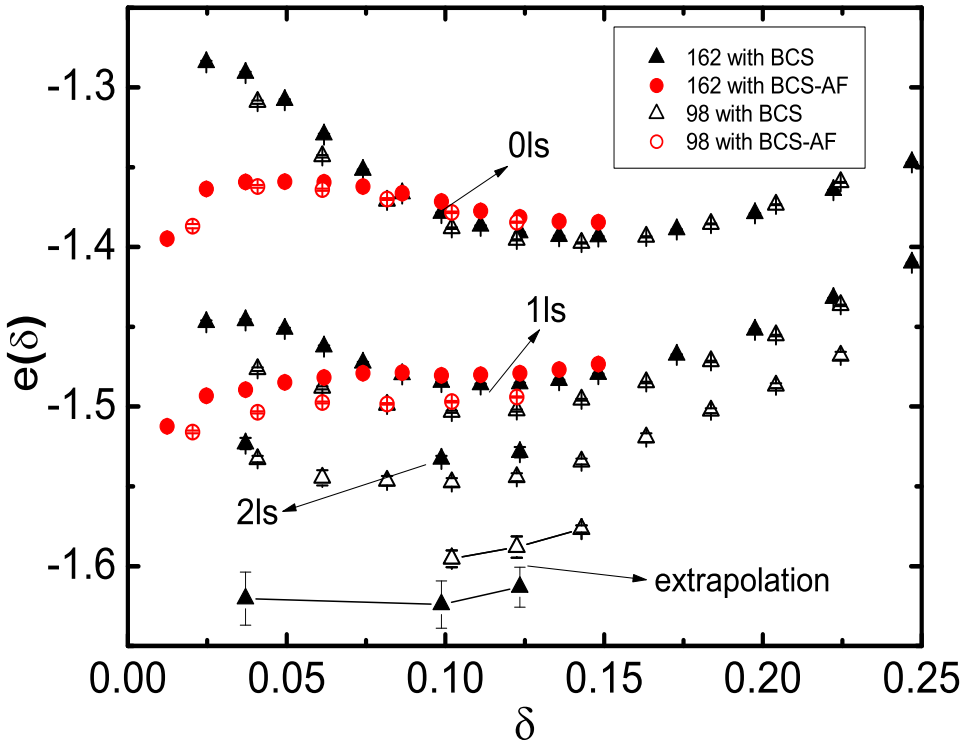

Figure 3.2: Energy per hole as a function of the doping for $J/t = 0.4$. Variational results are reported for $p = 0$ and 1 ($p = 0, 1$ and 2) Lanczos steps for the wave function with (without) antiferromagnetism. The extrapolated gap for $0.03 \lesssim \delta \lesssim 0.15$ are reported.

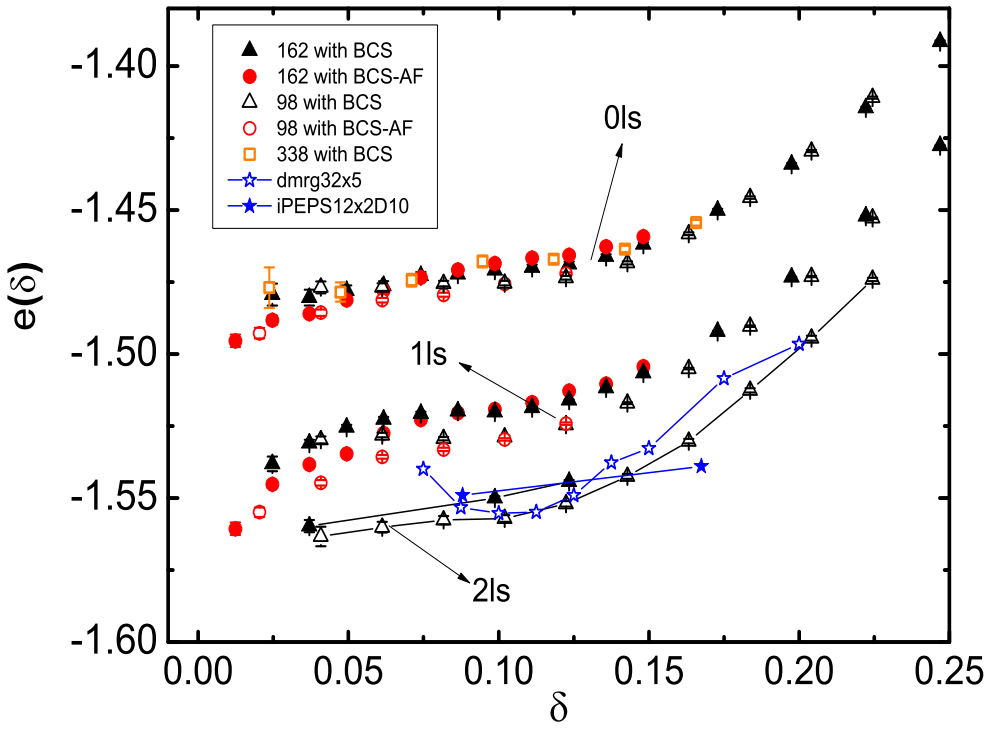

Figure 3.3: Energy per hole as a function of the doping for $J/t = 0.4$. Fixed-node results are reported for $p = 0$ and 1 ($p = 0, 1$ and 2) Lanczos steps for the wave function with (without) antiferromagnetism. The best variational DMRG and iPEPS energies [16] and the fixed-node with $p = 2$ are connected by dashed lines for a better comparison.

Table 3.1: VMC and FN energies per site for 26 sites with 2 and 4 holes. The estimated values of the variance extrapolation and exact results are also reported.

J/t	2 holes			
	VMC			extrapolation
	$p=0$	$p=1$	$p=2$	
0.3	-0.48334(1)	-0.49563(4)	-0.4985(1)	-0.5010(7)
0.4	-0.57664(1)	-0.58930(4)	-0.5925(1)	-0.5949(3)
0.5	-0.67045(1)	-0.68418(5)	-0.6874(1)	-0.6895(3)
0.6	-0.76463(1)	-0.77999(5)	-0.7833(1)	-0.7868(5)
0.8	-0.95410(1)	-0.97332(7)	-0.9771(1)	-0.9800(5)
1.0	-1.14483(1)	-1.16832(7)	-1.1727(1)	-1.1759(6)
	FN			exact
	$p=0$	$p=1$	$p=2$	
0.3	-0.49256(1)	-0.49824(1)	-0.49979(1)	-0.50097
0.4	-0.58625(1)	-0.59197(1)	-0.59349(1)	-0.59452
0.5	-0.68091(1)	-0.68700(1)	-0.68845(1)	-0.68945
0.6	-0.77645(1)	-0.78295(1)	-0.78446(1)	-0.78537
0.8	-0.96920(1)	-0.97684(1)	-0.97837(1)	-0.97935
1.0	-1.16385(1)	-1.17286(1)	-1.17434(2)	-1.17538
J/t	4 holes			
	VMC			extrapolation
	$p=0$	$p=1$	$p=2$	
0.3	-0.61372(1)	-0.63293(6)	-0.6375(1)	-0.6410(3)
0.4	-0.68894(1)	-0.70643(6)	-0.7107(1)	-0.7140(4)
0.5	-0.76461(1)	-0.78106(5)	-0.7851(1)	-0.7875(8)
0.6	-0.84065(1)	-0.85667(6)	-0.8606(1)	-0.8632(4)
0.8	-0.99361(1)	-1.01052(6)	-1.0144(1)	-1.0174(5)
1.0	-1.14760(1)	-1.16741(7)	-1.1719(2)	-1.1757(9)
	FN			exact
	$p=0$	$p=1$	$p=2$	
0.3	-0.62752(1)	-0.63677(1)	-0.63940(1)	-0.64262
0.4	-0.70101(1)	-0.70938(2)	-0.71207(1)	-0.71437
0.5	-0.77571(1)	-0.78399(1)	-0.78632(1)	-0.78812
0.6	-0.85132(1)	-0.85944(1)	-0.86164(1)	-0.86337
0.8	-1.00476(1)	-1.01338(1)	-1.01551(1)	-1.01733
1.0	-1.16072(1)	-1.17054(1)	-1.17306(1)	-1.17493

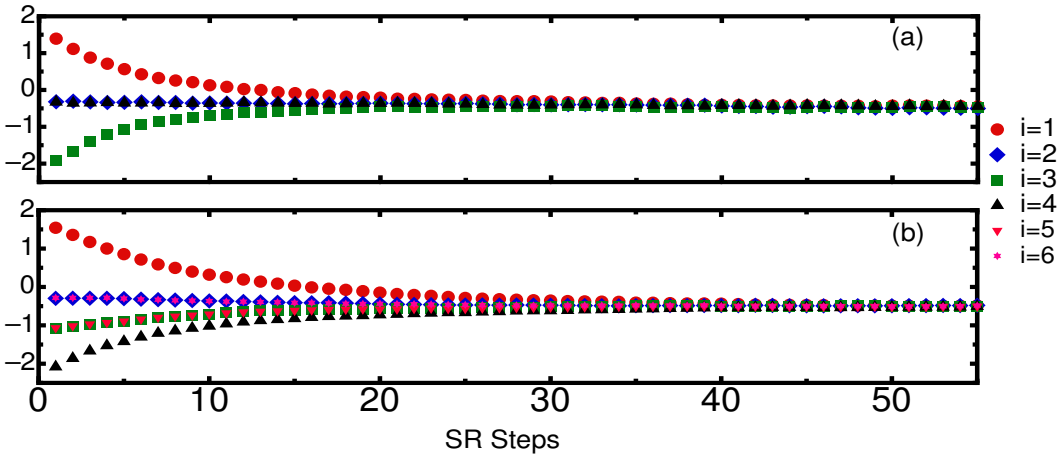

Figure 3.4: The CDW parameters as function of SR steps at 1/8 doping on 24×24 size cluster. (a) $l_s = 8$; (b) $l_s = 12$. i labels different sites.

not crucial to improve the variational state. The FN results with the second Lanczos step are also reported in Fig. 3.1, which are close to the extrapolated values and show very good accuracy.

In order to analyze the tendency towards phase separation, we calculate the energy per hole $e(\delta) = [E(\delta) - E(0)]/\delta$ at different dopings by using two kinds of wave functions. As mentioned in Chapter 1, $e(\delta)$ is a powerful detector for phase separation: a monotonic behavior of $e(\delta)$ vs δ indicates a finite compressibility and a stable uniform phase, while a minimum on finite systems or a flat behavior in the thermodynamic limit indicates an instability [35]. In Figs. 3.2 and 3.3, we show our results for various cluster sizes. It should be mentioned that the energy at half-filling has been computed for each cluster independently. We have seen that this choice minimizes finite size effects, which become negligible for $N_{site} \simeq 162$ sites. Close to half-filling, the Pfaffian wave function is considerably better than the simple superconducting state, indicating a coexistence of pairing and antiferromagnetic order [20, 65]. As the doping increases, the antiferromagnetic parameter decreases and eventually vanishes for $\delta \approx 0.1$. The general trend is clear: the increased accuracy of the calculation favors the homogeneous state, marked by a monotonic behavior of the energy per hole vs the doping. In particular, one Lanczos step strongly improves

the quality of the results, the gain in the FN energy being approximately $0.05t$, independently of δ. Even the second Lanczos step is efficient for these large sizes, providing a further energy gain of about $0.02t$. We also mention that the results obtained with the variance extrapolation are consistent with the DMRG and iPEPS ones [16]; indeed, we have that $e(\delta) = -1.61(1)$ for $0.03 \lesssim \delta \lesssim 0.12$. However, the extrapolated values have too large errorbars and cannot be used to study the issue of phase separation.

Although results with $p = 1$ and $p = 2$ are not size consistent, the largest size considered appears closely enough to describe the thermodynamic limit, and far from the system sizes where the Lanczos techniques may have problems (in principle for $N_{site} \to \infty$, $E_{p=2} \to E_{p=1} \to E_0$). Therefore, we have considered $p = 2$ FN calculations for $N_{site} = 162$ (or even 98 for $\delta \gtrsim 0.17$), which compare well with the best energies obtained by DMRG and iPEPS, see Fig. 3.3. The latter ones provide slightly more accurate energies for $\delta \simeq 0.1$. However, considering that all these methods are significantly away from the estimated exact energy per hole obtained by DMRG and variance extrapolations (i.e., $e(\delta) \simeq -1.61$), the difference between energies for $\delta = 0.1$ looks essentially irrelevant. In contrast with DMRG and iPEPS that find a minimum in the energy per hole [16], our best FN approximations do not show any tendency to phase separation for any doping, and, therefore, represent a thermodynamically stable phase corresponding to a well defined variational state.

Let us now consider the more subtle issue of stripes. Recently, DMRG and iPEPS calculations suggested that the ground state has charge (and spin) modulations, at least close to $\delta = 1/8$ [16]. Up to now, we have considered a uniform mean-field state $|\Phi_{MF}\rangle$, clearly biasing the variational results towards a homogeneous state. Despite the fact that the FN method can in principle remove this bias and give rise to non-uniform results, we have not found any evidence in favor of stripes with this variational ansatz.

In order to gain some evidence that a charge inhomogeneity is not stabilized in the low-doping regime, we add a site-dependent chemical potential in the mean-field Hamiltonian

$$\mu_{R_i} = \delta\mu \cos\left(\frac{4\pi}{l_s} x_i\right) + \mu_0, \tag{3.8}$$

where $R_i = (x_i, y_i)$ is the coordinate of the site i and l_s is equal to 8 or 12. In our

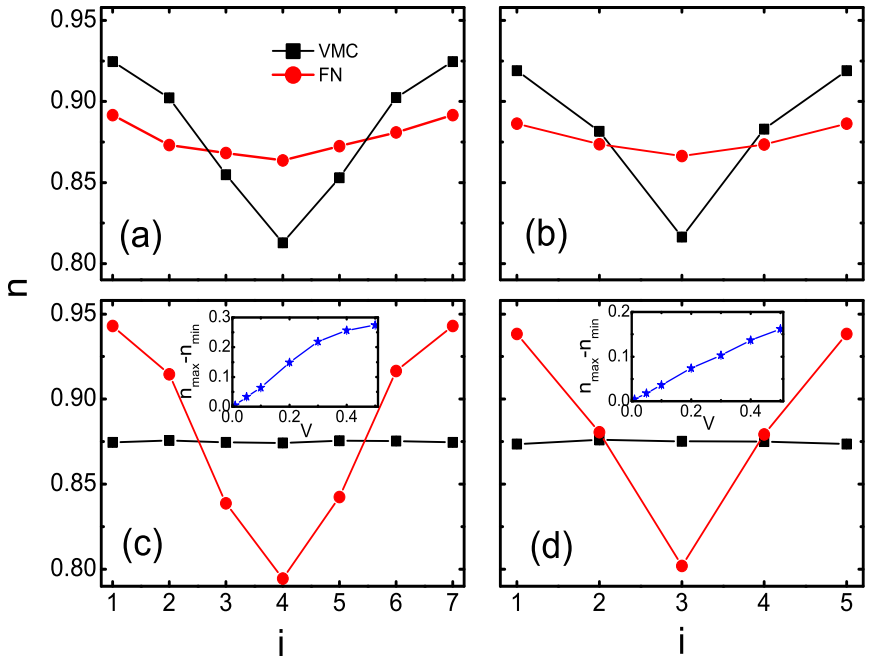

Figure 3.5: Upper panels: local density n_i when a site-dependent chemical potential with $\delta\mu = 1.6$ [see Eq. (3.8)] is added to the variational wave function; the cases with $l_s = 12$ (a) and 8 (b) are reported. Lower panels: local density n_i when a site-dependent potential [see Eq. (3.9)] is added to the $t-J$ Hamiltonian, with $l_s = 12$ and $V = 0.2$ (c) and $l_s = 8$ and $V = 0.4$ (d). Variational and fixed-node results are reported for a 12×12 cluster and $\delta = 1/8$. Insets: the difference between the largest and the smallest local density (at the fixed-node level) as a function of V.

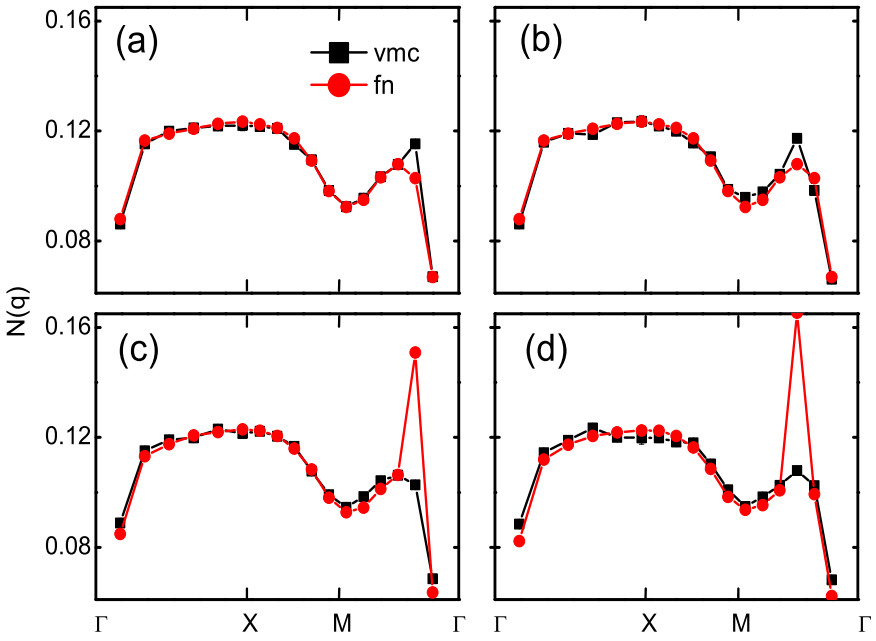

Figure 3.6: The density-density correlation function calculated by using the same parameters as Fig. 3.5. Upper panels: a site-dependent chemical potential with $\delta\mu = 1.6$ [see Eq. (3.8)] is added to the variational wave function; the cases with $l_s = 12$ (a) and 8 (b) are reported. Lower panels: a site-dependent potential [see Eq. (3.9)] is added to the $t-J$ Hamiltonian, with $l_s = 12$ and $V = 0.2$ (c) and $l_s = 8$ and $V = 0.4$ (d). Variational and fixed-node results are reported for a 12×12 cluster and $\delta = 1/8$.

simulations, we start from a given $\delta\mu$ and then release each μ_{R_i} in order to optimize each site in the unit cell independently. In Fig. 3.4, we show the evolution of the numerical optimization: after few iterations, a perfect uniform state is obtained, since all chemical potentials μ_{R_i} converge to the same value. Moreover, FN calculation strongly reduces the density modulation present in the original variational wave function, see Fig. 3.5. Although a small inhomogeneity remains in the density profile, the FN energy is always higher than the one with $\delta\mu = 0$. The density-density correlation function is reported in Fig. 3.6 with parameters corresponding to Fig. 3.5. In the upper panels, the VMC results show the peaks at $(\pi/3, 0)$ for $l_s = 12$ and $(\pi/2, 0)$ for $l_s = 8$; FN calculations reduce them to get the same $N(q)$ for both l_s. For these calculations, we consider 12×12, 16×16, and 24×24 lattices at $\delta = 1/8$. Similar results have been obtained also for $\delta = 1/12$ on a 12×12 lattice (not shown).

In order to show the effectiveness and the reliability of the FN method to detect charge inhomogeneities, we add a modulated potential directly in the $t-J$ Hamiltonian:

$$V_{R_i} = V \cos\left(\frac{4\pi}{l_s} x_i\right). \tag{3.9}$$

Then, we consider a uniform mean-field wave function and compute the local density for 12×12 and 24×24 lattices at $\delta = 1/8$. The results are also reported in Fig. 3.5. Clearly, the VMC results show a completely flat behavior of the density on different sites. On the contrary, the FN simulations are able to recover a strongly modulated density. The density-density correlation functions (see Fig. 3.6) show that the FN calculations obtain the peaks at $(\pi/3, 0)$ for $l_s = 12$ and $(\pi/2, 0)$ for $l_s = 8$ which we cannot find in the VMC results. This fact demonstrates that the presence of stripes could be detected by using this approach, even when a uniform guiding function is used in the FN technique.

Finally, we can also add a spin structure to the charge modulation, so to have:

$$n_{R_i} = 1 - \delta - \delta n \cos\left(\frac{4\pi}{l_s} x_i\right), \tag{3.10}$$

$$S^z_{R_i} = \delta s (-1)^{R_i} \sin\left(\frac{2\pi}{l_s} x_i\right). \tag{3.11}$$

The above structure implies a $2 \times l_s$ unit cell and contains the so-called π-shift,

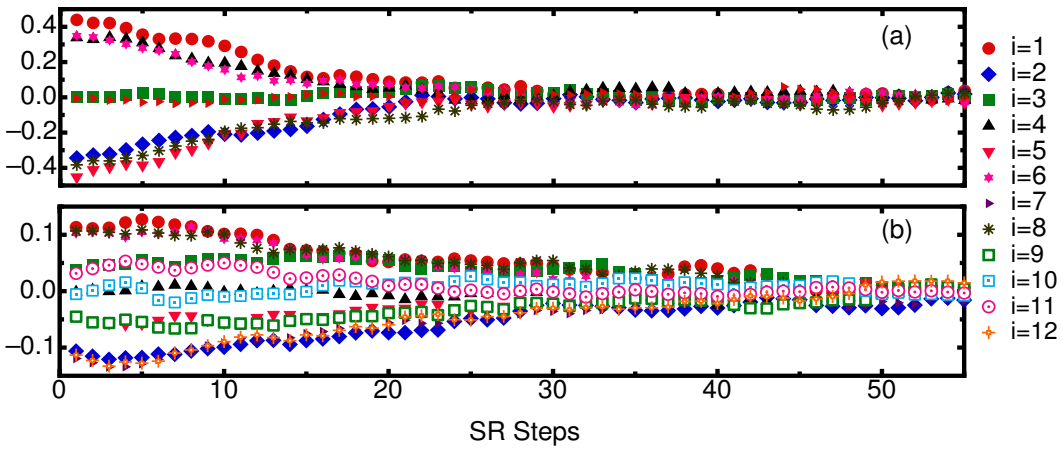

Figure 3.7: The SDW parameters as function of SR steps in the $2 \times l_s$ unit cell at 1/8 doping on 24×24 size cluster. (a) $l_s = 8$; (b) $l_s = 12$. i labels different sites.

namely anti-parallel spins across the hole-rich sites at $x_i = 0$ and $l_s/2$. In the following, we consider suitable variational parameters inside the mean-field Hamiltonian that defines the uncorrelated state (i.e., local chemical potentials and local magnetic fields) [68], such to reproduce a stripe with $l_s = 8, 12$ and take $\delta = 1/8$ on 16×16 and 24×24 lattices. We start from finite values of δn and δs and then optimize n_{R_i} and $S^z_{R_i}$ for each site independently. In Fig. 3.7, we observe that the initial stripe melts and a perfect uniform state is recovered. Moreover, the FN approach over the striped variational state leads to a much more uniform state, by replacing the $\pi-$shift with a small defect in a much weaker antiferromagnetic background, see Fig. 3.8.

3.4 Conclusions

In this chapter, we adopt the quantum Monte Carlo techniques described in Chapter 2: by applying few Lanczos steps to the variational wave function and by filtering out its high-energy components (by means of the Green's function Monte Carlo with the FN approximation), the accuracy of the calculations is highly improved. This approach is particularly effective at low doping and is actually unbiased at half filling.

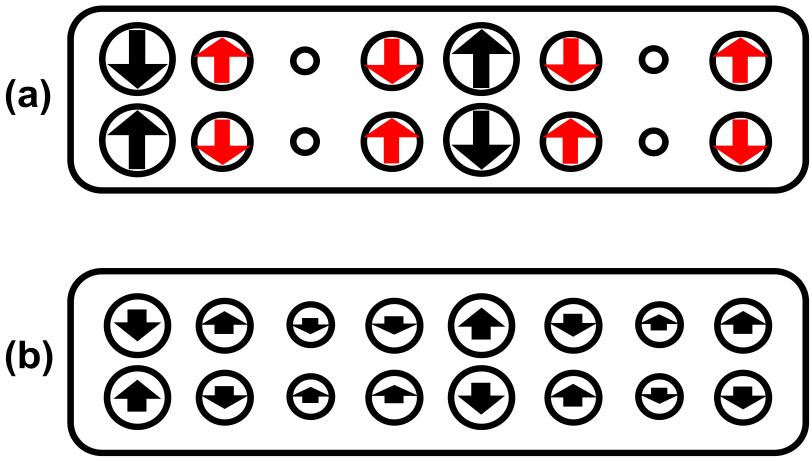

Figure 3.8: Variational (a) and fixed-node (b) charge and spin distributions in the 2×8 unit cell of a 16×16 lattice. The size of the circles and arrows is proportional to the electron density and spin along z, respectively (largest symbols: $n_{R_i} = 0.9195(4)$, $S^z_{R_i} = \pm 0.087(2)$).

Moreover, an estimation of the exact energy is given by the variance extrapolation. We have shown that the FN approach is particularly reliable, not only to improve the energy of a given variational ansatz, but also to determine the density profile of the ground state, in a way that is rather independent of the original ansatz. Indeed, the approximate FN ground state $|\Psi_{FN}\rangle$ is not a "brute force" variational ansatz, but it represents the ground state of a physical Hamiltonian that is different from the exact one only in the region where the variational wave function is close to zero (namely within the so-called *nodal region*). Operators $\mathcal{O}$ that are diagonal in configuration space $|x\rangle$ (e.g., related to stripes or antiferromagnetic order) are weakly affected by this nodal error. Indeed, in the expectation value of $\mathcal{O}$, which takes the form of $\sum_x \Psi^2_{FN}(x)\mathcal{O}_x$, the nodal region, where $\Psi_{FN}(x) \simeq 0$, provides a very little contribution, thus explaining the reliability of the FN approach in these cases.

Our results of energy per hole show that no phase separation is detected at any doping: at low doping, a uniform state is stabilized, containing both superconductivity and antiferromagnetism ($\delta < 0.1$). We also have studied the stripe phase by

adding charge and spin modulations into the mean-field ansatz. The optimization of wave function melts the stripes. On the other hand, if an external modulated potential is added to the $t-J$ Hamiltonian, the FN approximation gives rise to stripes, even when the initial state is chosen to be homogeneous.

Chapter 4

Quantum Spin Liquid

4.1 Introduction

During the "Valence-Bond-Solid era" most of the community working on highly-frustrated magnets believed that quantum spin liquids could not exist as true ground states of microscopic models and some kind of valence-bond order would have taken place in non-magnetic insulators (thus leading to trivial band insulators). Now, we are presently living in the more exciting "Quantum-Spin-Liquid era", where a plethora of different spin-liquid states are proposed as ground states of various magnetic systems, both theoretically and experimentally [24]. The turning point was marked by the discovery that stable gapped spin liquids may be found in effective low-energy Hamiltonians, which are based upon the so-called quantum dimer models [73] or strong-coupling expansions [74]. Since then, three main directions are carried out to study quantum spin liquids. The first one is the definition of *ad hoc* Hamiltonians that can be exactly solved to have a cartoon picture of the exotic properties expected in generic systems (e.g., topological degeneracy and fractional excitations) [75, 76]. The second one is the classification of different spin-liquid states according to hidden symmetries (i.e., beyond the Ginzburg-Landau description); examples may be given by the projective-symmetry group [50], tensor states [77], or cohomology [78, 79, 80]. Finally, the third and more pragmatic direction is to perform numerical simulations on frustrated models, in order to gain evidence that stable spin-liquid phases may indeed exist, such as the Heisenberg [17, 81, 82, 83, 84]

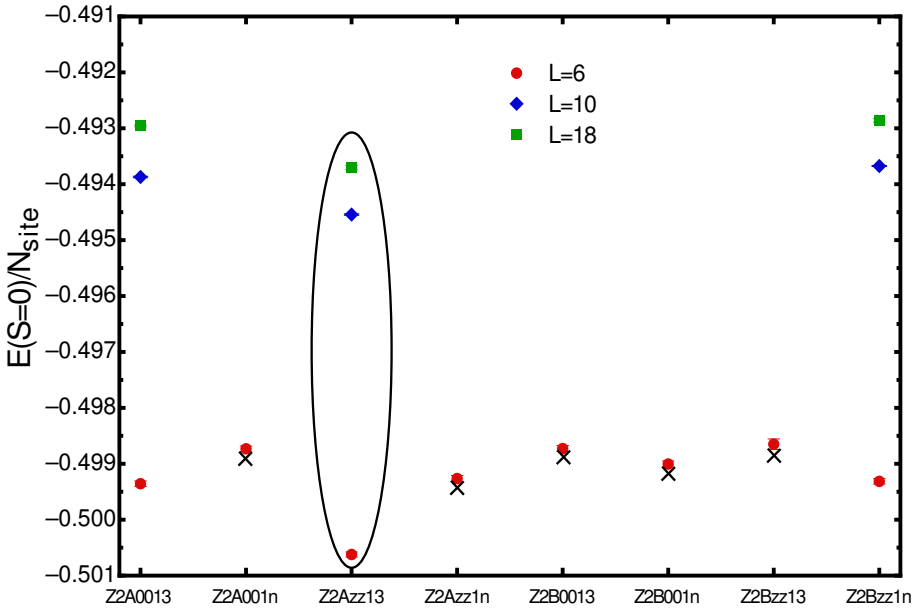

Figure 4.1: The ground state energy per site of eight Z_2 spin liquids in Ref. [50] (Z2A0013, Z2A001n,Z2Azz13, Z2Azz1n, Z2B0013, Z2B001n, Z2Bzz13, Z2Bzz1n) at $J_2/J_1 = 0.5$ on different sizes ($L = 6, 10, 18$). Black crossings mark unstable spin liquids, for which the variational parameters related to Z_2 symmetry vanish after the optimization of the wave function. The best energy is given by the ansatz Z2Azz13.

and Hubbard [85, 86] models on different kinds of lattice.

In this chapter, we take the third point of view and investigate the $J_1 - J_2$ spin-half Heisenberg model on the square lattice. As discussed in Chapter 1, the intermediate regime, separating two magnetically ordered phases (see Fig. 1.7), is the most debated one, since the combined effect of frustration and quantum fluctuations destroys antiferromagnetism and leads to a non-magnetic ground state. Recent density-matrix renormalization group (DMRG) results sparked the desire of understanding the phase diagram of the J_1-J_2 model, suggesting the existence of a true spin-liquid phase [17]. In particular, by considering cylindrical geometry, DMRG results for the singlet and triplet gaps provided some evidence for a fully gapped Z_2 state in the region $0.4 \lesssim J_2/J_1 \lesssim 0.6$, without local broken symmetry. Moreover, the calculation of the so-called topological entanglement entropy γ was

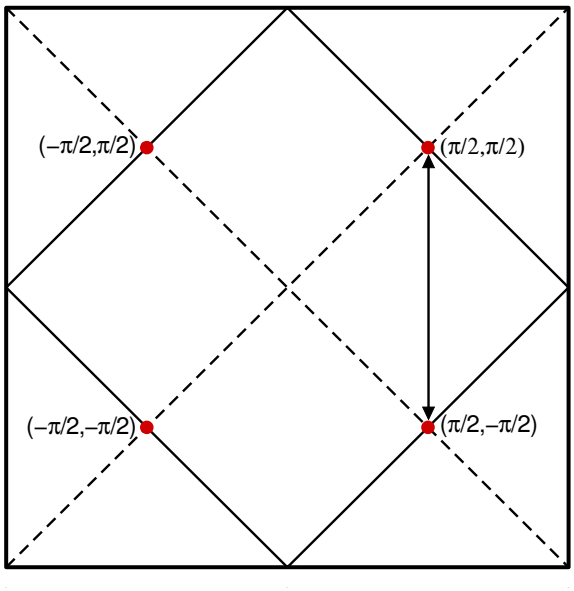

Figure 4.2: The mean field spectrum of the Hamiltonian Eq.(4.1). Four red points are the Dirac points.

found to be consistent with the expected value of $\gamma = \ln(2)$ for a gapped Z_2 spin liquid. The most natural description of a fully gapped state is given in terms of the Schwinger boson representation of the spin operators [87]. By performing a full optimization of the many-body wave function on small sizes (36 sizes), it has been shown that this kind of bosonic ansatz may qualitatively reproduce some of the DMRG results, and suggested a Z_2 gapped spin liquid with finite $S = 1$ spin gap [88]. However, while in the weakly-frustrated regime the bosonic ansatz has magnetic order and excellent variational energy, for $0.45 \lesssim J_2/J_1 \lesssim 0.6$ a state constructed with Abrikosov fermions instead of Schwinger boson has better accuracy [88]. In fact, in Ref. [81] the authors showed that, within this kind of fermionic representation, it is possible to have a particularly accurate description of the ground state in the strongly frustrated regime.

Here, we take the Abrikosov fermionic representation to construct our mean-field states and study various mean-field ansatze with different projective-symmetry groups (as described in Chapter 1). In particular, eight possible candidates for

describing the frustrated regime have been proposed [50]. After a full numerical optimization of these states (in presence of the Gutzwiller projector), we have found that the state dubbed Z2Azz13 (see Section 1.4.1) is stable and has a best variational energy in the strongly frustrated regime (see Fig. 4.1). This state has a Z_2 gauge structure (implying gapped gauge excitations) but gapless spinon excitations with four Dirac points. By using the ansatz Z2Azz13, we also construct the variational wave functions for low-lying excitations. The few Lanczos step technique will be used to systematically improve the accuracy of the variational states. A reliable estimate of the *exact* ground state, along with few relevant low-energy states, will be obtained. This procedure allows us to extract the spin gap and show that a gapless spin-liquid phase exists in the highly frustrated regime.

4.2 Model and Methods

The 2D Heisenberg J_1-J_2 model is defined by Eq.(1.6). Here, we focus on the case where both super-exchange couplings J_1 and J_2 are antiferromagnetic. We consider the square lattice $N_{site} = L \times L$ sites and periodic boundary conditions.

In order to construct the Z2Azz13 state, we take a gauge in which the mean-field Hamiltonian is real and defined by:

$$H_{MF} = \sum_{i,j,\sigma} t_{i,j} c^{\dagger}_{i,\sigma} c_{j,\sigma} + H.c. + \sum_{i,j} \eta_{i,j} (c^{\dagger}_{i,\uparrow} c^{\dagger}_{j,\downarrow} + c^{\dagger}_{j,\uparrow} c^{\dagger}_{i,\downarrow}) + H.c., \qquad (4.1)$$

where for each bond (i, j) there are hopping ($t_{i,j}$) and/or pairing ($\eta_{i,j}$) terms. Given any eigenstate $|\Psi_{MF}\rangle$ of the mean-field Hamiltonian, a physical state for the spin model can be obtained by a projection of it onto the subspace with one fermion per site:

$$|\Psi_v\rangle = \mathcal{P}_G |\Psi_{MF}\rangle. \qquad (4.2)$$

Here we will consider a projected state that is obtained by taking a real pairing η_{xy} (with d_{xy} symmetry) in the mean-field ansatz on top of the $U(1)$ state with nearest-neighbor hopping t and real pairing $\eta_{x^2-y^2}$ (with $d_{x^2-y^2}$ symmetry). A substantial energy gain is obtained by considering $\eta_{x^2-y^2}$ pairing for $(2, 1)$ (and symmetry related ones) and $(\pm 3, 0)$ and $(0, \pm 3)$ bonds (for $L > 6$), on top of the nearest-neighbor

bonds. The d_{xy} term is crucial to break the $U(1)$ gauge symmetry down to Z_2. Here, we consider η_{xy} terms for $(\pm 2, \pm 2)$ bonds, which imply *commensurate* Dirac points at $k = (\pm\pi/2, \pm\pi/2)$ in the mean-field spectrum, see Fig. 4.2. On the contrary, η_{xy} terms for $(\pm 1, \pm 1)$ bonds will give rise to *incommensurate* Dirac cones, whose positions depend upon the actual values of the variational parameters. Moreover, the former choice gives more stable simulations for $L > 6$. We want to stress the fact that both choices belong to the same Z2Azz13 ansatz. In order to minimize the variational energy, suitable boundary conditions have to be considered in the mean-field Hamiltonian.

The ground-state wave function is constructed by projecting the lowest-energy mean-field state. Furthermore, few excited states can be also constructed. For that, it is useful to consider a particle-hole transformation for the spin-down electrons on the mean-field Hamiltonian (4.1), i.e., $c^{\dagger}_{i,\downarrow} \rightarrow c_{i,\downarrow}$, while keeping the spin-up electrons unchanged, such that the transformed Hamiltonian conserves the total number of particles. Then, the ground state is obtained by filling the lowest N_{site} orbitals, with suitable boundary conditions (either periodic or anti-periodic) in order to have a unique mean-field ground state. Spin excitations can be obtained by creating the appropriate Bogoliubov quasi-particles (spinons) and possibly changing boundary conditions. Limited by states constructed from a single determinant, we consider a $S = 2$ state with momentum $k = (0, 0)$ by creating four spinons, and a $S = 1$ state with $k = (\pi, 0)$ or $(0, \pi)$ by creating two spinons with $k = (\pi/2, \pm\pi/2)$ or $(\pm\pi/2, \pi/2)$ (see Fig. 4.2). A brief discussion on the boundary conditions of the mean-field Hamiltonian is needed: when $L = 2 \times$ *odd integer*, the ground state has periodic boundary conditions in both directions, while excitations have antiperiodic conditions. The opposite is taken for $L = 2 \times$ *even integer*. By performing quantum Monte Carlo calculations, we are able to compute separately the energies of these three states, so as to assess the spin gaps of the $J_1 - J_2$ model.

In order to systematically improve the variational wave functions of the ground state and excitations, we apply a number p of Lanczos steps. Furthermore, if the starting wave function is sufficiently accurate, we can obtain an estimate of the exact energy $E_{\rm ex}$ with zero variance by fitting energy E_p vs variance σ_p^2 for $p = 0, 1, 2$ (see Section 2.4). The estimation of the gap is obtained by performing the variance extrapolation independently for the ground state and excitations.

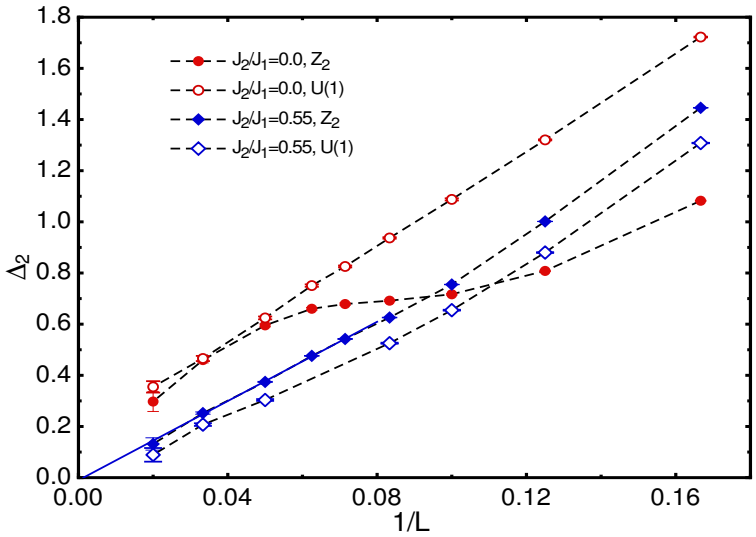

Figure 4.3: Calculations with fixed parameters of $S = 2$ spin gap Δ_2 by using different wave functions (Z_2 and $U(1)$ spin liquids) for $J_2/J_1 = 0$ and $J_2/J_1 = 0.55$ on square lattice until 50×50 cluster. The solid line is the linear fitting.

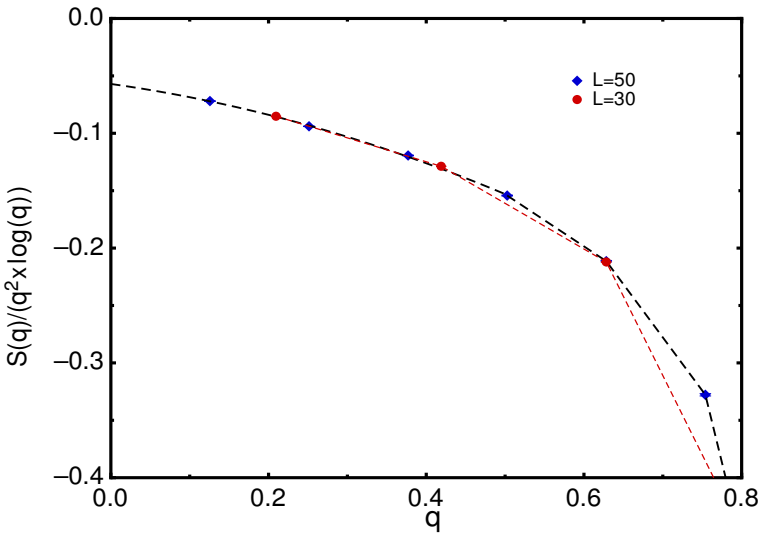

Figure 4.4: Calculations with fixed parameters of spin-spin correlation function $S(q)$ by using Z_2 spin liquid wave function at $J_2/J_1 = 0.55$ on 30×30 and 50×50 clusters.

4.3 Calculations with fixed parameters

Let us start by briefly considering the properties of the variational wave function. In order to do that, we fix the parameters ($\eta_{x^2-y^2}/t = 1$ at the nearest neighbors $(1,0)$ and $(0,1)$ and $\eta_{xy}/t = 0.5$ for $(\pm 2, \pm 2)$ bonds) and consider both the spin-spin structure factor

$$S(q) = \langle S^z_q S^z_{-q} \rangle = \frac{1}{N_{site}} \sum_{lm} e^{iq(R_l - R_m)} S^z_l S^z_m, \tag{4.3}$$

and the $S = 2$ spin gap (the same parameters are used for the $S = 0$ and $S = 2$ states). In Figs. 4.3 and 4.4, we report the numerical results. First of all, for small momenta, we have that

$$S(q) \sim q^2 \log(q), \tag{4.4}$$

which is the expected result in presence of Dirac points (to be contrasted with $S(q) \propto |q|$ in presence of a Fermi surface and $S(q) \propto q^2$ for gapped systems). We emphasize that the structure factor is a property of the wave function only and does not depend upon the excitation spectrum. The calculation of the gap instead requires the definition of an Hamiltonian. Indeed, in general, the connection between the behavior of correlation functions of the ground state and the properties of the low-energy excitations (that is always assumed) is a prerogative of local Hamiltonians, for which the *exact* ground-state properties mirror the low-energy spectrum. By directly computing the $S = 2$ gap Δ_2 of the variational wave function, we notice a very different behavior for $J_2 = 0$ and $J_2/J_1 = 0.55$. While for the latter case, we clearly see that Δ_2 is vanishing in the thermodynamic limit, for the former case, the situation is less clear and a finite gap cannot be excluded. We want to stress the fact that, while for the frustrated case the variational wave function represents a good ansatz for the exact ground state, so that a consistency between $S(q)$ and the gap is expected, for the unfrustrated case this wave function has a rather poor accuracy: in the language of the PSG, the spinon interactions can be so strong to destabilize the mean-field ansatz.

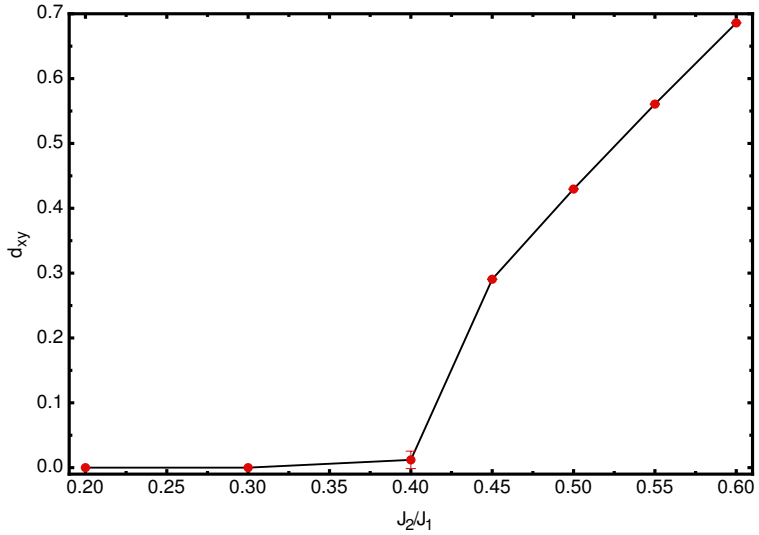

Figure 4.5: The d_{xy} pairing as function of J_2/J_1 on 6×6 lattice for the ground state. The value of d_{xy} is nonzero for $J_2/J_1 > 0.4$.

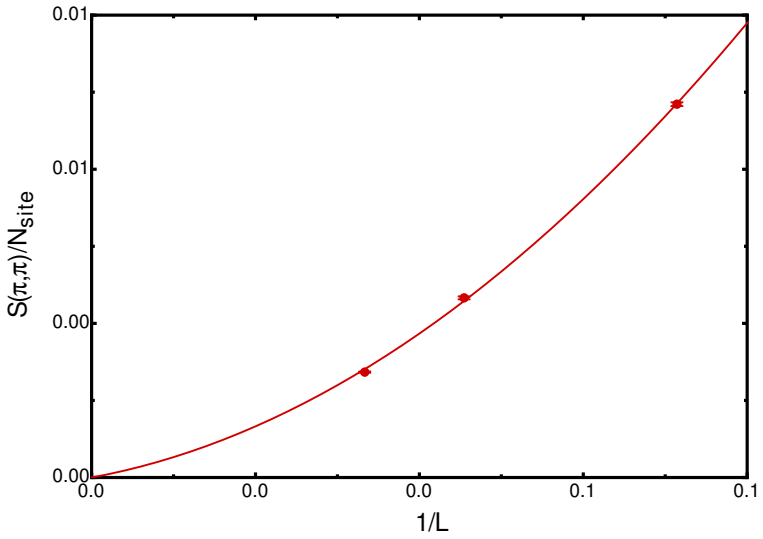

Figure 4.6: The spin-spin correlation function at momentum (π, π) divided by N_{site} at $J_2/J_1 = 0.5$ on different sizes $(L = 14, 22, 30)$ are reported. The quadratic fit is performed to show the non-magnetic order in the thermodynamical limit.

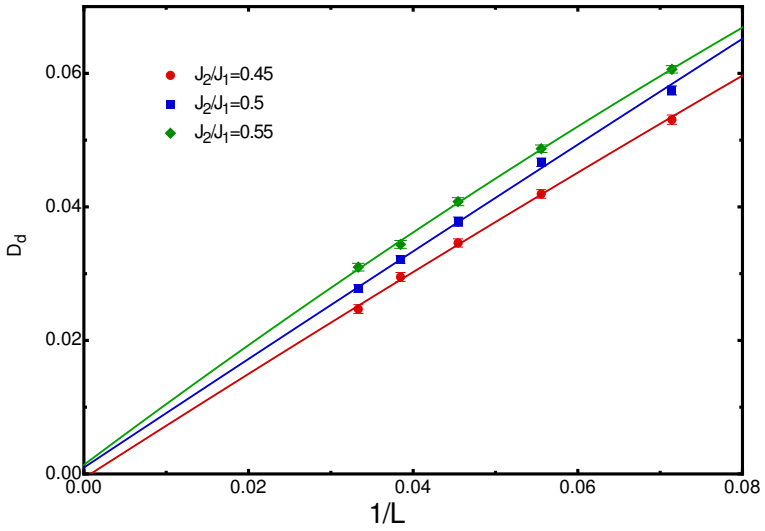

Figure 4.7: The dimer order parameter D_d as function of $1/L$ at $J_2/J_1 = 0.45$, 0.5 and 0.55 are reported. No dimer order is shown by the quadratic fit.

4.4 Main Results

In this section we present the main results for the $J_1 - J_2$ Heisenberg model on the square lattice. Therefore, we perform a numerical optimization of the variational wave function by using the technique described in Chapter 2. After optimization, the best possible ansatz for the variational wave function of the form (4.2) has a non-vanishing d_{xy} pairing, in the whole regime $0.45 \lesssim J_2/J_1 \lesssim 0.6$, which is important for having a Z_2 spin liquid, see Fig. 4.5. Most importantly, in this regime both the spin structure factor $S(q)$ at $q = (\pi, \pi)$ and the dimer-dimer correlations [89]:

$$D_d = 9 \lim_{r\to\infty} |D_{y,y}(r-y) + D_{y,y}(r+y) - 2D_{y,y}(r)|, \tag{4.5}$$

with

$$D_{\mu,\nu}(r-r') = \langle S^z_r S^z_{r+\mu} S^z_{r'} S^z_{r'+\nu}\rangle - \langle S^z_r S^z_{r+\mu}\rangle\langle S^z_{r'} S^z_{r'+\nu}\rangle, \tag{4.6}$$

do not show any evidence for the occurrence of ordered phases (see Figs. 4.6 and 4.7), in agreement with DMRG calculations [17].

In order to extract the information about the *exact* spin gap, a systematic improvement on the variational wave function is performed, which allows us to extract (i) the ground state energy, (ii) the energy of the lowest $S = 2$ state, and (iii) the energy of a state with $S = 1$ and $k = (\pi, 0)$ [or $(0, \pi)$]. The state with $S = 1$ and $k = (\pi, 0)$ is particularly interesting, since it is certainly gapped in the Néel phase and it is not expected to play any important role in a gapped non-magnetic regime (while it is one of the gapless modes in the collinear magnetic phase that appears for large J_2 values). On the contrary, this state is gapless in the Z2Azz13 ansatz. In the following, we will show that this $S = 1$ excitation becomes indeed gapless in a region around $J_2/J_1 = 0.5$, and, therefore, a spin liquid with gapless triplet excitations at $k = (\pi, 0)$, $(0, \pi)$, and (π, π) may represent a suitable candidate to describe the magnetically disordered state.

Before presenting the results of the spin gaps, in Fig. 4.8, we report calculations of energies of the ground state and the two excitations ($S = 1$ at $k = (\pi, 0)$ and $S = 2$ at $k = (0, 0)$) for different sizes of the cluster at $J_2/J_1 = 0.5$. For $L = 6$, where the exact results can be obtained by Lanczos diagonalizations, our extrapolations are extremely accurate. Moreover, for the ground state, our best variational $p = 2$ state gives the energy $E/J_1 = -0.503571(3)$, while $E_{\rm ex}/J_1 = -0.50381$; remarkably, the Lanczos step procedure remains effective even for larger sizes, the difference between the energy of the best variational state with $p = 2$ and the extrapolated one being very weakly size dependent (for $L = 10$, the $p = 2$ energy is $E/J_1 = -0.497549(2)$, while the extrapolated one is $E/J_1 = -0.49781(2)$). The same applies also for excited states (see Fig. 4.8). The almost perfect alignment of the Lanczos steps, together with the impressive accuracy obtained up to relatively large clusters, clearly indicates that the exact ground state should be essentially described by the starting Z_2 gapless state.

In Figs. 4.9 and 4.10, we show the results for the $S = 1$ spin gap Δ_1 at $k = (\pi, 0)$ and the $S = 2$ spin gap Δ_2 for the 6×6 cluster, in comparison with the exact results. Remarkably, our approach based upon a spin-liquid wave function gives excellent accuracy on Δ_1 in the whole region $0.2 \leq J_2/J_1 \leq 0.55$. A similar accuracy is also obtained for Δ_2 in the strongly frustrated region (i.e., $0.4 \leq J_2/J_1 \leq 0.55$), even though this is not a simple excitation since it involves four spinons. At $J_2/J_1 = 0.2$ and 0.3, with the help of the noise δ_{noise} in the mean-field determinant (see

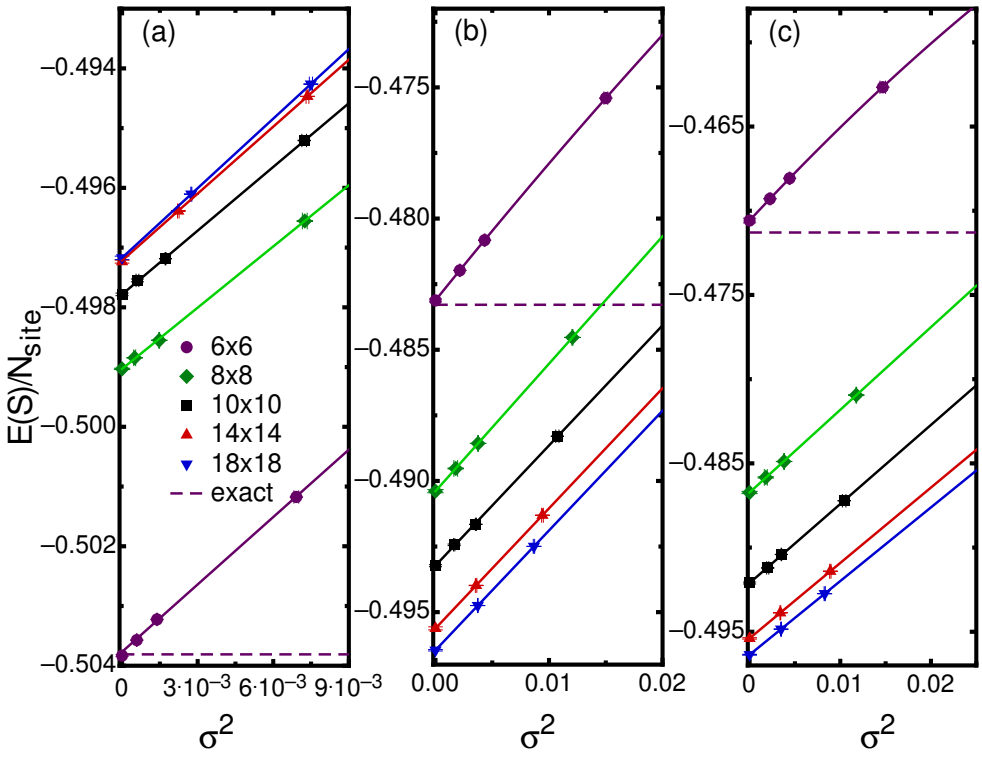

Figure 4.8: Energies per site for the $S = 0$ ground state (a), the $S = 1$ state with $k = (\pi, 0)$ (b), and the $S = 2$ with $k = (0, 0)$ (c) versus the variance for $J_2/J_1 = 0.5$. The results with $p = 0$, 1, and 2 are reported for $L = 4$, 6, 8, and 10, and with only $p = 0$ and $p = 1$ for $L = 14$ and $L = 18$. The variance extrapolated results are also shown.

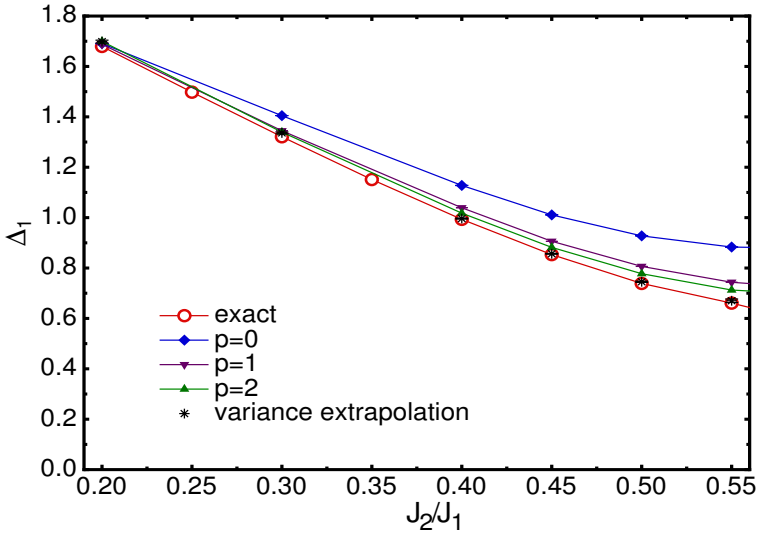

Figure 4.9: Spin gap for the $S = 1$ excitation at $k = (\pi, 0)$ for the 6×6 cluster. Results for $p = 0$, 1, and 2 Lanczos steps are reported, together with the extrapolated and the exact energies.

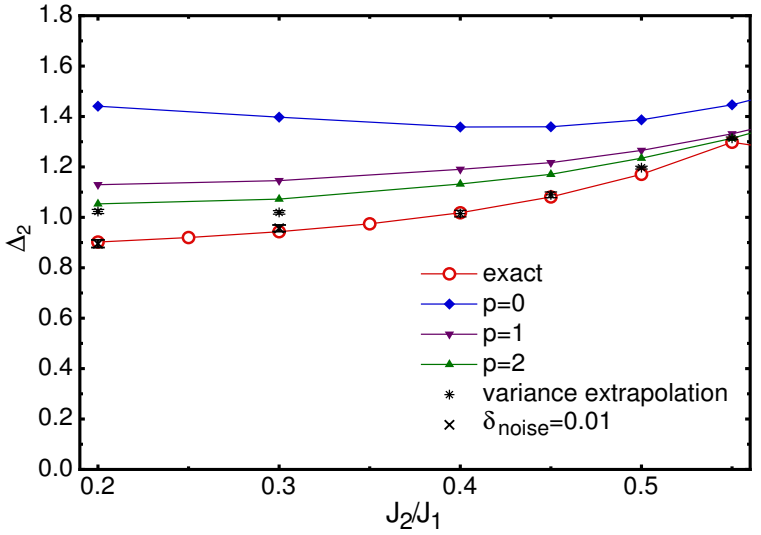

Figure 4.10: Spin gap for the $S = 2$ excitation with $k = (0, 0)$ for the 6×6 cluster. Results for $p = 0$, 1, and 2 Lanczos steps are reported, together with the extrapolated and the exact ones.

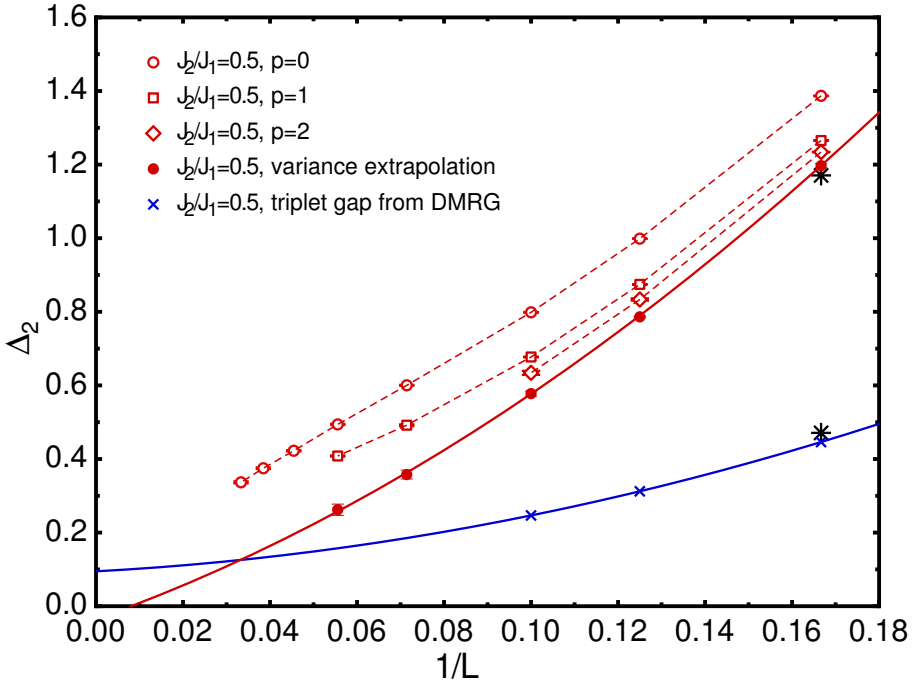

Figure 4.11: The $S = 2$ spin gap as a function of the system size for the variational wave function and the Lanczos extrapolation for $J_2/J_1 = 0.5$. The thermodynamic extrapolation is consistent with a vanishing gap within the errorbar, i.e., $\Delta_2 = -0.04(5)$. The DMRG results on $2L \times L$ cylinders (with open boundary conditions along x and periodic along y) for the $S = 1$ excitation are also shown [17]. Exact results (stars) of the $S = 2$ gap and the lowest $S = 1$ gap on the 6×6 cluster (with periodic boundary conditions) are reported.

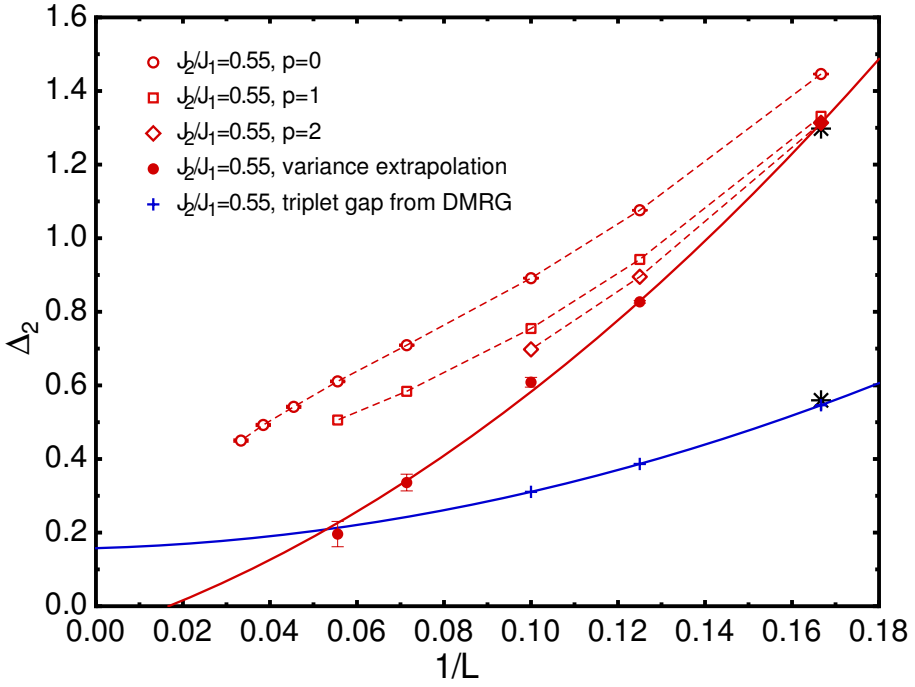

Figure 4.12: The $S = 2$ spin gap as a function of the system size for the variational wave function and the Lanczos extrapolation for $J_2/J_1 = 0.55$. The thermodynamic extrapolation is consistent with a vanishing gap within the errorbar, i.e., $\Delta_2 = -0.07(7)$. The DMRG results on $2L \times L$ cylinders (with open boundary conditions along x and periodic along y) for the $S = 1$ excitation are also shown [17]. Exact results (stars) of the $S = 2$ gap and the lowest $S = 1$ gap on the 6×6 cluster (with periodic boundary conditions) are reported.

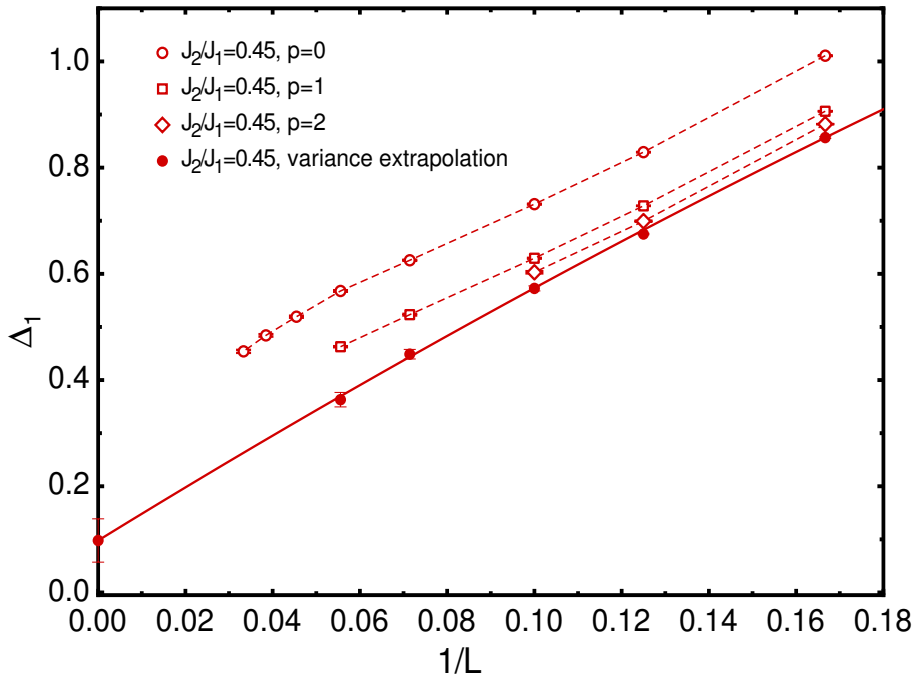

Figure 4.13: The $S = 1$ spin gap with $k = (\pi, 0)$ as a function of the system size for the variational wave function and the Lanczos extrapolation at $J_2/J_1 = 0.45$. The Lanczos step procedure reduces the gap on each size. The thermodynamic extrapolation shows a finite gap within the errorbar, i.e., $\Delta_1 = 0.10(4)$.

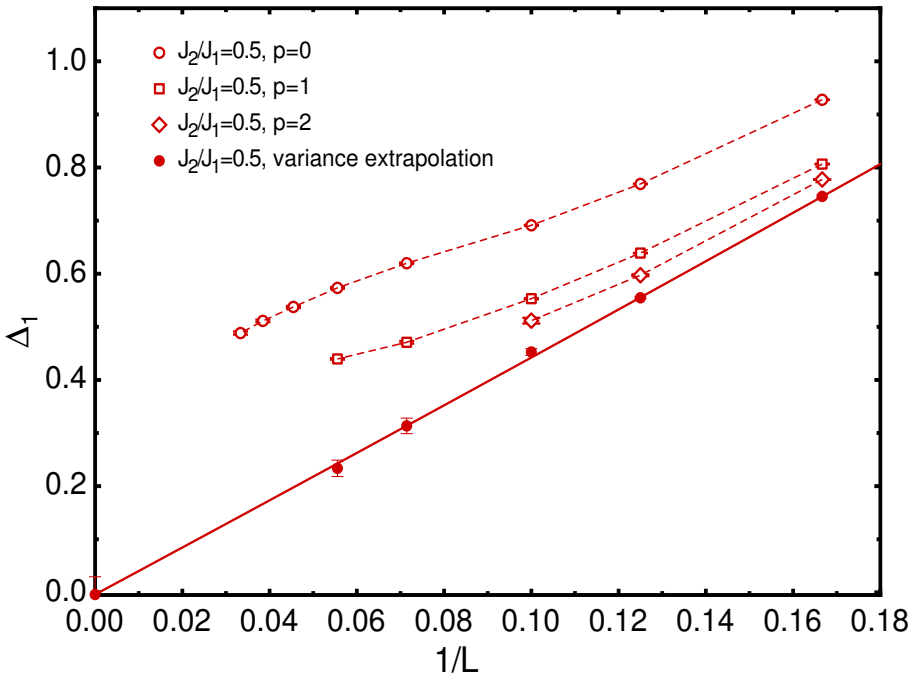

Figure 4.14: The $S = 1$ spin gap with $k = (\pi, 0)$ as a function of the system size for the variational wave function and the Lanczos extrapolation at $J_2/J_1 = 0.5$. The Lanczos step procedure reduces the gap on each size. The thermodynamic extrapolation is consistent with a vanishing gap within the errorbar, i.e., $\Delta_1 = -0.00(3)$.

Section 2.4), the $S = 2$ spin gap Δ_2 is consistent with the exact values. Instead, at $J_2/J_1 \simeq 0.6$ the accuracy deteriorates because a first-order transition to the collinear magnetic state takes place in the thermodynamic limit [17, 43, 91]: in this region, a quasi-degeneracy of levels in the energy spectrum occurs, leading to a reduced overlap between the variational wave function and the lowest exact eigenstate. [81, 90]

Then, we consider larger cluster and perform a finite size scaling of the gaps, see Figs. 4.11 and 4.12 for the $S = 2$, and Figs. 4.13 and 4.14 for $S = 1$ with $k = (\pi, 0)$, respectively. For $L \geq 6$, the extrapolations obtained with two ($p = 0$ and 1) or three ($p = 0$, 1, and 2) points are perfectly consistent (i.e., the three points lie along a straight line, see Fig. 4.8). Therefore, we perform the computationally demanding second Lanczos step only for relatively small clusters (up to $L = 10$), while we limit to the first Lanczos step for large clusters (up to $L = 18$).

The $S = 2$ gap is reported for two values of the frustrating ratio J_2/J_1, together with the $S = 1$ gap obtained by DMRG calculations of Ref. [17] in Figs. 4.11 and 4.12. We find that the Lanczos step procedure clearly reduces the gap on each size. In contrast with the DMRG picture, we have a clear evidence that the spin gap closes when $L \to \infty$ for $J_2/J_1 = 0.5$ and 0.55. Indeed, the values that we obtain in the thermodynamic limit are both compatible with a vanishing gap, i.e., $\Delta_2 = -0.04(5)$ and $-0.07(7)$ (see Figs. 4.11 and 4.12). We want to stress that our calculations are done on square clusters, having all the symmetries of the infinite lattice, and periodic boundary conditions, while DMRG calculations employed cylinders with $2L \times L$ sites and open boundary conditions along x. A possible explanation for having a finite gap within DMRG is that it favors low-entangled states with finite gaps. On the contrary, our variational approach is more flexible, allowing both gapped and gapless states. At the pure $p = 0$ variational level, the best wave function of the form (4.2) is found to be gapless, its energy being the lowest one among all states constructed from Schwinger bosons and Abrikosov fermions for $0.45 \lesssim J_2/J_1 \lesssim 0.6$ [88]; moreover, by applying few Lanczos steps, the finite-size gap lowers with no evidence for a finite value in the thermodynamic limit.

Finally, the $S = 1$ gap with $k = (\pi, 0)$ has been computed for various values of J_2 and cluster sizes (see Fig. 4.15). This gap is finite in the Néel phase for small J_2/J_1, where the only gapless $S = 1$ excitations have $k = (0, 0)$ and $k = (\pi, \pi)$.

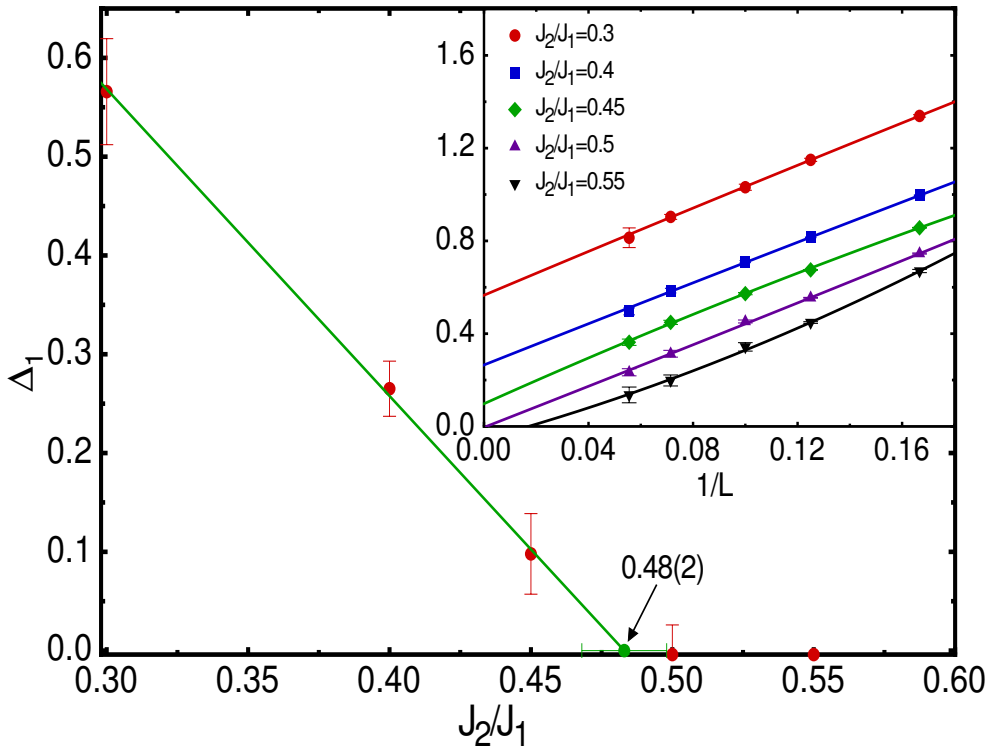

Figure 4.15: The behavior of the extrapolated gap as a function of J_2/J_1 is reported. The line is a guide to the eye. The Lanczos extrapolated gap as a function of L for different values of J_2/J_1 are also reported in the inset.

Indeed, this is what is found for $J_2/J_1 \lesssim 0.48$ when the Lanczos extrapolation is considered, even if the starting variational wave function is gapless before Gutzwiller projection. Remarkably, in agreement with the theoretical picture of the Z2Azz13 spin liquid, this gap vanishes for the two cases we investigated within the spin liquid region: $J_2/J_1 = 0.5$ and 0.55 (*before* the transition to the collinear magnetic phase, which occurs for $J_2/J_1 \gtrsim 0.6$). We expect that the $S = 1$ gap at $k = (\pi, 0)$ closes for $J_2 \to J_2^c$ with a non-trivial exponent smaller than one, whose value is however not possible to estimate with our numerical results. Nevertheless, by performing a linear fit of our data, we can obtain an upper bound of the critical J_2^c of the Néel phase to spin liquid transition, which can be located at $J_2^c = 0.48(2)$.

In the following we report detailed tables for all the energies of the ground state and excitations estimated with our methods, namely with the $p = 0$, 1, and 2 Lanczos step wave functions and variance extrapolation at different J_2/J_1 and cluster sizes.

Table 4.1: p=0

	$J_2/J_1 = 0.4$	$J_2/J_1 = 0.45$	$J_2/J_1 = 0.5$	$J_2/J_1 = 0.55$
$L = 6$ $S = 0$	$-0.52715(1)$	$-0.51364(1)$	$-0.50117(1)$	$-0.48992(1)$
$S = 1$	$-0.49582(1)$	$-0.48557(1)$	$-0.47541(1)$	$-0.46538(2)$
$S = 2$			$-0.46265(2)$	$-0.44974(2)$
$L = 8$ $S = 0$	$-0.52302(1)$	$-0.50930(1)$	$-0.49656(1)$	$-0.48487(1)$
$S = 1$	$-0.50835(1)$	$-0.49635(1)$	$-0.48453(1)$	$-0.47299(1)$
$S = 2$			$-0.48095(1)$	$-0.46806(1)$
$L = 10$ $S = 0$	$-0.52188(1)$	$-0.50811(1)$	$-0.49521(1)$	$-0.48335(1)$
$S = 1$	$-0.51362(1)$	$-0.50080(1)$	$-0.48830(1)$	$-0.47625(1)$
$S = 2$			$-0.48722(1)$	$-0.47443(1)$
$L = 14$ $S = 0$	$-0.52124(1)$	$-0.50745(1)$	$-0.49447(1)$	$-0.48242(1)$
$S = 1$	$-0.51772(1)$	$-0.50425(1)$	$-0.49131(1)$	$-0.47904(1)$
$S = 2$			$-0.49141(1)$	$-0.47880(1)$
$L = 18$ $S = 0$	$-0.52107(1)$	$-0.50728(1)$	$-0.49426(1)$	$-0.48215(1)$
$S = 1$	$-0.51921(1)$	$-0.50553(1)$	$-0.49249(1)$	$-0.48018(1)$
$S = 2$			$-0.49274(1)$	$-0.48026(1)$

Table 4.2: p=1

	$J_2/J_1 = 0.4$	$J_2/J_1 = 0.45$	$J_2/J_1 = 0.5$	$J_2/J_1 = 0.55$
$L = 6$ $S = 0$	$-0.52928(1)$	$-0.51538(1)$	$-0.50323(1)$	$-0.49303(1)$
$S = 1$	$-0.50042(1)$	$-0.49020(1)$	$-0.48082(1)$	$-0.47238(1)$
$S = 2$			$-0.46807(1)$	$-0.45605(1)$
$L = 8$ $S = 0$	$-0.52501(1)$	$-0.51101(1)$	$-0.49855(1)$	$-0.48777(1)$
$S = 1$	$-0.51157(1)$	$-0.49963(1)$	$-0.48857(1)$	$-0.47847(1)$
$S = 2$			$-0.48489(1)$	$-0.47305(1)$
$L = 10$ $S = 0$	$-0.52368(1)$	$-0.50973(1)$	$-0.49718(1)$	$-0.48622(1)$
$S = 1$	$-0.51610(1)$	$-0.50344(1)$	$-0.49165(1)$	$-0.48090(1)$
$S = 2$			$-0.49041(1)$	$-0.47867(1)$
$L = 14$ $S = 0$	$-0.52287(1)$	$-0.50899(1)$	$-0.49638(1)$	$-0.48519(1)$
$S = 1$	$-0.51966(1)$	$-0.50632(1)$	$-0.49398(1)$	$-0.48270(1)$
$S = 2$			$-0.49387(1)$	$-0.48221(1)$
$L = 18$ $S = 0$	$-0.52259(1)$	$-0.50874(1)$	$-0.49611(1)$	$-0.48475(1)$
$S = 1$	$-0.52083(5)$	$-0.50137(1)$	$-0.49475(1)$	$-0.48327(1)$
$S = 2$			$-0.49485(1)$	$-0.48319(1)$

Table 4.3: p=2

	$J_2/J_1 = 0.4$	$J_2/J_1 = 0.45$	$J_2/J_1 = 0.5$	$J_2/J_1 = 0.55$
$L = 6$ $S = 0$	$-0.52957(1)$	$-0.51558(1)$	$-0.50357(1)$	$-0.49399(1)$
$S = 1$	$-0.50130(1)$	$-0.49108(1)$	$-0.48197(1)$	$-0.47419(1)$
$S = 2$			$-0.46929(1)$	$-0.45750(1)$
$L = 8$ $S = 0$	$-0.52539(1)$	$-0.51125(1)$	$-0.49886(1)$	$-0.48841(2)$
$S = 1$	$-0.51224(2)$	$-0.50033(1)$	$-0.48952(1)$	$-0.48008(4)$
$S = 2$			$-0.48583(4)$	$-0.47443(2)$
$L = 10$ $S = 0$	$-0.5240(1)$	$-0.51001(1)$	$-0.49755(1)$	$-0.48693(3)$
$S = 1$	$-0.51671(7)$	$-0.50398(1)$	$-0.49243(1)$	$-0.4825(2)$
$S = 2$			$-0.49121(3)$	$-0.4800(2)$
$L = 14$ $S = 0$				
$S = 1$				
$S = 2$				
$L = 18$ $S = 0$				
$S = 1$				
$S = 2$				

Table 4.4: extrapolation

	$J_2/J_1 = 0.4$	$J_2/J_1 = 0.45$	$J_2/J_1 = 0.5$	$J_2/J_1 = 0.55$
$L = 6$ $S = 0$	$-0.52972(1)$	$-0.51566(1)$	$-0.50382(1)$	$-0.49521(7)$
$S = 1$	$-0.50204(5)$	$-0.49187(4)$	$-0.48312(6)$	$-0.4766(1)$
$S = 2$			$-0.4706(1)$	$-0.4587(1)$
$L = 8$ $S = 0$	$-0.52556(1)$	$-0.51140(1)$	$-0.49906(1)$	$-0.48894(3)$
$S = 1$	$-0.51282(1)$	$-0.50085(1)$	$-0.49039(2)$	$-0.48194(3)$
$S = 2$			$-0.48677(1)$	$-0.47602(3)$
$L = 10$ $S = 0$	$-0.52429(2)$	$-0.51017(2)$	$-0.49781(2)$	$-0.48766(6)$
$S = 1$	$-0.51718(3)$	$-0.50445(3)$	$-0.49329(5)$	$-0.4842(1)$
$S = 2$			$-0.49203(5)$	$-0.48157(8)$
$L = 14$ $S = 0$	$-0.52351(2)$	$-0.50953(1)$	$-0.49722(2)$	$-0.48696(5)$
$S = 1$	$-0.52052(2)$	$-0.50724(3)$	$-0.49562(5)$	$-0.48594(7)$
$S = 2$			$-0.49539(4)$	$-0.48524(9)$
$L = 18$ $S = 0$	$-0.52333(1)$	$-0.50940(1)$	$-0.49717(2)$	$-0.48698(5)$
$S = 1$	$-0.52180(4)$	$-0.50828(3)$	$-0.49645(3)$	$-0.48656(5)$
$S = 2$			$-0.49636(3)$	$-0.48638(5)$

4.5 Conclusions

In this chapter, by using the variational Monte Carlo techniques, we have studied the properties of the $J_1 - J_2$ Heisenberg model on the square lattice. The spin liquid Z2Azz13 has been used to construct the variational wave functions for not only the ground state ($S = 0$) but also the $S = 2$ and $S = 1$ with momentum $(0, 0)$ and $(\pi, 0)$ spin excitations, respectively. The results of the spin-spin and dimer-dimer correlations show no ordered phase in the strongly frustrated regime. In order to extract important information on the spin gap in the $J_1 - J_2$ Heisenberg model, the energy values of these three states have been computed.

The few Lanczos step technique has been performed to improve the accuracy of these three variational wave functions. With the help of $p = 1, 2$ Lanczos steps, the energy values of the ground state and excitations are highly improved. Though the variational calculations with Lanczos steps are not size consistent, we can do the variance extrapolation by the $p = 0, 1, 2$ variational results. On a small cluster like $L = 6$, the exact energies of the ground state and excitations are obtained by the linear extrapolation with the $p = 0, 1, 2$ calculations. On larger sizes, the calculations also show very high accuracy.

According to the systematic simulations on spin gaps until 324 clusters, we have showed that, at $J_2/J_1 = 0.5$ and 0.55, the $S = 2$ spin gaps go to zero when $L \to \infty$. The phase diagram can be obtained by the $S = 1$ spin gap which vanishes at $J_2/J_1 = 0.48(2)$. This is a solid evidence that the spin-liquid phase of the $J_1 - J_2$ model on the square lattice is gapless and may be very well described by using a Abrikosov-fermion mean field with a Z_2 gauge structure and gapless spinons with four Dirac points at $k = (\pm\pi/2, \pm\pi/2)$. The latter statement is further supported by the occurrence of a vanishing $S = 1$ gap at the non-trivial momenta $k = (\pi, 0)$ and $(0, \pi)$. Our calculations give the first direct evidence for the existence and the stability of highly-entangled gapless spin liquids in SU(2) spin models.

Conclusions

In this thesis, we have applied state-of-the-art quantum Monte Carlo techniques, including the variational and the Green's function Monte Carlo with the fixed-node approximation, to two-dimensional strongly-correlated systems. Few Lanczos steps have been used to systematically improve the accuracy of the trial wave functions. By introducing a suitable regularization scheme for the variational calculations with few Lanczos steps, stable and controllable simulations can be performed up to very large cluster sizes with good accuracy. We have studied two systems: the doped antiferromagnet described by the two-dimensional $t-J$ model and the frustrated Néel antiferromagnet described by the J_1-J_2 Heisenberg model on the square lattice.

For the $t-J$ model at $J/t = 0.4$, based on the previous variational [70] and fixed-node Monte Carlo [20] work, we have improved the accuracy of the uniform RVB state by few Lanczos steps and performed calculations up to the 162-site cluster. The final accuracy of the fixed-node Monte Carlo on top of few Lanczos steps is competitive with recent DMRG and iPEPS calculations [16], as far as the variational energy is concerned. Our main outcome is that the ground state is homogeneous and no evidence of stripes is detected around the doping $\delta = 1/8$. Indeed, our best approximation to the ground state does not show any evidence towards charge inhomogeneity. Furthermore, we confirm previous fixed-node calculations [20], where a uniform state containing superconductivity and antiferromagnetism is stabilized at low hole doping. By contrast, DMRG and iPEPS calculations suggested a stripe phase at doping $\delta = 1/8$ [15, 16]. Actually the conflict between the different methods is an open issue and deserves further investigations. In our work, we only considered charge and spin modulations Eqs.(3.10) and (3.11). It would be interesting to take into account other kinds of stripes, for example the π-phase domain RVB states

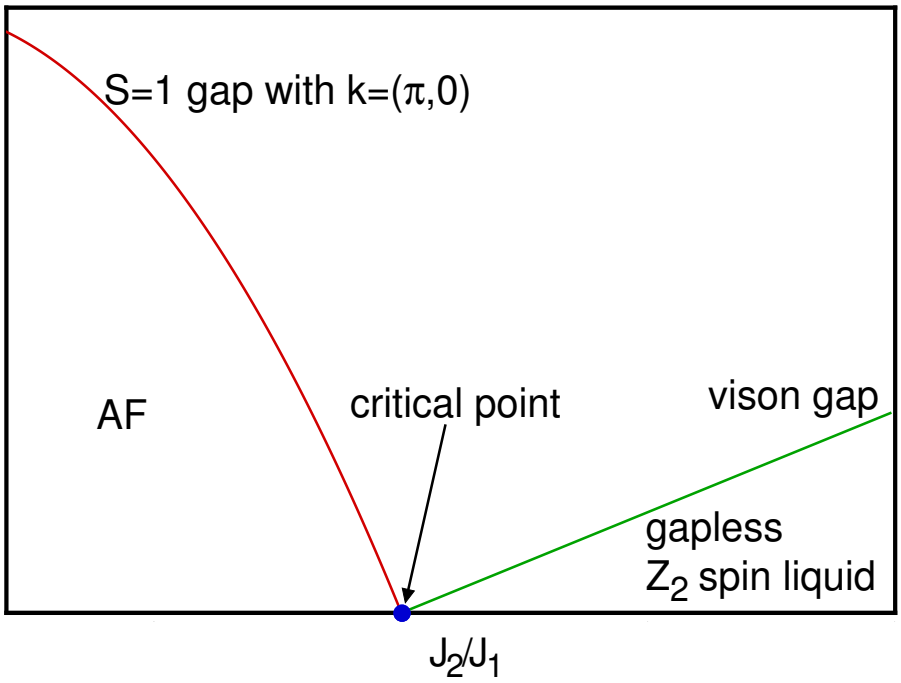

Figure 5.1: A continuous phase transition between antiferromagnetic order (AF) and the gapless Z_2 spin liquid. At the critical point, the vison gap (green line) and the $S = 1$ spin gap with $k = (\pi, 0)$ (red line) vanish. A state with four gapless modes with momenta $(0, 0)$, (π, π), $(\pi, 0)$, and $(0, \pi)$ is obtained not only in the spin-liquid regime but also at the critical point.

suggested in Ref. [69]. Another direction is to choose the so-called tensor network state as a variational wave function in quantum Monte Carlo simulations, because this new class of variational wave functions for two-dimensional systems is largely unbiased, as pointed out in Ref. [92]. This may help us to understand the reason for the present discrepancy between quantum Monte Carlo and DMRG/iPEPS and draw a final conclusion on the properties of the ground state in the two-dimensional $t - J$ model.

For the $J_1 - J_2$ Heisenberg model on the square lattice, according to the projective symmetry group classification [50] of different spin liquids (see Chapter 1), we searched among many possible candidates and obtained the best variational energy

at $J_2/J_1 = 0.5$ by means of the ansatz classified as Z2Azz13. No spin or dimer order has been found in the strongly frustrated regime and our calculations implied that a Z_2 spin liquid phase may faithfully represent the exact ground state around $J_2/J_1 = 0.5$. This is in agreement with the recent DMRG results [17], which also suggested a Z_2 spin liquid phase in the region $0.4 \lesssim J_2/J_1 \lesssim 0.6$. However, a finite triplet gap was obtained by DMRG in the spin-liquid phase. Instead, our results of the $S = 2$ and $S = 1$ spin gaps clearly support gapless excitations around $J_2/J_1 = 0.5$. In particular, we found gapless triplet excitations at momenta $(\pi, 0)$ and $(0, \pi)$, which are compatible with the presence of four Dirac points at momenta $(\pm\frac{\pi}{2}, \pm\frac{\pi}{2})$ in the mean-field part of the Z2Azz13 ansatz.

The disagreement between quantum Monte Carlo and DMRG may arise from the following reasons: in DMRG, calculations are done on $2L \times L$ clusters with cylindrical boundary condition, i.e., open boundary along x direction and periodic boundary along y direction. These boundary conditions may induce strong finite size effects, since the rotational symmetry of the lattice is broken. Moreover, the accuracy of the DMRG calculations exponentially decreases with the number of chains. Although further studies are necessary to completely clarify the nature of the ground state of the $J_1 - J_2$ model in the highly-frustrated regime, we believe that quantum Monte Carlo provides a reasonable and accurate description of the thermodynamic limit and suggests a very interesting effect from strong frustration, namely the vanishing of the $S = 1$ spin gap with $(\pi, 0)$ that may be observed in experiments.

We would like to remark that our results are not compatible with the standard Landau theory of continuous phase transitions. Here, a system described by a three-dimensional ($n = 3$) spin vector should have only $n - 1 = 2$ gapless modes, even at the transition point [93]. Instead, our results suggest the existence of four gapless triplets at the transition between the antiferromagnetic and the spin-liquid phases: the ordinary magnons with $k = (0, 0)$ and (π, π), but also two more excitations with $k = (\pi, 0)$ and $(0, \pi)$. Moreover, the spin-spin correlations of a gapless Z_2 spin liquid with Dirac points decay as $1/r^4$ because the correlation, namely the Gutzwiller projection, does not affect the long-range mean-field behavior. This implies that, if a Z_2 spin liquid remains stable down to the transition point, a critical exponent $\eta = 3$ of the spin correlations (decaying as $1/r^{1+\eta}$) is implied. This value is much

larger than the value $\eta \simeq 0.03$ obtained by the standard $n = 3$ continuous phase transition theory (i.e., based upon the ϕ^4 field theory) [94]. An alternative and rather interesting point of view is that the vison gap, which is finite in the Z_2 spin-liquid phase, vanishes when approaching the continuous transition to an antiferromagnetic phase. This implies that the mean-field state at the critical point should have a $U(1)$ gauge structure. In our parameterization of the Z2Azz13 ansatz, we should obtain the standard projected BCS wave function with $d_{x^2-y^2}$ symmetry and $d_{xy} \to 0$. This mean-field state is instead unstable against the Gutzwiller projection as for example a finite antiferromagetic order parameter appears for small J_2/J_1. For a continuous phase transition between an ordered antiferromagnet and a gapless Z_2 spin liquid, which becomes a critical $U(1)$ state at the transition, the exponent η can be therefore strongly modified by critical fluctuations. The scenario in which both the $S = 1$ excitations with $k = (\pi, 0)$ and $(0, \pi)$ and the vison gap vanish at the critical point is depicted in Fig. 5.1. The field theory describing this possibility is not known so far and, therefore, we believe that our numerical work requires further theoretical studies on this fascinating picture of the transition between an antiferromagnetic phase and a gapless Z_2 spin liquid.

Bibliography

[1] J.G. Bednorz and K.A. Müller, Z. Phys. **64**, 189 (1986).

[2] P.W. Anderson, Science **235**, 1196 (1987).

[3] J.M. Tranquada, B.J. Sternlieb, J.D. Axe, Y. Nakamura, and S. Uchida, Nature (London) **375**, 561 (1995)

[4] J.M. Tranquada, J.D. Axe, N. Ichikawa, Y. Nakamura, S. Uchidaand B. Nachumi, Phys. Rev. B **54**, 7489 (1996).

[5] J.M. Tranquada, J.D. Axe, N. Ichikawa, A.R. Moodenbaugh, Y. Nakamura, and S. Uchida, Phys. Rev. Lett. **78**, 338 (1997).

[6] V.J. Emery, S.A. Kivelson, and J.M. Tranquada, Proc. Natl. Acad. Sci. **96** 8814 (1999).

[7] Y. Shimizu, K. Miyagawa, K. Kanoda, M. Maesato, and G. Saito, Phys. Rev. Lett. **91**, 107001 (2003).

[8] S. Yamashita, Y. Nakazawa, M. Oguni, Y. Oshima, H. Nojiri, Y. Shimizu, K. Miyagawa, and K. Kanoda, Nature Physics **4**, 459 (2008).

[9] P. Mendels and F. Bert, J. Phys. Conf. Ser. 320, 012004 (2011).

[10] P.A. Lee, Science **321**, 1306 (2008).

[11] H. Bethe, Z. Phys. **71**, 205 (1931).

[12] E. H. Lieb and F. Y. Wu, Phys. Rev. Lett. **20**, 1445 (1968).

[13] A. Georges, G. Kotliar, W. Krauth, and M.J. Rozenberg, Rev. Mod. Phys. **68**, 13 (1996).

[14] S.R. White, Phys. Rev. Lett. **69**, 2863 (1992).

[15] S.R. White and D.J. Scalapino, Phys. Rev. Lett. **80**, 1272 (1998).

[16] P. Corboz, S.R. White, G. Vidal, and M. Troyer, Phys. Rev. B **84**, 041108(R) (2011).

[17] H.-C. Jiang, H. Yao, and L. Balents, Phys. Rev. B **86**, 024424 (2012).

[18] N. Trivedi and D.M. Ceperley, Phys. Rev. B **41**, 4552 (1990).

[19] D.F.B. ten Haaf, H.J.M. van Bemmel, J.M.J. van Leeuwen, W. van Saarloos, and D.M. Ceperley, Phys. Rev. B **51**, 13039 (1995).

[20] L. Spanu, M. Lugas, F. Becca, and S. Sorella, Phys. Rev. B **77**, 024510 (2008).

[21] *Solid State Physics*, N. W. Ashcroft and N.D. Mermin, Harcourt Inc. (1976).

[22] *Theory of Interacting Fermi Systems*, P. Nozieres, Westview Press. (1997).

[23] N. Mott and R. Peierls, Phys. Rev. B **64**, 024512 (1937).

[24] L. Balents, Nature **464**, 199 (2010).

[25] L. Pitaevskii and S. Stringari, J. Low Temp. Phys. **85**, 377 (1991); S. Stringari, arXiv:9311024.

[26] J. Hubbard, Proc. R. Soc. London, Ser. A **276**, 238 (1963); M.C. Gutzwiller, Phys. Rev. Lett. **10**, 159 (1963); J. Kanamori, Prog. Theor. Phys. **30**, 275 (1963).

[27] *Bosonization and Strongly Correlated Systems*, A.O. Gogolin, A.A. Nersesyan, A.M. Tsvelik, A.M. Tsvelik, and A.A. Nersesyan, Cambridge University Press. (2004).

[28] J.D. Reger and A.P. Young, Phys. Rev. B **37**, 5978 (1988).

[29] A.W. Sandvik, Phys. Rev. B **56**, 11678 (1997).

[30] M. Calandra Buonaura and S. Sorella, Phys. Rev. B **57**, 11446 (1998).

[31] *Lecture Notes on Electron Correlation and Magnetism* P. Fakezas, World Scientific, Series in Modern Condensed Matter Physics-Vol. 5 (1999).

[32] P.W. Anderson, Mater. Res. Bull. **8**, 153 (1973).

[33] S. Liang, B. Doucot, and P.W. Anderson, Phys. Rev. Lett. **61**, 365 (1988).

[34] *Introduction to Frustrated Magnetism: Materials, Experiments, Theory*, Springer Ser. Solid-State Sci. (2011).

[35] V.J. Emery, S.A. Kivelson, and H.Q. Lin, Phys. Rev. Lett. **64**, 475 (1990).

[36] J.D. Jorgensen, B. Dabrowski, Shiyou Pei, D.G. Hinks, L. Soderholm, B. Morosin, J.E. Schirber, E.L. Venturini, and D.S. Ginley, Phys. Rev. B **38**, 11337 (1988).

[37] P.C. Hammel, A.P. Reyes, Z. Fisk, M. Takigawa, J.D. Thompson, R.H. Heffner, S-W. Cheong, and J.E. Schirber , Phys. Rev. B **42**, 6781 (1990).

[38] P.C. Hammel, E.T. Ahrens, A.P. Reyes, R.H. Heffner, P.C. Canfield, S.-W. Cheong, Z. Fisk, and J.E. Schirber, Physica C **185-189**, 1095 (1991).

[39] F.C. Chou and D.C. Johnston , Phys. Rev. B **54**, 572 (1996).

[40] C. Castellani, C. Di Castro, and M. Grilli, Phys. Rev. Lett. **75**, 4650 (1995)

[41] S-W. Cheong, G. Aeppli, T.E. Mason, H. Mook, S.M. Hayden, P.C. Canfield, Z. Fisk, K.N. Clausen, and J.L. Martinez, Phys. Rev. Lett. **67**, 1791 (1991).

[42] F. Becca, L. Capriotti, and S. Sorella, Phys. Rev. Lett. **87**, 167005 (2001).

[43] P. Chandra and B. Doucot, Phys. Rev. B **38**, 9335 (1988).

[44] N. Read and S. Sachdev, Phys. Rev. Lett. **62**, 1694 (1989).

[45] M.P. Gelfand, R.R.P. Singh, and D.A. Huse, Phys. Rev. B **40**, 10801 (1989).

[46] F. Figueirido, A. Karlhede, S. Kivelson, S. Sondhi, M. Rocek, and D.S. Rokhsar, Phys. Rev. B **41**, 4619 (1990).

[47] P. Carretta, T. Ciabattoni, A. Cuccoli, E. Mognaschi, A. Rigamonti, V. Tognetti, and P. Verrucchi, Phys. Rev. Lett. **84**, 366(2000).

[48] P. Carretta, R. Melzi, N. Papinutto, and P. Millet , Phys. Rev. Lett. **88**, 047601 (2001); P. Carretta, N. Papinutto, C.B. Azzoni, M.C. Mozzati, E. Pavarini, S. Gonthier, and P. Millet, Phys. Rev. B **66**, 094420 (2002).

[49] G. Baskaran, Z. Zou, and P.W. Anderson, Solid State Commun. **63**, 973 (1987); G. Baskaran and P.W. Anderson, Phys. Rev. B **37**, 580 (1988).

[50] X.-G. Wen, Phys. Rev. B **65**, 165113 (2002).

[51] X.-G. Wen, Phys. Rev. B **44**, 5708 (1991).

[52] N. Metropolis, A.W. Rosenbluth, M.N. Rosenbluth, A.H. Teller, and E. Teller, J. Chem. Phys. **21** 1087 (1953).

[53] *Variational description of Mott insulators*, PhD thesis, M. Capello (2006).

[54] T. Maier, M. Jarrell, T. Pruschke, and M.H. Hettler, Rev. Mod. Phys. **77**, 1027 (2005).

[55] C. Gros, Phys. Rev. B **38**, 931 (1988); Phys. Rev. B **42**, 6835 (1990).

[56] G. Vidal, Phys. Rev. Lett. **99**, 220405 (2007); **101**, 110501 (2008).

[57] F. Verstraete and J.I. Cirac, arXiv:cond-mat/0407066; V. Murg, F. Verstraete, and J.I. Cirac, Phys. Rev. A **75**, 033605 (2007).

[58] P. Corboz and G. Vidal, Phys. Rev. B **80**, 165129 (2009).

[59] J. Jordan, R. Orus, G. Vidal, F. Verstraete, and J.I. Cirac, Phys. Rev. Lett. **101**, 250602 (2008).

[60] C.S. Hellberg and E. Manousakis, Phys. Rev. B **52**, 4639 (1995).

[61] C.S. Hellberg and E. Manousakis, Phys. Rev. Lett. **78**, 4609 (1997).

[62] S.R. White and D.J. Scalapino, Phys. Rev. Lett. **81**, 3227 (1998).

[63] W.O. Putikka, M.U. Luchini, and T.M. Rice, Phys. Rev. Lett. **68**, 538 (1992).

[64] C.T. Shih, Y.C. Chen, and T.K. Lee, Phys. Rev. B **57**, 627 (1998).

[65] M. Lugas, L. Spanu, F. Becca, and S. Sorella, Phys. Rev. B **74**, 165122 (2006).

[66] For a recent review, see M. Vojta, Adv. Phys. **58**, 699 (2009).

[67] S. Sorella, G.B. Martins, F. Becca, C. Gazza, L. Capriotti, A. Parola, and E. Dagotto, Phys. Rev. Lett. **88**, 117002 (2002).

[68] A. Himeda, T. Kato, and M. Ogata, Phys. Rev. Lett. **88**, 117001 (2002).

[69] M. Raczkowski, M. Capello, D. Poilblanc, R. Fresard, and A.M. Oles, Phys. Rev. B **76**, 140505(R) (2007).

[70] M. Capello, M. Raczkowski, and D. Poilblanc, Phys. Rev. B **77**, 224502 (2008).

[71] F. C. Zhang and T. M. Rice, Phys. Rev. B **37**, 3759 (1988).

[72] S. Sorella, Phys. Rev. B **71**, 241103 (2005).

[73] R. Moessner and S. Sondhi, Phys. Rev. Lett. **86**, 1881 (2001).

[74] L. Balents, M.P.A. Fisher, and S.M. Girvin, Phys. Rev. B **65**, 224412 (2002).

[75] A.Y. Kitaev, Ann. Phys. **303**, 2 (2003).

[76] A.Y. Kitaev, Ann. Phys. **321**, 2 (2005).

[77] X. Chen, Z.-C. Gu, and X.-G. Wen, Phys. Rev. B **83**, 035107 (2011); N. Schuch, D. Perez-Garca, and I. Cirac, Phys. Rev. B **84**, 165139 (2011).

[78] X. Chen, Z.-C. Gu, Z.-X. Liu, and X.-G. Wen, Phys. Rev. B **87**, 155114 (2013).

[79] A.M. Essin and M. Hermele, Phys. Rev. B **87**, 104406 (2013).

[80] A. Mesaros and Y. Ran, Phys. Rev. B **87**, 155115 (2013).

[81] L. Capriotti, F. Becca, A. Parola, and S. Sorella, Phys. Rev. Lett. **87**, 097201 (2001).

[82] S. Yan, D. Huse, and S. White, Science **332**, 1173 (2011).

[83] Y. Iqbal, F. Becca, S. Sorella, and D. Poilblanc, Phys. Rev. B **87**, 060405 (2013).

[84] S.-S. Gong, D. N. Sheng, O. I. Motrunich, and M. P. A. Fisher, arXiv:1306.6067.

[85] Z.Y. Meng, T.C. Lang, S. Wessel, F.F. Assaad, and A. Muramatsu, Nature **464**, 847 (2010).

[86] S. Sorella, Y. Otsuka, and S. Yunoki, Sci. Rep. **2**, 992 (2012).

[87] D.P. Arovas and A. Auerbach, Phys. Rev. B **38**, 316 (1988).

[88] T. Li, F. Becca, W.-J. Hu, and S. Sorella, Phys. Rev. B **86**, 075111 (2012).

[89] L. Capriotti, F. Becca, A. Parola, and S. Sorella, Phys. Rev. B **67**, 212402 (2003).

[90] F. Becca, L. Capriotti, A. Parola, and S. Sorella, Springer Ser. Solid-State Sci. **164**, 379 (2011).

[91] H.J. Schulz, T. Ziman, and D. Poilblanc, J. Phys. I **6**, 675 (1996).

[92] P. Corboz, R. Orús, B. Bauer, and G. Vidal, Phys. Rev. B **81**, 165104(2010).

[93] T. Senthil, L. Balents, S. Sachdev, A. Vishwanath, and M.P.A. Fisher, J. Phys. Soc. Jpn. **74**, 1 (2005).

[94] R. Guida and J. Zinn-Justin, J. Phys. A: Math. Gen. **31** 8103 (1998).

Acknowledgment

I would like to express my deep gratitude to my supervisors Prof. Sandro Sorella and Dr. Federico Becca for their great scientific support, kindness, patience and encouragement to me. Also I am very grateful to the stimulating collaborations with Alberto Parola and Tao Li. Special thanks to my friends for their helpful discussion on rich topics, Zhenyi Cai, Xiaochuan Ge, Ye Luo, Riccardo Sabatini, Sebastiano Saccani, Xiaoquan Yu, Hongyi, Xie, Mohammad Zhian, and Simone Ziraldo.

I am grateful to all the members of the Condensed Matter Theory group, for the inspiring work atmosphere that they create, and to the people of the Computer Staff, for their precious support. I remember with pleasure all the SISSA members, for the friendly atmosphere they provide, and my present office mates, Guglielmo Mazzola and Travis Jones.

I would like to thank my lovely flatmates Michele, Alberto and Daniel. Last but not the least I thank my parents and my sister for their continued support and my wife Yanhua Hou for these wonderful years in Italy with her.

List of Publications

- **Wen-Jun Hu** and Ning-Hua Tong,
  Dynamical Mean-Field Theory for the Bose-Hubbard Model,
  Phys. Rev. B **80**, 245110 (2009).

- **Wen-Jun Hu**, Federico Becca, and Sandro Sorella,
  Absence of static stripes in the two-dimensional $t-J$ model by an accurate and systematic quantum Monte Carlo approach,
  Phys. Rev. B **85**, 081110(R) (2012).

- Tao Li, Federico Becca, **Wen-Jun Hu**, and Sandro Sorella,
  Gapped spin-liquid phase in the J_1-J_2 Heisenberg model by a bosonic resonating valence-bond ansatz,
  Phys. Rev. B **86**, 075111 (2012).

- **Wen-Jun Hu**, Federico Becca, Alberto Parola, and Sandro Sorella,
  Direct evidence for a gapless Z_2 spin liquid by frustrating Néel Antiferromagnetism,
  Phys. Rev. B **88**, 060402(R) (2013).